Active Flat Optics Wavefront Manipulation for Imaging, Ranging, and Sensing

Thesis by
Seyed Mohammadreza Fatemi

In Partial Fulfillment of the Requirements for the
Degree of
Doctor of Philosophy

Caltech

CALIFORNIA INSTITUTE OF TECHNOLOGY
Pasadena, California

2020
Defended August 18, 2020

To the love of my life,
my wife Nassrin.

ACKNOWLEDGEMENTS

My first gratitude always goes to my parents who devoted their time, energy, and lives and provided me with an infinite source of guidance and love throughout my life. Every achievement I had in life was a seed they planted and nurtured. The support of my parents, my sister, and my brother gave me the courage for every step for which I am always thankful to them. I also owe a debt of gratitude to my wife, Nassrin, who stood next to me for every moment of my Ph.D. studies and was a persisting support to me. I hope that I can reciprocate at least a small fraction of the happiness and joy she brings to me.

The most precious gift in my life, that I could never appreciate enough, was being surrounded by smart people. Caltech is, of course, a unique place to pursue higher education and work towards Ph.D., but what makes it special is the people including all the faculties, students, and staff. During my years at Caltech, I had the privilege of being a member of the CHIC lab, and work with an insightful advisor, Professor Ali Hajimiri. He is not only creative, innovative, masters several subject matters, and academically brilliant, but more importantly a close friend to his students who cares about them on a personal level. I am deeply appreciative of him for everything I learned over the course of my Ph.D. as well as the friendly and warm atmosphere he created within the group.

I would like to thank all the members of the CHIC lab, in particular Aroutin Khachaturian, who is a dear friend, a great partner in technical discussions and developments, and a resourceful scientist in practice. Also, Parham Khial, who aside from being a collaborator on some adventurous project ideas was a close friend and the company of conversations about deep and fundamental research subjects. Every member of the CHIC lab that I had the chance to be labmate with, Amirreza Safaripour, Alex Pai, Behrooz Abiri, Constantine Sideris, Aroutin Khachaturian, Brian Hong, Matan Gal-Katziri, Parham Khial, Austin Fikes, Elliott Williams, Craig Ives, Samir Nooshabadi, Oren Mizrahi, Armina Khakpour, and Ailec Wu, is a bright and unique person who contributed to my research and personal developments. I would like to express my appreciation to Professors Changhuei Yang, Kerry Vahala, Azita Emami, and Andrei Faraon for serving on my thesis committee and providing me with great feedback. There are many others to whom I owe thanks and gratitude. While I do not have enough space to mention everyone, I will always remember them and wish them the best wherever they are.

ABSTRACT

The emergence and maturity of integrated photonic platforms over the past decade allowed for reliable integration of a large number of photonic components on a single substrate. This ability to process and control coherent light on a chip is a potential pathway for the realization of novel low-cost systems capable of non-conventional functionalities for optical wavefront engineering. In this thesis, integrated active flat optics architectures for generation, manipulation, and reception of optical wavefronts are investigated. In particular, the application of such systems for imaging, ranging, and sensing are studied and multiple photonic systems including a large scale transmitter, a high-sensitivity receiver, and a high-resolution transceiver are demonstrated.

For generation of optical wavefronts, solutions for engineering a radiative optical waveform via emission by an array of nano-photonic antennas are studied and a chip-scale photonic transmitter is implemented. The transmitter forms an optical phased array with a novel architecture in a CMOS compatible silicon photonics process which not only dispenses with the limitations of previously demonstrated systems but also yields a narrower beamwidth leading to a higher resolution. Moreover, an integrated adaptive flat optical receiver architecture that collects samples of the incident light and processes it on-chip with high detection sensitivity is implemented. To detect the optical samples with a high signal to noise ratio, an optoelectronic mixer is proposed and designed that down-converts the optical signals received by each antenna to a radio frequency signal in the electronic domain, provides conversion gain, and rejects interferers. This system allows arbitrary wavefront manipulation of the received signal by adapting itself to new conditions — a capability that does not exist in conventional cameras. Using this system, we realized the first high-sensitivity optical phased array receivers with one-dimensional and two-dimensional apertures and the functionality of the chips as ultra-thin lens-less cameras were demonstrated. To achieve a high-resolution integrated photonic 3D imager with low system complexity, a double spectral sampling method is developed through a special wavefront sampling arrangement on the transmitter and receiver apertures. This transceiver architecture includes a multi-beam transmitter and a high-sensitivity receiver that can distinguish the illuminated points separately and process them simultaneously using a digital signal processor.

Moreover, novel ultra-low power architectures for generation and reception of short

RF/microwave pulses are explored. Such systems have a broad range of applications including imaging and ranging. In this study, the capability of generating and receiving orthogonal Hermite pulses of various orders using a capacitor-only time-varying network is demonstrated.

PUBLISHED CONTENT AND CONTRIBUTIONS

R. Fatemi, A. Khachaturian, and A. Hajimiri, "A nonuniform sparse 2-D large-FOV optical phased array with a low-power PWM drive,"IEEE Journal of Solid-State Circuits, vol. 54, no. 5, pp. 1200–1215, 2019. Available: `https://ieeexplore.ieee.org/document/8649827`.
https://doi.org/10.1109/JSSC.2019.2896767.
I designed, measured, and wrote the paper.

R. Fatemi, P.Khial, A. Khachaturian, and A. Hajimiri, "Breaking FOV-aperture trade-off with multi-mode nano-photonic antennas," IEEE Journal of Selected Topics in Quantum Electronics, 2021. [Accepted]
I performed the theoretical developments, simulated, and wrote the paper.

R. Fatemi, B. Abiri, A. Khachaturian, and A. Hajimiri, "High sensitivity active flat optics optical phased array receiver with a two-dimensional aperture," Opt. Express, vol. 26, no. 23, pp. 29 983–29 999, Nov. 2018. Available: `http://www.opticsexpress.org/abstract.cfm?URI=oe-26-23-29983`.
https://doi.org/10.1364/OE.26.029983.
I modified the design, measured, and wrote the paper.

R. Fatemi, A. Khachaturian, and A. Hajimiri, "A low power PWM optical phased array transmitter with 16° field-of-view and 0.8° beamwidth," in 2018 IEEE Radio Frequency Integrated Circuits Symposium (RFIC), 2018, pp. 28–31. Available: `https://ieeexplore.ieee.org/abstract/document/8428847`.
https://doi.org/10.1109/RFIC.2018.8428847.
I designed, measured, and wrote the paper.

R. Fatemi, A. Khachaturian, and A. Hajimiri, "Scalable optical phased array with sparse 2D aperture," in Conference on Lasers and Electro-Optics,Optical Society of America, 2018, STu4B.6. Available: `http://www.osapublishing.org/abstract.cfm?URI=CLEO_SI-2018-STu4B.6`.
https://doi.org/10.1364/CLEO_SI.2018.STu4B.6.
I designed, measured, and wrote the paper.

R. Fatemi, B. Abiri, and A. Hajimiri, "An 8×8 heterodyne lens-less OPA camera," in Conference on Lasers and Electro-Optics, Optical Society of America, 2017, JW2A.9. Available: `http://www.osapublishing.org/abstract.cfm?URI=CLEO_QELS-2017-JW2A.9`.

https://doi.org/10.1364/CLEO_AT.2017.JW2A.9.
I modified the design, measured, and wrote the paper.

R. Fatemi, B. Abiri, and A. Hajimiri, "A one-dimensional heterodyne lens-free OPA camera," in Conferenceon Lasers and Electro-Optics, Optical Society of America, 2016, STu3G.3. Available: `http://www.osapublishing.org/abstract.cfm?URI=CLEO_SI-2016-STu3G.3`.
https://doi.org/10.1364/CLEO_SI.2016.STu3G.3.
I modified the design, measured, and wrote the paper.

B. Abiri, R. Fatemi, and A. Hajimiri, "A 1-D heterodyne lens-free optical phased array camera with reference phase shifting,"IEEE Photonics Journal, vol. 10, no. 5, pp. 1–12, 2018. Available: `https://ieeexplore.ieee.org/document/8471238`.
https://doi.org/10.1109/JPHOT.2018.287182.
I modified the design, measured, and wrote the paper.

TABLE OF CONTENTS

LIST OF ILLUSTRATIONS

LIST OF TABLES

Chapter 1

INTRODUCTION

> “The duty of the man who investigates the writings of scientists, if learning the truth is his goal, is to make himself an enemy of all that he reads, and ... attack it from every side. He should also suspect himself as he performs his critical examination of it, so that he may avoid falling into either prejudice or leniency.”
>
> Ibn al-Haytham (Alhazen), 1021 AD

The history of pondering about light and its mysteries is entangled with the story of human kind from ancient mythologies to the earliest known philosophical studies. Euclid and Ptolemy used geometry to explain the properties of light and believed that sight works by the eye emitting rays of light. Centuries later, Ibn Al-Haytham conducted many experiments with lenses, mirrors, refraction, and reflection, explained human vision system, and showed through experiment (rather than pure philosophy) that light is an external phenomenon traveling in straight lines [1]. He also invented and quantified camera obscura, which is in fact a simple construct for manipulating a reflected light to form an image. Later, advances in engineering light with lenses and mirrors became the gateway to understand the laws of mechanics by observing celestial bodies through the works of Galileo and many others [2] while the nature of light itself remained unknown. In 1690, Christian Huygens proposed a wave nature for light based on an intuitive conviction [3], but the corpuscular theory of light supported by Isaac Newton, a scientist with immense reputation, was favored throughout the 18th century [4]. It was not until 1804 that Thomas Young's interferometric experiment shed light on the wave nature of light and helped researchers such as Augustin Fresnel to devise various other optical devises [5].

The major milestone in quantitatively describing light was taken by James Clerk Maxwell showing that light is an electromagnetic wave [6] which was followed by further research by Poincare, Kirchhoff, Sommerfeld, and many others leading to the development of Fourier optics [7]. Consequently, wavefront shaping and engineering using various types of lenses, mirrors, and novel optical system significantly impacted many fields of science and engineering. Within a short time after Heinrich Hertz provided experimental evidence for Maxwell's equations in 1884 [8], generation, manipulation, wavefront engineering, and reception of electromagnetic waves up to the microwave region was extensively explored and a wide range of antennas and transmitter/receiver architectures have been realized [9]. However, the absence of a coherent optical source as well as fabrication platforms at nano-scale delayed the realization of similar systems in optical region of the spectrum and optical wavefront manipulation was primarily performed via lenses.

The discoveries about the particle nature of light and theoretical developments on quantum intraction of photons and atoms in the 20th century eventually led to the invention of laser in the 1960s [10], providing a coherent source of light. The invariance of the coherent light to a shift by a wavelength allows for controlling the wavefront by tuning over only a single cycle through phase wrapping. Therefore, various kinds of spatial light modulators (SLM) such as liquid crystal SLMs [11] and MEMs based devices [12] have been developed with capabilities of modulating/controlling both amplitude and phase of the optical wavefront with electrically controlled micron-sized pixels. SLMs revolutionized the display technology, introduced new microscopy methods, provided laser beam shaping, aberration control, and much more. Moreover, the electro-optically controlled pixels of the SLMs allowed for rapid switching between configurations leading to many novel practical optical systems such as controlled lenses, active free-space optical communications [13], and adaptive optics [14].

While designing photonic antennas similar to microwave antennas were not conventionally feasible due to the small optical wavelengths, advances in nano-technology, enabled by employing the light itself for photo-lithography processes, paved the way for the fabrication of miniaturized structures on various material platforms. However, its impact on the electronic industry and integrated systems drew most of the attentions and investments to pursuing low cost fabrication platforms for the continuously scaling transistors. While integrated electronics has revolutionized how we communicate, process data, and access information by controlling the motion of electrons, photons also played an important role in the advent of the information age by enabling the global telecommunications networks. Shortly after the invention of lasers, low loss optical fibers with 20 dB/km at 632.8 nm wavelength were demonstrated in 1970 [15] and evolved to achieve optical loss of 0.2 dB/km at 1.55 μm in the same decade [16], which is about the same value for the standard optical fibers today [17]. The unique features of optical fibers such as large bandwidth, negligible latency, low loss, and low cross-talk allowed for the extraordinary growth in the world-wide data communication, with a record transmission capacity of over a hundred petabits per second in a single fiber of 125 μm diameter [18].

The focus on the communication industry and development of integrated silicon-based platforms led to the emergence of a new paradigm of integrated photonics on silicon-on-insulator (SOI) platforms over the past decade [19]. Designers can now integrate a large number of photonic components on a single silicon chip, and photonic foundries have become more commonplace and offer multi-project wafer (MPW) runs, which enable circuit and system researchers to explore novel photonic integrated solutions. This provides new opportunities to devise non-conventional optical wavefront manipulation techniques and a new generation of optical devices. Efficient and low-cost on-chip waveform engineering reduces the size of many conventional optical systems by integrating many of these processes on a single chip, which in turn results in reduced cost, scalability, and higher yield. Moreover, it opens up the door for many novel applications and enables functionalities that have not been previously feasible or possible. In the future, this success of realizing reliable and low cost silicon-based integrated photonic platforms will be followed by the inclusion of other photonic materials and integration of high speed transistors along side the photonic components leading to further developments and expansion in this field.

In this thesis, active flat photonic systems implemented on integrated platforms for generation, manipulation, and reception of optical wavefronts are studied. In particular, application of such systems for imaging, ranging, and sensing are considered and various photonic systems including a large scale transmitter, a high-sensitivity receiver, and a high-resolution transceiver are realized.

1.1 Contributions

In this thesis, we investigated architectures and systems to realize integrated active flat optics wavefront manipulation for imaging, ranging, sensing, and communication. We studied solutions for engineering a radiative optical wavefront via nano-photonic transmitters, as well as processing incoming light on a photonic chip for directive collection and high-sensitivity detection. As a result of this research, we demonstrated a large-scale optical phased array (OPA) with a novel architecture in a CMOS compatible silicon photonic process [20]–[22]. The proposed array not only dispenses with the limitations of previously demonstrated OPAs, but also yields a narrower beamwidth leading to a higher resolution. The proof-of-concept implementation for this architecture achieves 30 times higher resolution than the state-of-the-art 2-D OPAs. The primary benefit of such OPAs is to form an electronically steerable optical beam. Forming and steering an optical beam can have a wide range of applications, such as target detection and tracking, LiDAR, optical wireless communication, image projection, and surface meteorology.

Moreover, we studied novel solutions to realize photonic receivers, demonstrating an integrated adaptive flat optical receiver architecture that collects samples of incident light and processes it on-chip with high detection sensitivity [23]–[26]. The ability to electronically control all the optical properties of an optical receiver using a compact low-cost silicon photonic chip, without any mechanical movement, lenses, or mirrors, paves the way for future generations of imagers and sensors, as well as receivers for data communication. In this system, nano-photonic antennas with large effective apertures are designed to collect samples of the incident light. It is shown analytically that under certain conditions, the incident waveform can be reconstructed using a set of captured samples and its information can be extracted. To detect the optical samples with a high signal-to-noise ratio, an optoelectronic mixer is proposed and designed that down-converts the optical signals received by each antenna to a radio frequency signal in the electronic domain, provides conversion gain, and rejects interferers. This system allows arbitrary wave-front manipulation of the received signal by adapting itself to new conditions — a capability that does not exist in conventional cameras. Using this system, we designed the first high-sensitivity optical phased array receivers with one-dimensional [24], [26] and two-dimensional [23], [25] apertures. The functionality of the chips as ultra-thin lens-less cameras was demonstrated by imaging objects through electronically steering of the main lobe (the angle with maximum directivity).

To realize a nano-photonic system for high-resolution 3D imaging applications, a transceiver architecture is devised based on a double spectral sampling technique. This system includes a multi-beam transmitter and a photonic receiver with digital wave processing. The proposed double spectral sampling method for photonic aperture design enables the operation of the system with an under-sampled transmitter and receiver apertures such that information can be extracted unambiguously. The transceiver system enables high imaging resolution while maintaining a low system complexity, power consumption, and optical loss. Moreover, this architecture provides a robustness against interference, stray reflections, and clutter.

A major drawback of photonic receivers is the small collection area due to the relatively small number of elements as well as small fill-factor of the receiving aperture. To devise nano-photonic antennas with high effective aperture and high FOV, we investigated the fundamental trade-offs in nano-antenna design to increase the effective aperture while maintaining a large field-of-view. Multi-mode nano-photonic antennas are presented as a solution for breaking the fundamental conventional limits and accordingly various antenna structures are demonstrated.

In addition to the photonic systems, we explored new opportunities in RF and microwave integrated circuit design for pulse generation and detection. We developed a family of time-varying systems that can generate arbitrary modulated/baseband pulses during the circuit transitions and detect the same waveforms through a correlation function, which is embedded in the functionality of the system. We demonstrated the capability of generating and receiving Hermite pulses of various orders using a capacitor-only time-varying network. Such a system can be used for high data-rate communications and ultra-low power applications, as well as pulsed imaging and sensing.

1.2 Thesis outline

The rest of this thesis is organized as follows: Chapter 2 introduces integrated silicon photonic platforms with a brief description of various photonic components and potential optical structures that can be fabricated on a photonic chip. Moreover, it provides an analytical setup for studying radiation from an aperture which is used in the later chapters, and presents a review of the state-of-the-art optical wavefront manipulation methods with a focus on optical phased arrays.

Chapter 3 starts with the motivations for scaling optical phase arrays as a photonic wave-front engineering technology and presents an analytical development illustrating the trade-offs, which is followed by design and implementation of a large scale sparse OPA transmitter. In Chapter 4, the general setting of an integrated photonic receiver is explained and by utilizing the high sensitivity detection property of heterodyne detection an opto-electronic mixer is designed. The developed platform is used to realize the first functional integrated photonic receiver with phase array processing, capable of forming a reception beam and steering it electronically. Furthermore, the functionality of this system as a lens-less camera is demonstrated.

Using these developments, Chapter 5 introduces a transceiver architecture capable of high-resolution 3D imaging. In this chapter, first the challenges in realizing a 3D imager using integrated photonics are discussed. Then, the proposed double spectral sampling method is explained and used to extend the photonic system to a transceiver architecture, which includes a multi-beam transmitter and a photonic receiver with digital waveform processing. This chapter is followed by the design details of the implemented system. A major problem for photonic receivers is the small collection area due to the relatively small number of elements as well as small fill-factor. This is the subject of Chapter 6, which is dedicated to studying the fundamental trade-offs in increasing the effective aperture of nano-photonic antennas while maintaining a large field-of-view. Multi-mode antennas are presented as a solution for breaking the fundamental limits and accordingly various antenna structures are proposed and demonstrated.

In Chapter 7, an electronic system for generating and receiving short RF/microwave pulses is demonstrated that can be used for ranging and imaging as well as data communication. This system is based on a time-varying network that generates Hermite pulses and receives them with high-sensitivity as an analog correlator.

Chapter 2

INTEGRATED PHOTONIC SYSTEMS

In this chapter, a brief survey of the existing wavefront engineering techniques including the recently developed integrated photonic systems is conducted. Moreover, the standard low cost integrated silicon photonic platforms are described with a brief discussion of various photonic structures and components that can be realized on such photonic chips. Finally, an analytical framework for studying radiation from an aperture is discussed, which will be used in later chapters, and a review of the state-of-the-art optical phased arrays as integrated photonic systems capable of forming an optical beam through controlling the radiation from an aperture is presented.

2.1 Wavefront generation and manipulation

Precise generation, manipulation, and control of the optical wavefront is required in many applications. Due to the small wavelength of optical signals, conventionally, lenses of various types, which are refractive optical elements, were the primary components used to perform wavefront adjustment and transformation. The advent of the spatial light modulators (SLM) such as various kinds of liquid crystal SLMs [11] and MEMs based devices (e.g. digital micro-mirror device (DMD) [12], grating light valve (GLV) [27], etc.) provided a great deal of flexibility in modulating/controlling the amplitude, phase, and polarization of the optical wavefront in both space and time on micrometer scale pixel sizes. SLM devices, which are diffractive optical elements, have been used to improve conventional optical systems as well as to devise novel optical functionalities such as high-resolution video image projection, speckle field manipulation, focusing in a complex media, tailoring the light, study of atmospheric turbulence, adaptive channel equalization in free-space communication, holographic projection, polarization control, optical trapping, and many others. These functionalities enabled various novel optical systems for applications such as optical metrology [28], scanning and printing technologies, laser pulse shaping [29], projectors and holographic projection systems [30], optical information processing, optical tweezers [31], [32], automotive applications, generation of vector beams [33], microscopy [11], holographic data storage, free-space optical communication, orbital angular momentum communications [34], etc. Moreover, the ability to reconfigure SLM settings led to the emergence of *adaptive optics*, which is an active field of study aiming for dynamically correcting wavefront aberrations in order to improve the performance of optical system. However, bulky footprint, high cost, low fabrication yield, relatively large pixel size (usually in the order of several wavelengths), low reconfiguration speed, not being able to control all the parameters of light and controlling them independently, and the need for an external light source are some of the drawbacks and limitations of the current SLM technologies.

Advances in nano-fabrication over the past few decades provided the possibility of implementing micro-meter scale structures, comparable to optical wavelengths, on a thin substrate. Subsequently, there has been a rise in research on this field of flat optics to investigate photonic devices that can modify different constitutive properties of light such as wavelength, amplitude, phase, and polarization state using a large number of photonic subwavelength structures called photonic antennas [35]–[41]. These nonidentical antennas, collectively forming a metasurface structure, capture the incident light and radiate the scattered light back into the free-space and enable the nano-scale control of the wavefront by adjusting its local amplitude, phase, and polarization. These devices were designed and demonstrated for a wide range of applications such as lenses [37], lasers [38], spectroscopy and nano-imaging [39], light emitters in LEDs [40], polarization control devices [41], etc. in both transmittive and reflective modes. Recently, active metasurface devices have also been demonstrated in which the properties of each nano-antenna are electronically adjustable [42]. The antennas on metasurface structures are the primary (and most of the times only) components that process the incident wavefront and operate independent from each other. This solo performance of the antennas which is limited to their local region significantly limits the design space and potential functionalities that can be realized.

Over the past decade, the maturity of photonic integration technologies, which were initially focused on developing higher speed optical communication links, gave birth to a new paradigm of integrated photonics. An integrated photonic platform enables fabrication of a large number of photonic components on a single chip. Thus, coherent light can be processed on-chip through filtering, modulation, phase shift, amplitude adjustment, mode conversion, etc. to realize various functionalities that can bring about novel integrated photonic solutions. With the advent of these integrated active flat optic systems, a second type of nano-photonic antennas has emerged [43]–[46]. In this context, an antenna is defined as a transducer that couples a guided mode into free-space mode and vice versa [20], which is the same definition used for conventional microwave antennas. In other words, an antenna is an on-chip component that in the transmitter setting is fed with a guided mode and radiates into the free-space, and in the receiver setting, captures the free-space incident wave and couples it into an on-chip waveguide. Therefore, a receiving aperture consisting an array of these antennas can be used to capture a wavefront, which is then processed and manipulated on-chip. The adjusted signals are then radiated back into the free space through a transmitter aperture with transmitter antennas [47]. This provides a greater flexibility due to the more complicated processing and avoiding the limitation of isolated and solo-performing antennas in metasurface devices. Moreover, addition of a laser source (either integrated or fed to the chip) enables the system to generate a desired wavefront with defined spatial and temporal properties. It is also possible to fully capture an incident wavefront and output its extracted features after complex detection processes on-chip.

While realization of complex systems such as 3D holographic projectors and lensless cameras on a commercial standard level are among the potential capabilities of integrated photonic platforms, optical beamforming and steering, which needs a relatively smaller aperture, have already attracted a great deal of interest in this field. Efficient and low cost on-chip waveform and wavefront engineering reduces the size of many conventional optical systems by integrating many of these processes on a chip which in turn results in a reduced cost, scalability, and higher yield. Since phased array processing is suitable for beamforming, active optical phased arrays with small apertures were demonstrated recently that can be used in systems such as LiDAR [48], autonomous vehicles, and point-to-point communication [49], [50]. Large-scale OPA transmitters with more than a thousand radiating elements are required to form a narrow beamwidth and high-resolution. Consequently, there have been several attempts to increase the number of elements in the array and implement functional OPA transmitters on silicon photonic platforms [43], [44], [46], [51], [52]. Since a phased array, in its general form, includes phase and amplitude control for all the radiating elements, realization of a large scale OPA opens the door for arbitrary wavefront control for more complex systems.

2.2 Integrated silicon photonic platform

Over the past decade, reliable and low cost integration of a large number (thousands) of optical components on a single silicon-based chip has become possible using various flavors of silicon-on-insulator (SOI) processes. These fabrication platforms

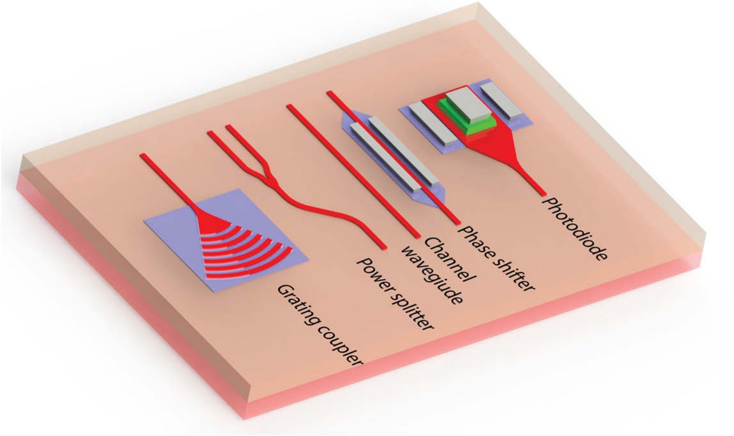

Figure 2.1: (a) Simplified schematic of a typical silicon photonics platform consisting a bulk silicon substrate and a buried oxide layer (BOX). Optical components are fabricated using the silicon layer on the BOX.

are compatible with commercial CMOS technologies, become more commonplace, and offer multi-project wafer (MPW) runs, which enable a broad range of new architectures and applications [53], [54]. The unique feature of this technology that distinguishes it from other nano-photonic systems is the possibility of designing complex systems in which many photonic components operate in harmony to process the optical signal.

Silicon photonic platforms are often based on an SOI process (Fig. 2.1) and in its simplest form have a single top silicon layer which is etched and doped to realize passive and active elements. Passive components such as dielectric waveguides, power splitters/combiners, and grating couplers transform and process the optical modes and active components such as phase shifters and optical modulators interface the optics with electronics. For a silicon-based photonic layer, these components operate at wavelengths above λ =1.1 µm to maintain a low loss and avoid photon absorption due to the silicon band gap. The transfer of signals from optics to electronics is realized by embedding photodetectors, which is often realized by adding a germanium layer which has a lower band gap compared to silicon. Germanium is usually added through epitaxial growth and enables efficient photon absorption for wavelengths up to λ = 1.8 µm. For longer wavelengths germanium become transparent and can be used to form optical waveguide. Most of today's low cost silicon photonic processes provide a single photonic layer, made of silicon, with multiple etch depths and doping levels used for grating coupler design and electrical access to the waveguides. This planar photonic structure presents optical routing challenges for implementation of certain complex systems as the number of components scales. On the other hand, multi-layer photonic platform offers multiple photonic layers that can interact with each other to realize more complex devices [55].The extra photonic layers are made of silicon-nitride [56] in some platforms which offer lower loss and a broader operational bandwidth including the visible range. However, in general, the target operating wavelength dictates the appropriate material for photonic layers.

The photonic layers are usually covered with silicon oxide and one or more metal layers are added above the photonic layers for routing and electrical interface to the devices. These metal layers contact with each other and photonic layers through inter-layer metal vias. The metal layers are usually more than 1 µm away from the photonic layers to avoid optical loss. Moreover, their low resistive loss provides the possibility of realizing traveling wave structures and microwave transmission lines along with the photonic devices. In the following, a brief description of various components that can be fabricated on such integrated photonic platforms is presented.

Photonic waveguide

An integrated photonic waveguide is one of the fundamental building blocks on integrated photonic platforms mainly used for routing and guiding the optical waves on the chip. While metallic waveguides are widely used in microwave frequencies, the high optical loss of the metals makes dielectric waveguides the suitable choice for almost all the applications. In a dielectric waveguide, the propagating optical power is confined inside the waveguide due to its higher refractive index compared to the surrounding material. While various forms of waveguides such as ridge, rib, buried, diffused, strip-loaded, and slot waveguides have been proposed for integrated photonics, rib and ridge waveguides are the most commonly used in standard silicon photonic platforms. Figure 2.2 shows a ridge (channel) waveguide which is formed by etching the photonic layer and later depositing silicon oxide that surrounds the waveguide core. Depending on its size, a waveguide can support one or multiple propagating modes. Due to the fabrication non-idealities and surface roughness of the practical implementations, there will be a random and uncontrolled mode coupling in multimode waveguides which can interrupt the operation of the photonic components. Therefore, it is desirable to adjust the dimensions of the waveguide for the target wavelength to support a single mode with low loss while prohibiting the propagation of higher order modes. However, for dielectric waveguides, there will always be a TE and a TM propagating mode. For 1.550 nm wavelength, 220 nm

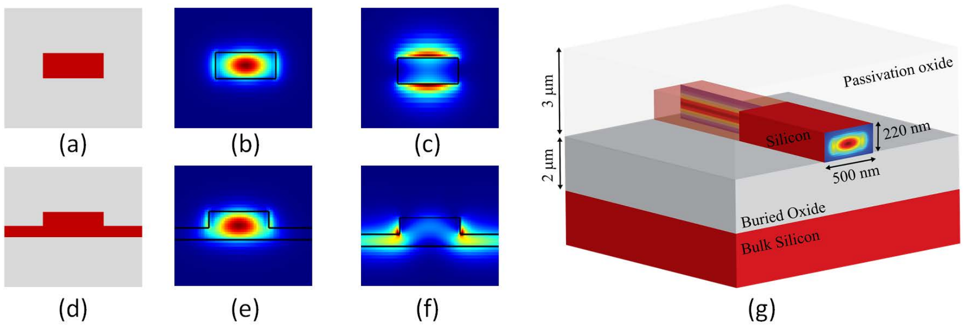

Figure 2.2: Single mode dielectric waveguides for $\lambda = 1, 55nm$ wavelength (a) Channel waveguide (b) TE mode of the channel waveguide (c) TM mode of the channel waveguide (d) Rib waveguide (e) TE mode of the rib waveguide (f) TM mode of the rib waveguide (g) A channel waveguide on a SOI silicon photonic platform.

height and 500 nm width yields a waveguide that only supports a single TE and a single TM mode. The energy of the TE mode is confined inside the structure while the TM mode will suffer high optical loss due to the surface roughness of the implemented waveguide, thus leasing to an effectively single mode waveguide. It is also possible to form rib waveguides in standard silicon photonic platforms using the etching levels provided for the photonic layer. While ridge waveguides have better confinement and lower optical loss, to control the propagation of light inside the waveguide, design modulators, and mode converters rib waveguides are more suitable.

Couplers and splitters

Couplers and splitters are passive optical components that can be used to convert optical modes and split/combine optical power from a set of inputs to a set of outputs. The most commonly used coupling mechanism on integrated platforms is evanescent coupling, which provides a low loss and efficient transfer of power from one waveguide to another. This coupling mechanism can be used to form a directional coupler which is a 4-port network as shown in Fig. 2.3(a) in which the length of the coupling region and gap spacing define the coupling ratio. Moreover, if the coupler structure is symmetric with respect to both axes, it is a hybrid directional coupler and features a 90° phase difference between its coupled and through ports. This can be used to form a differential beat component at these two ports and form a balance photodetector (this is described in more details in section 4.4).

While a coupler can be used to split or combine optical signals with arbitrary ratios

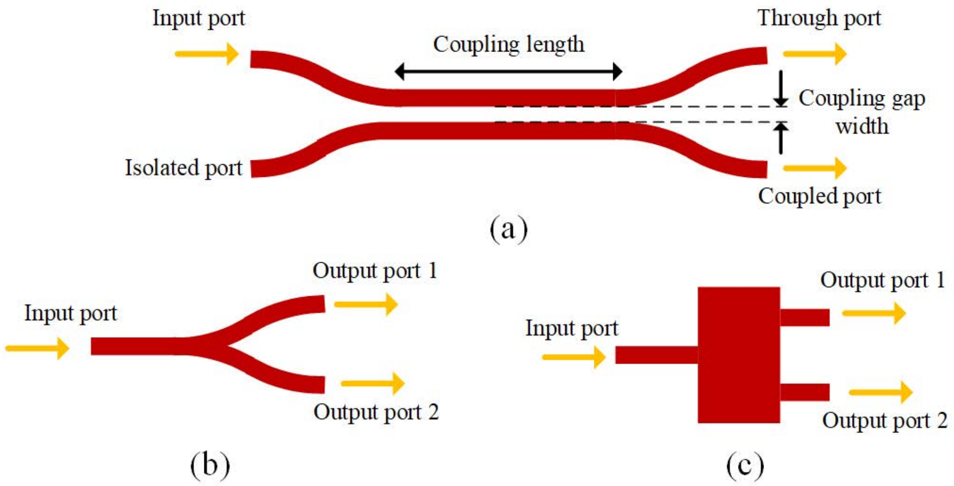

Figure 2.3: Diagram of a (a) Directional coupler (b) Y-Splitter (c) MMI splitter

and low loss, 3-port Y-splitter and MMI (Multimode interference) couplers/splitters are other passive devices with smaller footprint which are more robust to fabrication errors and mismatches. A Y-splitter is a symmetric structure that splits the input optical power into two equal fractions by converting the input mode to the two output modes. If the optical waves are fed in the reverse direction with the same phases, perfect power combining can also be achieved. Since there is no ideal power combiner for electromagnetic waves [57], the photonic Y-splitter suffers from reflections at the input in the combining mode if there is a phase or amplitude mismatched between the two inputs.

MMI splitter/couplers are a variety of compact couplers with one or multiple input/output ports which are used to split or couple the power at the input ports to the output ports. These components include a multimode slab at their central part which is the section in which coupling and splitting happen by converting the single mode inputs into multimode waves and coupling back to the single mode output waveguides.

Grating couplers and nano-photonic antenna

Grating couplers are passive components with a periodic grating that modulate the spatial frequencies of the guided mode and couple it into a different direction. These couplers are usually used to couple light from an optical fiber into the on-chip waveguides and vice versa. Figure 2.4(a) shows a focusing grating coupler which has a relatively large footprint of 50 µm by 50 µm.

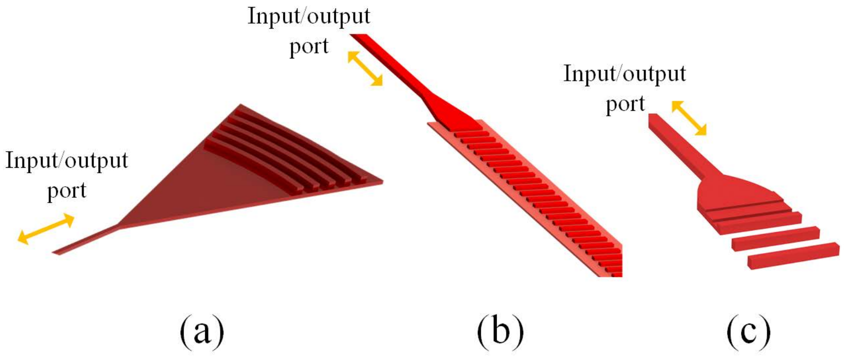

Figure 2.4: Diagram of a (a) focusing grating coupler for interfacing a fiber and the chip (b) nano-photonic antenna with a 1D FOV (narrow in one direction and suitable for 1D OPAs)(c) nano-photonic antenna with a 2D FOV

In early implementations of some nano-photonic systems, focusing grating couplers have been used to couple light into free-space as well. However, more efficient nano-photonic antenna structures have been designed to radiate light in the transmitter mode and collect light in the receiver mode with defined field-of-view, directivity, and effective aperture. Nano-photonic antennas can be designed for 1D and 2D FOV, Fig. 2.4(b)-(c). More details on nano-photonic antennas and novel structures are discussed in section 6.

Phase shifter

Phase shifting is an important function for systems operating with coherent light and can be used to construct more complex functionalities such as filtering, amplitude modulation, active mode conversion, etc. There are various mechanisms available on integrated platforms to realize an adjustable phase shifter which are mainly based on changing the effective optical path length in response to an electrical control signal. Therefore, the phase shift induced in response to an effective index change of Δn is

$$\Delta\phi = \frac{2\pi\Delta nL}{\lambda} \tag{2.1}$$

in which L is the physical length of the phase shifter and λ is the free-space wavelength of light. Since Δn is usually very small, in the order of 10^-4, hundreds of micron length is required for the phase shifter to achieve a 2π phase shift.

There are three types of phase shift/modulation mechanisms commonly used on silicon photonic platforms which are thermal based, free carrier dispersion based, and non-linearity based. A thermal phase shifter relies on the variation of the silicon refractive index versus temperature which has a temperature coefficient of

$\beta = dn/dT = 1.86\times10^{-4}K^{-1}$ [58] at a wavelength of 1.550 nm. Therefore, changing the temperature of a silicon waveguide with a length L by ΔT results in a phase shift of $2\pi\beta L\Delta T/\lambda$. By providing enough temperature change a 2π phase shift can be achieved. On integrated systems, the local temperature of the waveguides is controlled by adjusting the drive voltage and power dissipation in an electrical resistor in the vicinity of the waveguide as shown in Fig. 2.5(a). The bandwidth of a thermal phase shifter is limited to the its thermal response, which is a function of its thermal resistance and capacitance to a colder source. While thermal phase shifters have a slower speed compared to other types of phase shifters, their optical insertion loss is negligible and makes them suitable for power sensitive applications with slow variations.

On the other hand, carrier dispersion based phase shifters can reach a high bandwidth of tens of gigahertz. This type of phase shifters induce a phase shift to a light passing in a waveguide by changing the charge (electron and holes) density in the waveguide. The two commonly used architectures are shown in Fig. 2.5(b) and (c) which are PiN and PN diodes respectively. The PiN diode functions in forward bias and the current passing through the diode interacts with the optical mode. Changing the current changes the charge density and accordingly the phase shift per unit length. The PN structure works in reverse bias. The reverse bias voltage level determines the width of the depletion region and accordingly the phase shift per unit length.

The third type of phase shifting mechanism is based on the optical non-linearity of the waveguide material itself. Any material reveals nonlinear behavior if it is exposed to a large field magnitude. Applying a large enough electric field across the waveguide changes its refractive index due to the contribution of the higher order polarization factors. While silicon has a symmetric crystal lattice (thus no second order non-linearity) and have a relatively small third order non-linearity, phase shifters [59] have been demonstrated to work based on these nonlinear effects on silicon photonics platforms. The nonlinear effects are very fast and such phase shifters offer bandwidth beyond the modulating speed of electronic circuits. Moreover, the circuit model of these phase shifters is capacitive and there is no resistive power consumption.

Amplitude modulator

The amplitude modulators on integrated platforms can be categorized into two different classes of absorption based and interference based according to their operation principle. The absorption based amplitude modulators attenuate the optical signal in

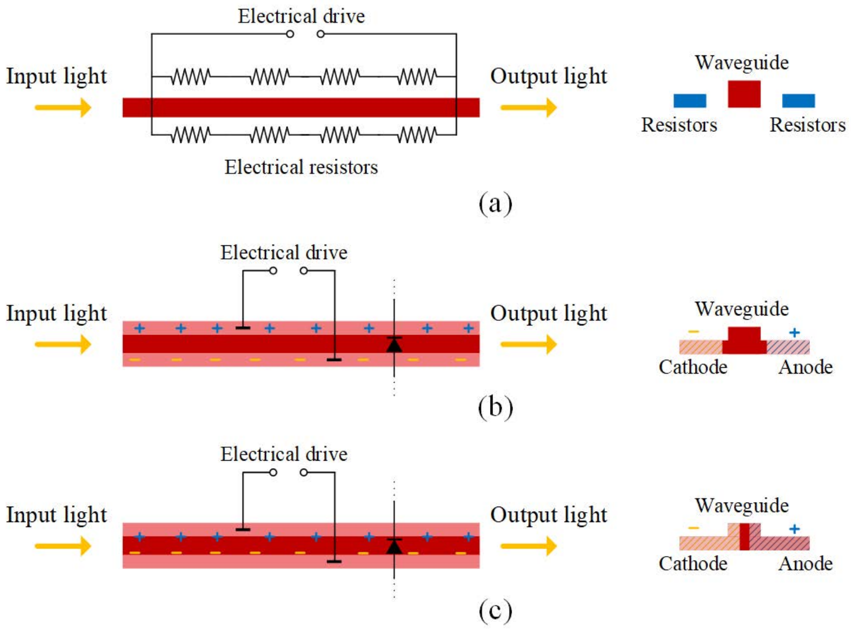

Figure 2.5: (a) Thermal phase shifter with electrical resistors controlling the temperature through their power consumption. (b) PiN diode phase shifter operating in forward bias and controlling the phase shift by adjusting the current passing through the diode. (c) PN diode phase shifter operating in reverse bias and controlling the phase shift by changing the depletion region width of the diode.

response to an electrical signal. Therefore, these modulators are lossy structures and suitable for applications that power efficiency is not a design concern. Moreover, in complex photonic systems that requires multiple modulators in series, the high loss of the overall architecture usually rules out the possibility of using this kind of modulators. However, absorption-based amplitude modulators usually do not need a (precise) calibration and feature high switching speed and simplicity, which makes them a suitable choice for many applications.

Since charge carriers in the light path will cause attenuation of the wave as well, the same phase modulators structures for phase shifting can be redesigned for amplitude modulation. Increasing the charge density in the waveguide increases the absorption coefficient and consequently reduces the amplitude of the output light. The modulator should be long enough to provide the desired extinction ratio. However, the longer length translates to a larger insertion loss as well. In addition to the plasma dispersion effect, Franz-Keldysh effect is also used to realize high speed amplitude modulators by controlling the absorption coefficient of the waveguide. Such modulators operate based on the change in the semiconductor bandgap in response to an applied modulating electric field. On silicon photonics platforms, silicon germanium (SiGe) compound is used for this purpose and adjusting the ratio of silicon and germanium can be used to tune the modulator for the desired operation wavelength. While these modulators feature high speed and compact footprint, the extra fabrication steps needed to embed the SiGe or other materials is a drawback compared to the plasma dispersion based modulators.

The interference based amplitude modulators are formed by embedding a phase shifter into their architecture. The intensity of light at the output is a function of the phase shift experienced by the waves traveling through the modulator architecture. The two commonly used modulators of this kind are Mach-Zehnder interferometers (MZI) and various architectures of ring resonator modulators. An MZI modulator split the input light into two paths with phase shifting capability on one or both arms (Fig. 2.6(a)). Adjusting the relative phase shifts of the two paths controls the interference at the output combiner with constructive and destructive interference in the extremes of zero phase shift and π phase shift. Having phase shifters on both arms functioning deferentially can improve the performance of the modulator and reduce its form factor. The simple MZI architecture gates the optical input like an absorption-based amplitude modulator and thus introduces modulation loss. This loss can be avoided by using a directional coupler to combine the two paths at the output, Fig. 2.6(b). Moreover, this architecture provides a differential output optical signal.

The phase shifting can also be used to change the resonant frequency of a resonator. Fig. 2.6(c) shows a ring resonator with 4 optical ports and a phase shifter that can change the resonant frequency of the ring by changing the optical path length that light travels around the ring. By moving the resonant frequency to the signal wavelength and away from it, the input light is switched between the through and drop ports. Since a resonator have a large quality factor, the resonant frequency can be shifted with relatively small phase shift. Therefore, these modulators are superior for their low voltage drive and power consumption. However, this exact same feature makes a ring resonator too sensitive to fabrication mismatches, temperature variations, and other noise and interference sources.

Photodetector

Photodetectors are electro-optical devices that convert optical signals into electrical signals (which is the reverse function of the modulators). While the low optical

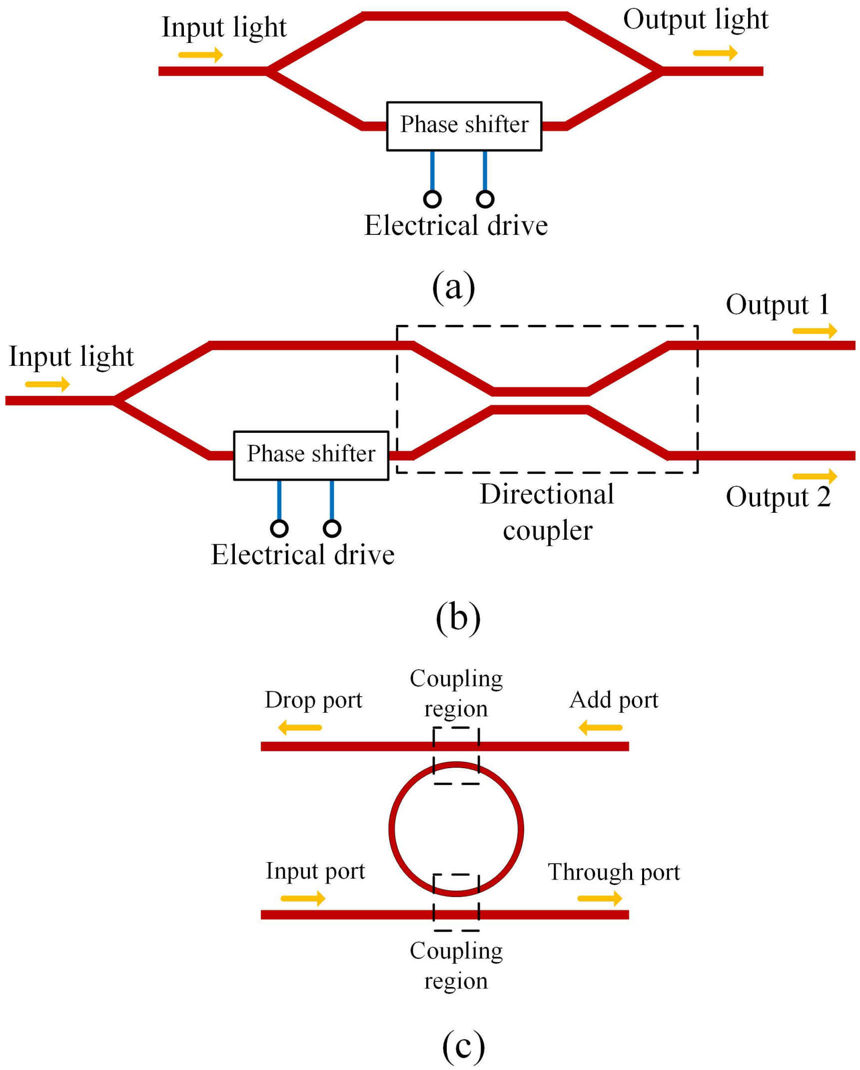

Figure 2.6: (a) MZI amplitude modulator (b) Amplitude modulator without reflection loss (c) Ring resonator-based amplitude modulator.

absorption of silicon makes it a good candidate for designing passive photonic components in the wavelength rages $1.1\mu m < \lambda < 1.8\mu m$, it is not a good photodetector for the same reason. Therefore, germanium and III/V materials have been used to form integrated photodetectors. Integration of germanium-based photodetector is compatible with CMOS electronic platforms and SiGe alloys already exists in CMOS processes. Therefore, germanium is the most common photodetector material used on silicon photonics platforms and can be integrated through chemical vapor deposition and epitaxial growth. However, there is a 4% lattice mismatch between germanium and silicon which leads to mid-gap generation-recombination

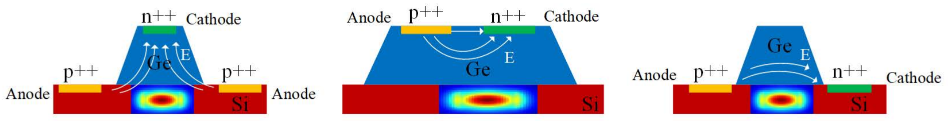

(a) (b) (c)

Figure 2.7: (a) Cross-section of a Ge-photodiode with vertical electric field. (b) and (c) Cross-section of Ge-photodiodes with lateral electric field.

centers and consequently increased dark current for the detector. While hybrid III/V-silicon and InGaAs-based photodetectors can potentially yield higher performance detectors (and even laser sources), the absence of fabrication methods compatible to CMOS mass production lines is a the major drawback that hampered their wide usage.

In Ge-based photodetectors, the interaction of photons and germanium generates electron hole pair which can be separated and collected by applying an electric field. The common architectures for collecting these charges are shown in Fig. 2.2(a)-(c) with vertical and lateral field application. The germanium layer is formed on top of the silicon layer (which can be waveguides carrying light) and construct a PiN photodiodes with germanium being the intrinsic region. Since Si/Ge interface is conductive, in the vertical field structure, the germanium is doped to form a cathode, and p+ doped silicon contacts on the sides are the cathode. The relatively large refractive index of germanium causes the optical field being drawn into it and interact with germanium efficiently. Interaction length, charge swept time, recombination rate, electrical resistivity of the charge paths, etc. defines the characteristics of the photodetector. Speed, responsivity, dark current, and power handling are among the characterises that should be considered in determining the type and geometry of the photodetector.

2.3 Integrated optical phased array

An integrated optical phased array transmitter capable of electrical adaptive beam forming and steering includes a 1D or a 2D array of nano-photonic antennas [46], [60]–[62] and can be used to engineer a desired optical wavefront. The antennas are fed with phase and amplitude adjusted optical signals which are routed by on-chip dielectric waveguides, Fig. 2.8. Such an optical transmitter is suitable for applications such as LiDAR [63]–[67], point-to-point communication [68]–[70], lens-less projection [46], and holographic displays [71]. Here, we first introduce an analytical framework to study the wavefront generation and manipulation on integrated photonic platforms. Then, we discuss the OPA transmitter functionality and explain the relationship between its aperture excitation and far-field pattern. While the operation principle of an OPA receiver is closely related to OPA transmitter, the detailed study of photonic receivers is postponed to Chapter 4.

To study the radiation pattern of a nano-photonic transmitter, here, we consider the far-field pattern, $P(\theta, \phi)$, for an electromagnetically active surface with a general complex field profile of $E(x, y) = a(x, y)e^{i\psi(x,y)}$ on the xy-plane (Fig. 2.9(a)). The radiation pattern of this structure can be derived by breaking the surface into infinitesimal segments $dxdy$. Each of these segments generates a wave and the total far-field radiation pattern of the aperture is the coherent sum of the field generated by the segments. The wave generated by the segment at coordinates (x, y) experiences a path length difference of l_{xy} in traveling towards a point in the far-field at θ and ϕ (elevation and azimuth angles, respectively) compared to the segment at the origin. This path length difference translates to a phase shift of $2\pi l_{xy}/\lambda = 2\pi(xf_x + yf_y)$ where

$$f_x = \frac{1}{\lambda}\sin\theta\cos\phi, \quad f_y = \frac{1}{\lambda}\sin\theta\sin\phi, \tag{2.2}$$

and λ is the free-space wavelength. Therefore, adding the contribution of all the segments through a continuous sum (integral) while accounting for their different path lengths, l_{xy}, the overall far-field radiation pattern is calculated as

$$\begin{aligned} P(\theta, \phi) = \mathcal{F}\{E(x, y)\} &= \iint_{-\infty}^{\infty} E(x, y)e^{-i2\pi(xf_x+yf_y)}dxdy \\ &= \iint_{-\infty}^{\infty} a(x, y)e^{i\psi(x,y)}e^{-i2\pi(xf_x+yf_y)}dxdy. \end{aligned} \tag{2.3}$$

This equation shows that the far-field radiation pattern is a modified Fourier transform of the electric field distribution on the aperture surface.

In a practical implementations, the excitation function, $E(x, y)$, can be sampled at some discrete points and replaced by an array of point sources radiating the samples. These discrete sources can be modeled by impulses (Dirac deltas) for the field profile. Therefore, a finite uniform array with elements at coordinates $(x_m, y_n) = (md, nd)$ (d is the element spacing) has a field profile of

$$E(x, y) = a(x, y)e^{i\psi(x,y)} = \sum_{m,n} a_{mn}e^{i\psi_{mn}}\delta(x - md, y - nd). \tag{2.4}$$

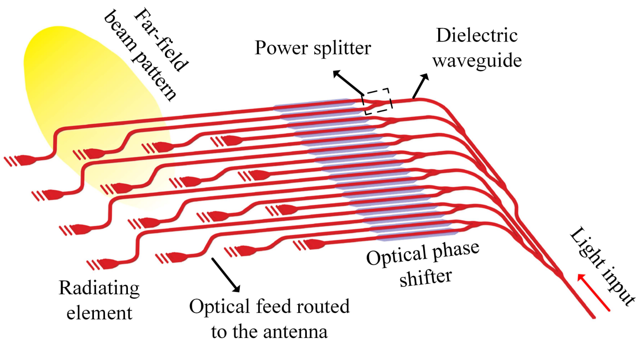

Figure 2.8: Simplified diagram of an integrated silicon photonics OPA transmitter including an input optical signal which is routed on-chip using dielectric waveguides, a power splitter tree, phase shifter network, and an array of radiating elements.

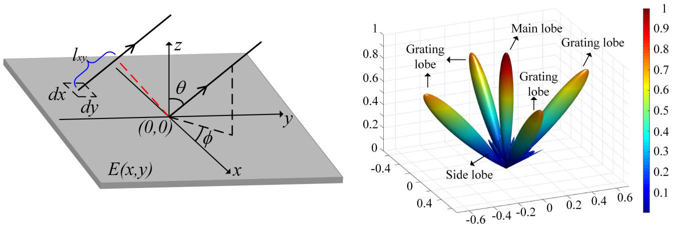

(a) (b)

Figure 2.9: (a) An active electromagnetic surface with a continuous excitation $E(x, y)$. The far-field radiation pattern can be calculated by breaking the surface into infinitesimal segments and count for the contribution of each segment considering its path length difference l_{xy} for angles θ and ϕ. (b) Far-field radiation pattern for a 4×4 uniform array with $d = 1.5\lambda$ element spacing.

Using (2.3) the far-field pattern can be written as the better known expression:

$$P_{array}(\theta,\phi) = \mathcal{F}\{E(x,y)\} = \sum_{(m,n)} a_{mn} e^{-i\frac{2\pi}{\lambda} l_{mn} + i\psi_{mn}}, \qquad (2.5)$$
$$l_{mn} = md\sin\theta\cos\phi + nd\sin\theta\sin\phi,$$

where a_{mn} and ψ_{nm} are the amplitude and phase of the wave radiated by the antenna at (md, nd). While this is the general form of an electromagnetically active aperture consisting a set of point sources, the extended definition of phased arrays covers this general form. Therefore, not only a uniform array of elements with linearly changing excitation phase, but also any aperture including a set of point sources with an arbitrary arrangement as well as excitation phase and amplitude, is alternatively called a phased array.

Due to the Fourier transform relationship, the effect of the sampling on the aperture translates to periodicity in the far-field pattern. In other words, sampling the aperture with sampling spacing of d_x and d_y in the x and y directions, respectively, generates a periodic Fourier transform (radiation pattern) which is the overlap of replicas of the original radiation pattern shifted by integer multiples of sampling rate

$$\begin{gathered} P_{array}(f_x, f_y) = \sum_{(m,n)} P_{cont}(f_x + n\Delta f_x, f_y + m\Delta f_y), \\ \Delta f_x = \lambda / d_x, \quad \Delta f_y = \lambda / d_x \end{gathered} \tag{2.6}$$

with f_x and f_y defined in equation (2.2). However, θ and ϕ only exist for $f_x^2 + f_y^2 \leq 1$ which is called the *visible range* and forms the far-field pattern of the aperture. Frequency components outside of the visible range are evanescent fields and do not propagate.

The sampling of the continuous aperture can be uniform or nonuniform as well as oversampled or undersampled. If the aperture is undersampled (with sampling spacing larger than $\lambda/2$) two replicas of the radiation pattern fall in the visible range and cause a form of aliasing. More details are provided in section 5.3 regarding the properties of the radiation pattern and its Fourier transform relationship to the aperture excitation.

For a simple phase array beam forming, all the elements in the array are in-phase with equal amplitudes. The associated continuous aperture to this setting has a uniform excitation which is a rectangular function (one inside the aperture and zero outside) and leads to a *sinc* shape radiation pattern. Therefore, the pattern has a beam shape at $(\theta, \phi) = (0, 0)$ and smaller peaks at larger angles. If the aperture is sample with $\lambda/2$ spaced elements, there will be only one beam in the pattern. This beam is called the main beam. For an undersampled aperture, with element spacing d of $\lambda/2 < d < \lambda$, the replicas of the main beam are not in the visible range when all the elements are in phase but if the beam is steered to larger angles they will appear in the pattern. These extra beams are called grating lobes. For element spacings larger than λ, the grating lobes are close enough to be present in the visible range even for broadside radiation (main beam at $(\theta, \phi) = (0, 0)$).

The far-field pattern of a 4×4 array with element spacing $d = 1.5\lambda$ and $\psi_{nm} = 0$ for all the elements is shown in Fig. 2.9(b), illustrating the main beam, grating lobes, and side lobes (smaller peaks in the pattern). In addition to the analysis provided above, the radiation pattern of the phased array can be understood as described in the following as well. If $\psi_{nm} = 0$ for all the elements, the radiated waves by the antennas are in-phase at a far distance for $(\theta = 0, \phi = 0)$ and differ in phases for the neighboring angles. Therefore a beam is formed at $(\theta = 0, \phi = 0)$. If the element spacing is larger than $\lambda/2$, constructive interference with all the antennas being in-phase can happen at other angles as well, resulting in grating lobes, Fig. 2.9(b). If a linear phase shift is applied to the excitation at each element (proportional to its absolute coordinates), the Fourier transform of the aperture excitation experiences a frequency shift according to Fourier transform shift properties. Therefore, beam steering is performed by adjusting the phase shift of each antenna feed, ψ_{nm}s, to

$$\psi_{nm} = \frac{2\pi}{\lambda}\big(md \sin\theta_0 \cos\phi_0 + nd \sin\theta_0 \sin\phi_0\big), \tag{2.7}$$

which steers the beam to the angle (θ_0, ϕ_0). In an OPA, directive transmission and beam steering are performed by tuning the relative phase of the optical wave fed to each antenna through electronically adjustable phase shifters, analogous to conventional microwave arrays [72].

While we assumed point sources for radiating the samples in the above discussion which are isotropic radiators, in practice, photonic antennas should be used which can not be isotropic. Assuming identical antennas with radiation pattern $G(\theta, \phi)$, the effect of location on the pattern is the same phase shift caused by the propagation length difference l_{mn} which yields an overall pattern of

$$\begin{aligned} P_{tot}(\theta, \phi) &= \sum_{(m,n)} a_{mn} G(\theta, \phi) e^{-i\frac{2\pi}{\lambda} l_{mn} + i\psi_{mn}}, \\ P_{tot}(\theta, \phi) &= G(\theta, \phi) \times P_{array}(\theta, \phi), \end{aligned} \tag{2.8}$$

which is the product of the array pattern and the individual antenna pattern.

Another assumption for the above derivation is using a two-dimensional array for sampling the aperture. The simpler structure is a 1D array of elements forming the radiating aperture which can be assumed to be along the x axis without loss of generality. While these derivations hold for a 1D array as well, it is more common to ignore f_y and plot the radiation pattern only in the angular range parallel to the x axis which is achieved by simply substituting $\phi = 0$ in the equations and thus

$$\begin{aligned} f_x &= \frac{1}{\lambda} \sin(\theta), \\ l_m &= md \sin(\theta), \\ P_{tot}(\theta) &= \sum_m a_m G(\theta) e^{-i\frac{2\pi}{\lambda} l_m + i\psi_m}, \end{aligned} \tag{2.9}$$

The first demonstrations of optical phased arrays were enabled by the advances in nano-fabrication to implement micron-scale devices [73]–[75]. These early works were an attempt to propose replacements for conventional electro-optical beam scanning devices such as variable prisms and waveguide array scanners. However, they were not fully integrated, had simple architectures, and could not meet the demands of functional system. Therefore, optical phased array technology remained limited to liquid-crystal and MEMS-based optical phased arrays which are bulky devices and suffer from large element size and low speed.

Over the past decade, integrated photonic platforms, mainly pushed by optical fiber communication industry, reached a maturity of providing a large number of various photonic components such as low-loss waveguides, couplers, splitters, modulators, etc. on a single substrate. Designers can now integrate a large number of photonic components on a single silicon chip, and photonic foundries have become more commonplace and offer multi-project wafer (MPW) runs, which enable circuit and system researchers to explore novel photonic integrated solutions. Consequently, simple optical phased arrays with small number of elements in a 1D array were demonstrated with grating couplers functioning as the antenna elements [76]–[78]. A one-dimensional array can only steer a beam in the direction parallel to the array axis. Two-dimensional beam steering using a phased array requires a 2D array aperture which increase the complexity of the system.

The diffraction angles of a grating structure are wavelength dependant. Thus, beam steering has also been demonstrated using a grating-based antenna and wavelength sweeping [79]. If each period of the grating is considered as a radiating element, sweeping the wavelength changes the phase shift that the elements are excited by and diffraction grating angle scans the field-of-view. Therefore, this beam steering mechanism works based on similar principles that a phased array functions while there is no electronic phase shifter to control the phases. Since there is only linear phase increment available by sweeping the wavelength, steering the diffraction angle and thus the beam is possible while arbitrary phase control and pattern adjustment can not be realized through such a system.

Since grating couplers are usually used as nano-photonic antennas in 1D array OPAs and wavelength sweeping yields beam steering in the second direction, these two methods were combined to realize a 2D beam steering OPAs [80]–[82]. However, such OPAs need a more complex and expensive precise tunable laser source, which also compromises its spectral purity and multibeam projection capabilities. Moreover, except for the broadside radiation, wavelength sweeping at other angles should be accompanied by phase shifter adjustments that keep track of the wavelength of the input source.

While 2D antenna array with more than a 1000 element and fixed phase setting has been demonstrated on integrated photonic platforms [60], OPAs capable of single wavelength 2D beam steering using purely electronic element-level full phase control, have been demonstrated for a small number of elements with a limited grating lobe-free FOV [46], [60], [83]. Scaling such 2D arrays to a large number of elements presents a major challenge due to the area required for optical feed distribution, relatively large size of the optical antennas compared to the wavelength, and electromagnetic (EM) interaction between elements. These issues dictate a large minimum inter-element spacing which leads to limited useful FOV due to multiple closely-spaced grating lobes.

For a regularly-spaced phased array, the number and spacing of elements play a central role in its beamforming and beam-steering capabilities by affecting the beamwidth, angular resolution, grating lobe spacing, and power. Increasing the number of elements reduces the beamwidth, while increasing the spacing of the elements (above $\lambda/2$, where λ is the wavelength) results in grating lobes in the radiation pattern. Achieving a small element spacing does not present as great a challenge in one-dimensional (1D) OPAs , where long and narrow elements can be tightly packed. Therefore, a majority of the attempts on scaling the OPA systems focused on 1D OPAs with 2D beam steering capability using wavelength sweeping [61]–[63], [84]–[86].

While large scale 1D array OPAs have been developed extensively showing a great promise for functional fine resolution systems, many challenges remained to realize a functional low-cost OPA system that can eventually compete with other technologies in the market. Moreover, many other possibilities enabled by on-chip wavefront manipulation such as holographic projection [71], [87], visible range [61] and midwave-infrared [88], sensing and complex imaging applications, etc. are remain for future research.

An OPA receiver (RX) is the counterpart to the OPA transmitter. It can form and steer a reception beam electronically and collect light selectively from any desired direction. It also suppresses undesirable light impinging on it from other directions, multipath reflections, or even active jammers. This spatially selective reception is highly valuable in many applications, such as ranging and sensing, volumetric imaging, and point-to-point communication systems. An OPA receiver can be combined with a transmitter to enhance its capabilities or introduce new functionalities. The OPA receiver can be used to collect light from the spot that is being illuminated by the transmitter and reject all the unwanted illuminated points and multipath reflections, to enhance sensitivity that can directly translate to range and accuracy. An OPA receiver can also be beneficial in point-to-point communication systems with multiple free-space optical communication systems to minimize the interference between channels and increase the fidelity of the communication system utilizing its selective directivity. Further discussions about OPA receivers and its analytical framework are postponed to Chapter 4.

Chapter 3

LARGE-SCALE SPARSE 2D OPTICAL PHASED ARRAY

In this chapter, design challenges regarding a large scale photonic transmitter with a 2D array of radiating elements are discussed and the effect of the element number on the FOV is studied. Moreover, the increasing system complexity and power consumption faced by scaling uniform arrays are explained. To address these challenges, methods for designing nonuniform photonic arrays are devised and a two-chip solution low-power scalable OPA with a nonuniform sparse aperture is realized [20]. The implemented OPA with an aperture consisting 128 radiating elements achieves the highest reported grating-lobe-free FOV-to-beamwidth ratio of 16°/0.8°. This performance is equivalent to a 484-element uniform array and translates to at least 400 resolvable spots which is 30 times larger than the state-of-the-art 2D OPAs. Moreover, the compact phase shifters, the row-column power delivery grid, and its high-swing pulse-width modulation (PWM) driving circuit which are designed to reduce the power consumption of the system are explained. Finally, measurement results and comparison with the previously reported OPAs are presented[1].

3.1 Introduction

Among various applications of optical wavefront generation, forming an electronically steerable optical beam has a wide range of applications, such as target detection and tracking, LiDAR, surface metrology, volumetric mapping, optical wireless communication, *etc.* [48], [49]. Systems capable of optical beamforming and steering have been demonstrated in the past utilizing various mechanical and electrical approaches such as using a deflecting mirror [89], MEMs arrays [90], [91], gradient refractive-index-based systems [92], and liquid crystal cell arrays [93]. However, these approaches suffer from bulky form factor, slow steering speed, high cost, and poor reliability. Moreover, many of these methods simply steer an existing beam and are generally incapable of arbitrary waveform generation.

On the other hand, coherent arrays, such as phased arrays, are capable of generating and manipulating wavefronts (including forming and steering beams) through the control of the relative phase and amplitude of the feed to each radiating element.

---

[1] The work presented in this chapter was done in collaboration with Aroutin Khachaturian.

These arrays are electronically controlled, do not require any mechanical movement, and have been used extensively in RF, microwave, and mm-wave range of the electromagnetic spectrum [72]. Realization of such phased arrays in the optical domain can open up many new opportunities as well as reduce the cost and form factor.

In a uniform phased array with regularly-spaced elements, beamforming and beam-steering capability strongly depend on the number and spacing of elements, which determines the beamwidth, angular resolution, grating lobe spacing, and optical power in the lobes. For a given element spacing smaller beamwidth is achieved by increasing the number of elements and element spacing larger than $\lambda/2$, where λ is the wavelength, leads to often undesirable grating lobes in the radiation pattern. For one-dimensional (1D) OPAs [61], [62], [84], [85], achieving a small element spacing does not present as great a challenge where long and narrow nano-photonics antennas can be tightly packed. However, 2D beam steering with a 1D OPA is realized through wavelength sweeping that requires a more complex, expensive, spectrally pure, and precise tunable laser source. Electronically controlled beamforming and steering through phase shift adjustment requires a 2D OPA which is capable of single wavelength 2D beam steering. Such OPAs have been demonstrated for a small number of elements with a limited grating lobe-free field-of-view (FOV) [46], [60], [83]. However, scaling 2D OPAs to embody a large number of elements faces major challenges due to the chip area required for optical feed distribution, relatively large size of the nano-photonic antennas (compared to the wavelength), and wave interaction between antennas. Consequently, the OPA's useful FOV was limited due to the large minimum inter-element spacing which leads to multiple closely-spaced grating lobes.

In addition to the aperture scaling, increased power consumption of both the phase shifters and their driver circuitry scaling with the number of elements used for the optical phased arrays poses a serious scaling limit for practical applications. In order to achieve full electronically 2D steering and enable phase calibration to compensate for fabrication mismatch, crosstalk between phase shifters, and thermal and electrical drifts, a useful OPA needs to feature independent phase control for each antenna. However, this results in high power consumption, increases the interface complexity for phase shifter electrical access, and requires a larger chip area occupied by the system.

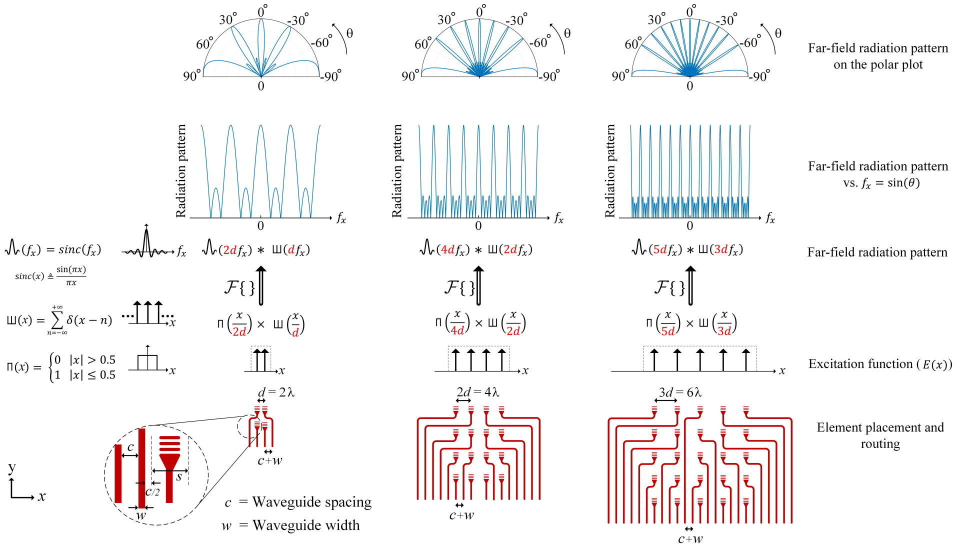

Figure 3.1: Illustration of the large inter-element spacing imposed by the optical feed distribution as the array size scales. The excitation of the three different 2D arrays are modeled as windowed impulse trains. Fourier transform of the excitation yields the far-field pattern of the array. As the element spacing of the array increases and impulses are spaced further apart, grating lobes get more compact as the *scaling* theorem predicts for Fourier transform.

3.2 Silicon photonics OPA with a sparse aperture

To implement an OPA with a 2D beam steering capability via pure control of the antenna feed phase shifts, a 2D array of nano-photonic antennas must be fabricated on the chip. In a single photonic layer process, one layer is available for routing the phase shifted optical signals to the antennas using dielectric waveguides [46] (as shown in the simplified model of an integrated OPA in Fig. 2.8). Beamforming and steering are then performed by controlling the electrically tunable phase shifters and the relative phase of the optical wave fed to each antenna, similar to conventional microwave arrays [72]. While this does not affect small arrays severely, as the array scales and the number of antennas increases, the spacing between the antennas will need to increase accordingly to accommodate the optical routing waveguides. Moreover, a minimum spacing between adjacent waveguides and antennas is required to keep the optical coupling below a satisfactory level. Consequently, this increase inter-element spacing leads to a larger number of grating lobes which are closely spaced in the array patterns of the OPAs, as shown in Fig. 3.1.

As explained in section 2.3, the far-field radiation pattern of an aperture is related to its field distribution through a modified Fourier transform. Therefore, the area occupied by the optical feed distribution and increased inter-element spacing affects the far-field radiation pattern, which is visualized in Fig. 3.1. In this figure, three exemplary uniform 2D arrays are illustrated, showing that their element counts and associated feed distributions are scaling from left to right. The field distribution on the apertures, $E(x, y)$, and their far-field patterns are shown for $\phi = 0$ to simplify the visualization while the arguments are equally applicable to the 2D patterns. As explained in section 2.3, for $\phi = 0$, l_{xy} reduces to l_x and the Fourier transform will reduce to a single variable function in terms of $f_x = \frac{1}{\lambda}\sin(\theta)$, as shown in Fig. 3.1. The field profile of these three arrays are modeled by a finite number of uniformly spaced impulses which are spaced further apart as the number of elements grows due to routing constraints. Mathematically this can be expressed as the product of an infinite impulse train with impulse spacing of kd, *i.e.*, $\sqcup\!\sqcup(x/kd)$ and a windowing pulse of $\prod(x/Nd)$. Therefore, the far-field pattern is the Fourier transform of this product, which can be written as the convolution of an impulse train and a *sinc* function (defined as $sin(\pi x)/(\pi x)$) which are the Fourier transforms of the two functions $\sqcup\!\sqcup(x/d)$ and $\prod(x/(Nd))$, respectively. These far-field patterns are plotted vs. f_x and vs. θ on the polar plots in Fig. 3.1. Based on the *scaling theorem* for Fourier transform, stretching $E(x, y)$ by a factor of α squeezes its Fourier transform by the same factor. Therefore, scaling the 2D OPA aperture in this setting reduces the grating lobe spacing, leading to closely compacted grating lobes, and consequently, a limited useful FOV.

As explained in the previous section, the relatively large size of the dielectric optical waveguides and antennas — and consequently, the large area required for routing optical signal — is the main obstacle in usefully scaling the two-dimensional photonic array. Generally, dimensions of dielectric photonics components and waveguides are enforced by the wavelength of interest ($\lambda = 1.550$ nm in this design) and the refractive index (for silicon, $n = 3.47$). Despite silicon's relatively large refractive index, achieving low loss and sufficient mode confinement at $\lambda = 1.550$ nm still leads to large footprint relative to the wavelength. While the routing limitation could be alleviated by using a multi-layer photonics process to some extent, the complexity, cost, and area overhead of such platforms present alternative challenges to 2D photonic array scaling.

In general, the waveguide routing space is defined by the array circumference which is $4(N - 1)(d - s)$ for a uniform $N \times N$ array with element spacing d and antenna size s. Therefore, the maximum waveguide count that can be routed into the array for feeding the $N \times (N-1)$ interior elements is $4(N-1)(d-s)/(c+w)$, in which w is the waveguide width and c is the minimum waveguide spacing required to have acceptable low coupling (Fig. 3.1). Therefore, the maximum number of antennas that can be placed in the array, N_{max}, is limited by

$$N_{max} \leq \frac{4(d-s)}{c+w}, \tag{3.1}$$

which indicates that scaling the array necessitates an increased element spacing as well. Moreover, equation (3.1) assumes that all the four sides of the aperture can be used for routing. However, in practical designs with photonic antenna ports on one side of the antenna, the minimum waveguide bend radius that should be observed to avoid high bend loss reduces the effective available room for routing and further decreases the maximum number of elements embedded in the array.

The discrete radiating elements which are used to sample and approximate $E(x, y)$ can also have nonuniform inter-element spacing creating a sparse array. Although uniform arrays are mathematically more tractable and commonly used, a sparse array can potentially be designed to have extra free space in the aperture for the optical feed distribution needed to implement a large scale OPA. Two exemplary arrays in Fig. 3.2 illustrate the feasibility of scaling a sparse array as opposed to a uniform array. The sparse array can accommodate more elements in the array (41 elements compared to 16 elements in Fig. 3.2) and achieve a narrower beamwidth. In addition to the scaling feasibility, there are additional degrees of freedom for designing a sparse array which can be used for adjusting the array factor. Since the aperture of the sparse array is larger than a uniform 41-element array, a narrower beamwidth is also achievable. Since the elements are placed on a not-fully-populated uniform grid (all the inter-element spacings are divisible by a common unit), the radiation pattern is a periodic function of f_x and f_y with the same period of a fully-populated uniform array on the same grid and thus the same grating lobes spacing.

Conventionally, electronic systems benefited from sparse arrays for applications with a narrow beamwidth requirement [94]. A large aperture size leads to a narrow beamwidth but the complexity, handling difficulties, and cost of the large number of elements in a large uniform array with wavelength-scale element spacing is undesirably immense. Some applications require a narrow beamwidth while not being restricted by the antenna gain; in these cases, a sparse array can be formed

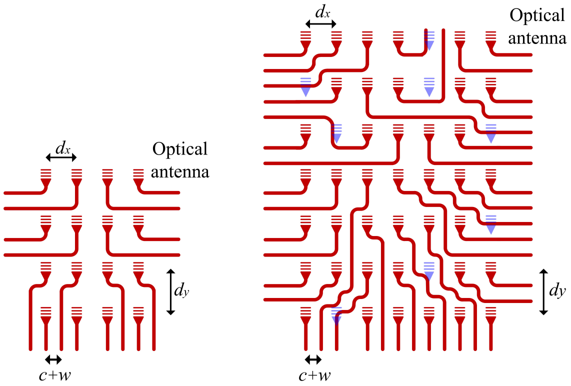

(a) (b)

Figure 3.2: (a) A 4×4 uniform array with element spacings d_x and d_y. The size of the array with this spacing is limited to the optical feed distribution feasibility (b) A 41-element nonuniform sparse array on a 7×7 grid with the same grid spacing of d_x and d_y that results in the same grating lobe-free steering range. Blue antennas show the non-occupied spaces on the grid. The sparse array achieves a larger scale and a better performance due to the larger number of elements.

by removing some of the elements in the array at the cost of the increased average side lobe power (within the tolerance of the system). Although the the radiation pattern is directly impacted by the selection of the elements to be retained in the array, there is no closed form solution relating the optimum set of elements to the array properties. Therefore, various optimization techniques [95]–[98] as well as random element placement methods [99], [100] were investigated in the literature which are mainly focused on reducing the number of elements under the condition of a maximum peak or the average side lobe level.

For an sparse array, as the number of elements increases its side lobe level reduces[94]. However, the rate of this reduction is slower than a uniform fully-populated grid which leads to a smaller directivity for sparse arrays. However, a sparse OPA brings many advantages such as significantly lower complexity, acceptable array performance, and smaller number of elements. Moreover, in designing a sparse OPA, amplitude of the optical wave fed to each radiating element can also be adjusted in addition to the element locations to achieve a better performance as has been done for electrical phased arrays [101], [102].

As explained above, a sparse array structure can be used to realize scalable OPAs. Therefore, the purpose of using a sparse array for OPAs is to increase the number of elements in the aperture, which stands in marked contrast to conventional sparse array designs in the RF and microwave domains, where thinning the array is an attempt to minimizes the number of elements. Moreover, OPA aperture faces a a stronger criteria beyond a well-shaped radiation pattern which is the feasibility of routing optical waveguides and implementing the feed distribution network. Therefore, conventional sparse array design methods as well as the limitations they face are not relevant here, and a different design approach is required for designing a sparse aperture OPA.

3.3 Aperture design

The aperture of the transmitter is a collection of nano-photonic antennas. These antennas are fed with processed (phase and amplitude adjusted) guided optical waves carried by on-chip waveguides. The function of the antennas is to interface the guided mode light with free-space mode propagation. The characteristics of the antenna such as radiation efficiency, FOV, and bandwidth directly affects/defines the performance of the system. Moreover, the relative placement of the antennas in the array controls sidelobe, directivity, and beam-efficiency. In integrated silicon photonics platforms, the design of both nano-photonic antennas and array design faces serious limitations due to the planar nature of the low-cost integrated solutions as well as large sizes of the nano-photonic components. To achieve high performance OPA systems, designing small footprint antenna, while efficient with high radiation efficiency, is essential to reduce the element spacing and increase the steering range (FOV) of the system. Since the footprint of a dielectric antenna is usually larger than the wavelength, to fit the antennas in the array, a well-designed sparse array aperture with inter-element spacings which yield low sidelobe levels is required. In this section, the detailed design metrics of the antenna are discussed and a compact efficient nano-photonic antenna is presented. Moreover, using the designed antenna, a sparse aperture array with low sidelobe performance is demonstrated.

Nano-photonic antenna design

A nano-photonic antenna on integrated platforms is usually formed by patterning a dielectric material (with no metallic part) to avoid high optical loss in the antenna structure. Therefore, the radiation efficiency of a transmitter antenna is limited by its input matching. A well-designed antenna is adjusted to have an acceptable S_{11} (usually less than 20 dB). However, due to the relatively symmetrical geometry of the chip, only a fraction of the couple light to the antenna is directed towards the surface of the chip and into the free-space. The portion of the light that is radiated towards the substrates can reflect and cause stray light and blind spots in the FOV of the system. Moreover, for a compact antenna structure, a fraction of the light continues propagating forward and does not get deflected. This portion will also turn into stray light after interacting with other structures on the chip which is different for each antenna. Therefore, it is important to optimize the antenna design for maximally radiating upward into the free-space. In addition to the radiation efficiency, the angular range on which the radiated wave is distributed (FOV) is one of the key parameters in the system specifications. The antenna should provide a sufficient FOV for beam steering while filter out the unwanted side-lobes and grating lobes outside of the FOV of the system. Moreover, any unwanted peak in the antenna pattern outside of the FOV will result in an effective power loss. Conventionally, integrated grating couplers have been exploited as nano-photonic antennas on silicon photonic platforms [46]. However, the large footprint of a standard grating coupler, which is on the order of several wavelengths, limits the FOV of the system and the minimum element spacing, which drastically reduces the maximum achievable grating-lobe-free steering range.

Here, a custom nano-photonic antenna which does not rely on periodic grating and has compact dimensions of 2 µm by 5 µm is designed (shown in Fig. 3.3(a)). This antenna is includes a tapered slab mode converter for broadening the input optical mode and match it to the antenna aperture. Moreover, multiple pieces of dielectric slabs are patterned and etched perpendicular to the wave propagation direction to from the antenna aperture for diffracting and deflecting the electromagnetic energy into free space. In addition to these pieces, a thinner slab layer aligned with the propagation direction helps confining the light in the antenna to avoid power leakage towards unwanted directions, as well as two side pieces which are both diffract the sideways propagating light as well as providing a matched waveguide for the routing network. The antenna aperture consisting these dielectric slab pieces are holistically designed and optimized to achieve a compact high performance antenna. The antenna for which the radiation pattern is shown in Fig. 3.3(b) achieves 51% radiation efficiency at a wavelength of 1.550 nm.

Sparse array design

As discussed previously, the routing feasibility is a strict constraint on the realizable planar arrays with single routing layer. Therefore, the designed array should be sparse to open enough room for the routing waveguides while achieving the targeted array pattern specifications. For designing the array and generating a set of locations for the elements, here, we developed an optimization algorithm that searches the

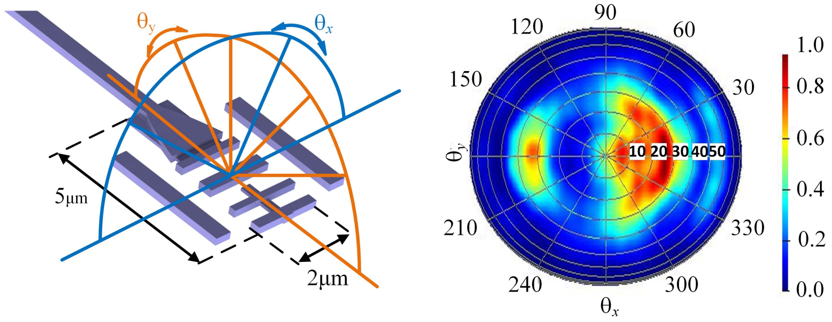

(a) (b)

Figure 3.3: (a) Structure of the designed compact nano-photonic antenna with dielectric slabs as diffracting aperture (b) Far-field radiation pattern of the antenna.

design space for the element coordinates that yield the desired array specifications. This algorithm which is based on the genetic optimization search [103] considers the feasibility of the feed distribution, average side lobe level, peak side lobe level, and the beamwidth. In optimization settings, the maximum peak for the sidelobe is allowed to be 16 dB less than the main beam in its vicinity and as large as 10 dB relative to the main beam at the edge of the FOV. The sidelobe level is relaxed for the large angles, far from the main beam, because of the extra suppression which will be provided by the antenna pattern and adjust the overall system pattern. While achieving lower sidelobe levels is possible, the extra degrees of freedom in the design space are put into obtaining a narrower beamwidth. A narrower beam width will effectively translate into a lower power consumption for the system as well since a smaller number of elements and accordingly phase shifters will be used to achieve the target system resolution compared to a larger uniform array that yields the same beamwidth.

In a Genetic algorithm each member of the design space is represented by a binary sequence which encodes the design parameters to uniquely represent a solution. This string of binary values is called DNA in analogy to its biological definition and a cost function is used to evaluate the performance of each DNA. The algorithm starts with an initial population of candidate solutions, which is a set of DNAs that form the first generation of the *society*, and through an evolutionary process searches for the solution that maximizes the cost function [98]. Each evolution step is a sequence of crossover and mutations to generate the next generation of the society using a pair of *parent* solutions for each new member, followed by evaluating the new members and removing the members with lowest cost value from the society (*natural selection*).

Every crossover generates two new members out of two current members which doubles the population and natural selection readjust the population by keeping the fittest half of the society. Iteration of this process leads to the evolution of the society and getting closer to the global optimum solution. The mutation operation in a genetic algorithm tries to avoid/escape the numerous non-global optimum points in the search space, which is an essential feature for sparse array design.

Among search algorithms in design spaces with many local extremum, Genetic algorithm is a suitable choice for sparse array design with elements on a grid since a single bit can be used to represent the absence/presence of each element. Therefore, A small length DNA can precisely represent each candidate solution and enable a fast thorough search. It worth noting that this is not the case for design spaces with continuous parameters, for which every variable in the DNA needs to be digitized with a finite number of bits, resulting in a trade-off between the accuracy of achieving an optimal solution (or potentially missing it) and the runtime. Here, the optimization is performed on a 27 by 27 grid array with 128 elements present and the rest of the grid points empty. However, it fully lend itself to larger search spaces and is suitable for designing larger scale apertures with more elements and different design criteria as well. The number of evolutionary steps required for reaching an optimum point depends on the size of the desired array and search space. For the 128-element array placed on a 729-spot grid presented here, the maximum number of 1000 generations is considered. The optimum result is achieved approximately after 500 generations and the extra 500 iterations are performed to demonstrate the convergence. The number of grid spots is experimentally adjusted to 729 spots which is large enough to provide the room required for routing with minimum sparsity.

Figure 3.4 shows the flowchart diagram of the designed algorithm. Since the algorithm operates on a 27 by 27 grid array, each solution is represented by a DNA of 729 (27x27) bits in length in which 128 of them are “1". This binary sequence defines the location of the 128 elements base on which the feed distribution network is designed and the array pattern, side lobe level and beamwidth are calculated. The first generation of the society is created randomly such that there is a large diversity of genes with different members having good features of a subset of optimization criteria for the following generations to *inherit*.

In each iteration, members of the society are randomly shuffled and then paired as parents to create the next generation. From a random location in the DNA of the

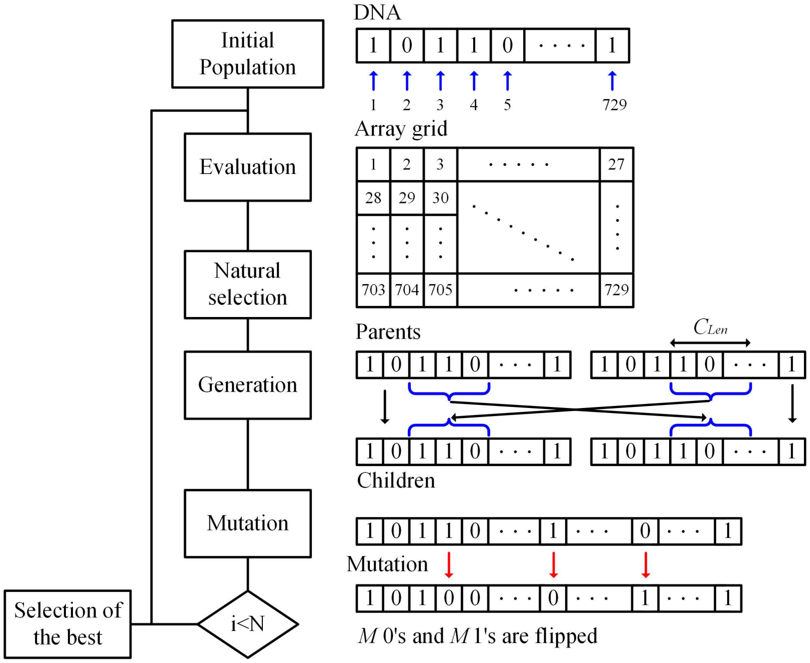

Figure 3.4: Flowchart of the genetic algorithm used for sparse array design.

parents a sequence of length C_{Len} bits is chosen that divides the DNA into two pieces: the chosen sequence and the rest of the DNA. The two children are produced to have one piece of each parent. This crossover process is followed by the mutation operation on the children which is implemented by randomly flipping M bits of their DNA with value of “0" and M bits with the value of “1". Therefore, the number of “1"'s in the DNA string remains constant (128). The generated new DNAs evaluated for a cost value according to their array factor characteristics and feed distribution feasibility, and then added to the society, doubling its population. Finally, through the *natural selection* step, the lower half of the population with the lowest cost value are removed, adjusting the population for the next iteration.

The cost value which is the measure of fitness of the society members is calculated by assigning scores to the array's sparsity (local crowdedness), the beamwidth, and the maximum and average side lobe levels of each member. The weighted summation of these scores are used as the final cost value. The weight of the summation are adjusted manually after multiple iterations by observing the behaviour of the society to achieve a solution that meets the desired characteristics of the array geometry and pattern. The final result of the designed algorithm which is the 128-element aperture with a grid spacing of 5.6 µm= 3.6λ implemented in this work is shown in Fig. 3.5. This grid spacing is limited by the antenna size and leads to a 16° grating

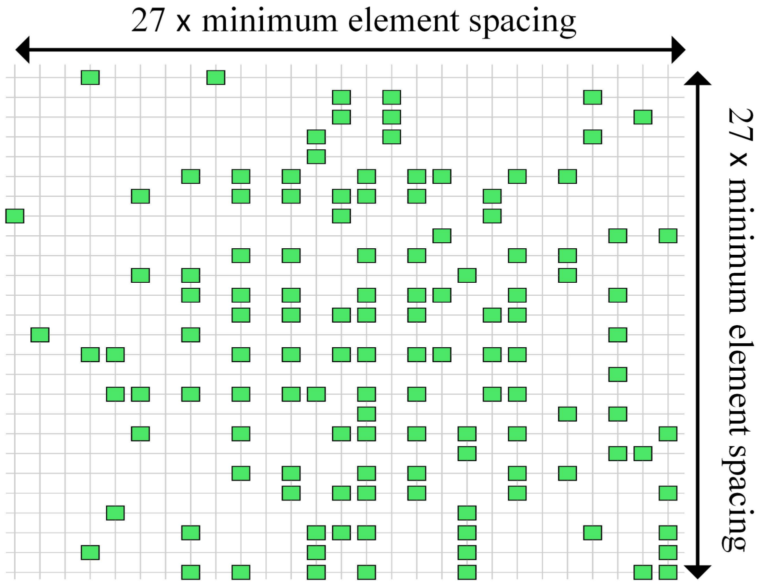

Figure 3.5: The designed 128-element sparse aperture on a 729-spot grid.

lobe spacing in the array pattern. The peak side lobe level near the main beam is less than −16 dB, −10 dB at far angles, and average side lobe level of −21 dB. Since the antenna pattern is maximized at the center of the FOV and the overall OPA pattern is the product of the antenna pattern and the array pattern, as the beam is steered away from the center of the FOV, side lobes are amplified by the antenna pattern while the main beam is partially suppressed leading to degradation of the side lobe rejection performance. On the other hand, the antenna pattern severely suppressed the grating lobes and minimized the power leakage outside of the FOV to about 7 dB.

Figure 3.6 shows the designed aperture with fully routed feed distribution network. The designed antenna in the previous section is embedded in the aperture and placed at a 45° angle relative to the aperture coordinates which provides the optical routing pass-ways from two sides of the aperture without sharp bends. Avoiding sharp bends is important since the light cannot be confined within the waveguides properly and leads to high optical loss. Therefore, the other two sides of the aperture include less feed routings to have enough room for the bends. Figure 3.7 shows the array pattern of the designed aperture for $\phi = 0$. This array achieves a beamwidth of 0.64° and a grating-lobe-free steering range (grating lobe spacing) of 16° which is equivalent to the same parameters of a uniform array with 484 elements on the same grid.

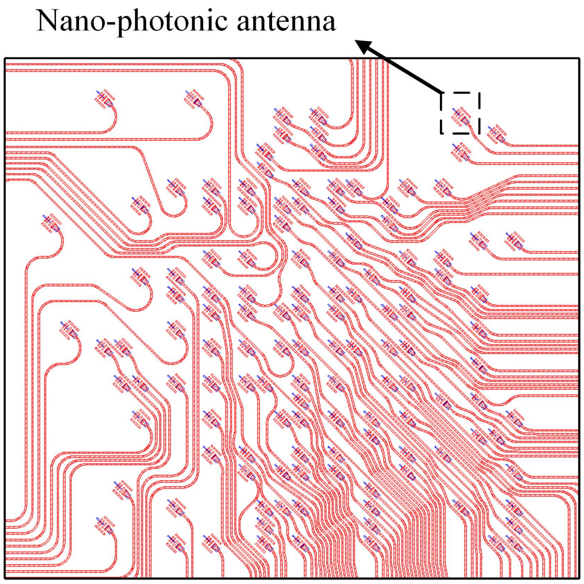

Figure 3.6: The sparse aperture with embedded nano-photonic antennas and optical feed distribution routing network.

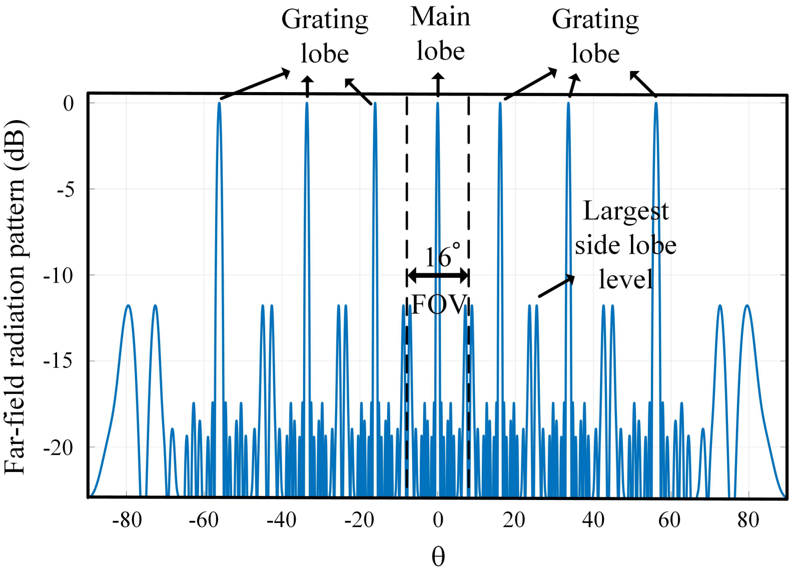

Figure 3.7: Far-field radiation pattern of the designed sparse array for $\phi = 0$.

To demonstrate the scalability of this work, the above procedure is used to design a 512-element sparse array on a 108 by 108 grid (11664-spot grid). Therefore, the number of elements in this array is 4 times larger and the aperture area is 16 times larger (4 times more sparse) compared to the 128-element array. On the same grid spacing of 5.6 µm, this 512-element array achieves peak side lobe level of less

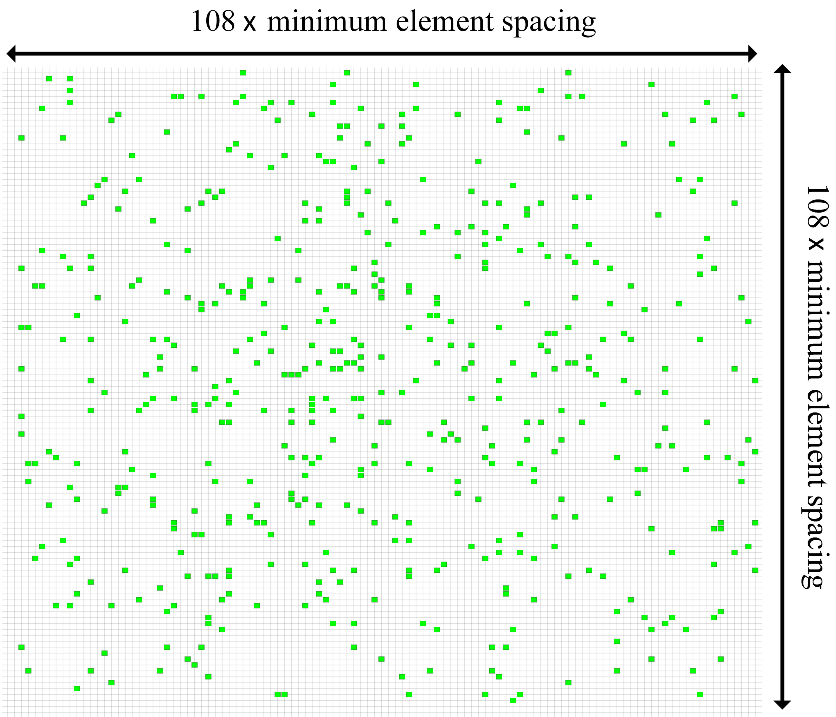

Figure 3.8: The designed 512-element sparse array aperture placed on a 11,664-spot grid.

than −19 dB and beamwidth of 0.14°. Figure 3.8 and Fig. 3.9 show the element locations on the aperture and the far-field radiation patterns of the 512-element array, respectively. The two array designs demonstrated here incorporate only phase control for the antenna feeds and assume uniform amplitude distribution. Further performance improvement can be achieved by designing a passive splitter network with non-uniform amplitude distribution or adding the amplitude control capability.

3.4 Phase shifter network

For controlling the beam shape and steering it to an arbitrary azimuth and elevation angles, a dedicated phase shifter for each radiating element is required. Moreover, for a good controllablity, it is essential to have low-cross-talk phase shifters which can be controlled independently and provide full 2π phase shift to calibrate the fabrication induced phase offsets in the optical paths. These phase offsets are the result of mismatches and non-idealities of the fabrication process that are caused by small variations in the effective index of the modes in integrated dielectric waveguides [104]. The phase error accumulating along the waveguides due to these variations leads to fixed phase offsets for which the statistical standard deviation increases with

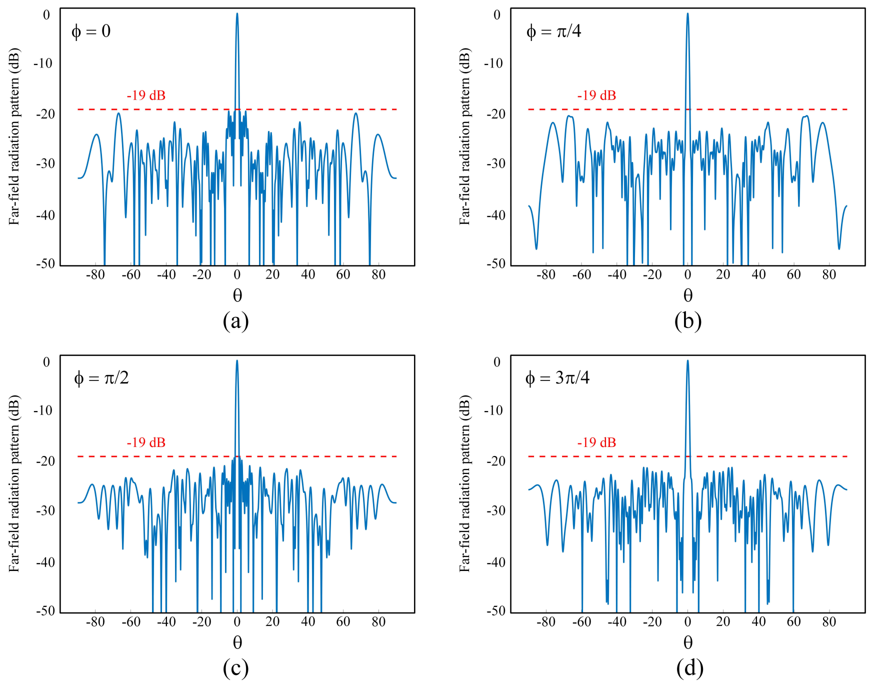

(a) (b) (c) (d)

Figure 3.9: Simulated far-field radiation pattern of the 512-element sparse array with $\lambda/2$ grid spacing for (a) $\phi = 0$ (b) $\phi = \pi/4$ (c) $\phi = \pi/2$ (d) $\phi = 3\pi/4$. To illustrate more details of the pattern it is plotted for grid spacing $\lambda/2$ which contains all the information about the pattern, thus, including only a single lobe in the visible range. Increasing the grid spacing broadens the visible range and leads to the appearance of periodic repetition of the same pattern and grating lobes.

the waveguide length. In addition to these phase offsets, drift and cross-talk between the phase shifters introduce extra factors of error in the zero-bias phase accuracy of the optical signals fed to the nano-photonic antennas, necessitating full phase shifter control. On the other hand, increased power consumption of the phase shifters and the electronic drive circuitry with the scale of the array present challenges in the realization of a large scale OPA. To address the power consumption of a large scale OPA, here, we designed a PWM driven row-column power delivery network for controlling the tunable optical phase shifters. This power delivery network scales with the square root of the number of elements in the array and thus significantly reduces the number of phase shifter drivers and their power consumption for a large scale OPA. In this section, the design of the individual phase shifters and phase shifter network is discussed and the electronic power delivery circuitry is explained in the next section.

Phase shifter

The desired characteristics of a phase shifter in OPA design are optical insertion loss, tuning power consumption, and crosstalk with other neighboring phase shifters. Thermal phase shifters are advantageous due to their negligible optical insertion loss and lower power consumption compared to other types of integrated phase shifters and modulators [105]. Accordingly, integrated thermal phase shifters with nano-heater controllers have been used in many recent OPA demonstrations [60], [62], [63], [83]–[86], [106]. The operation of the phase shifter is based on the temperature dependence of the silicon refractive index. At room temperature, the temperature dependence of silicon refractive index is $\beta = dn/dT = 1.86 \times 10^{-4} K^{-1}$ [58] at a wavelength of 1.550 nm. Therefore, a phase shift of $2\pi\beta l \Delta T/\lambda$ is introduced to the light propagating for a length l if the waveguide temperature is increased by ΔT. Providing enough temperature change yields a 2π phase shift which is required for the phase shifter functionality in the system.

Thermal crosstalk is the primary coupling mechanism between phase shifters. Due to the variable power consumption of the phase shifter versus the phase shift it provides, local heat generated at each phase shifter varies and its leakage to the other phase shifters and photonic structures on the chip affects their performance and in particular their phase shift. It should be noted that this form of crosstalk is not specific to thermal phase shifters and a broad range of nano-photonic phase shifters which have large enough power consumption to thermally affect the neighboring structures suffer from the same effect. Crosstalk disturbance on the phase tuning capability and beamforming quality gets more exaggerated as the OPA scales and more phase shifters are embedded in the system. Therefore, designing a compact and thermally isolated phase shifter is crucial for a large scale OPA.

Here, a power efficient spiral thermo-optical phase shifter is designed which benefits from a compact footprint and negligible crosstalk with the neighboring phase shifters. The schematic and thermal simulation results of this phase shifter is illustrated in Fig. 3.10. In this structure, a 300 µm long dielectric waveguide is wrapped in the form of a spiral accompanied by a doped pieces of silicon layer which form an electrical resistor. There is more than 1 µm clearance between the resistor parts and the optical waveguide to avoid the interaction of the optical wave with the doped region and induce a negligible optical insertion loss. There resistor width and length are adjusted to yield a 1 kΩ resistor. Passing an electrical current through the resistor increases the local temperature due to the generated heat and results in a longer op-

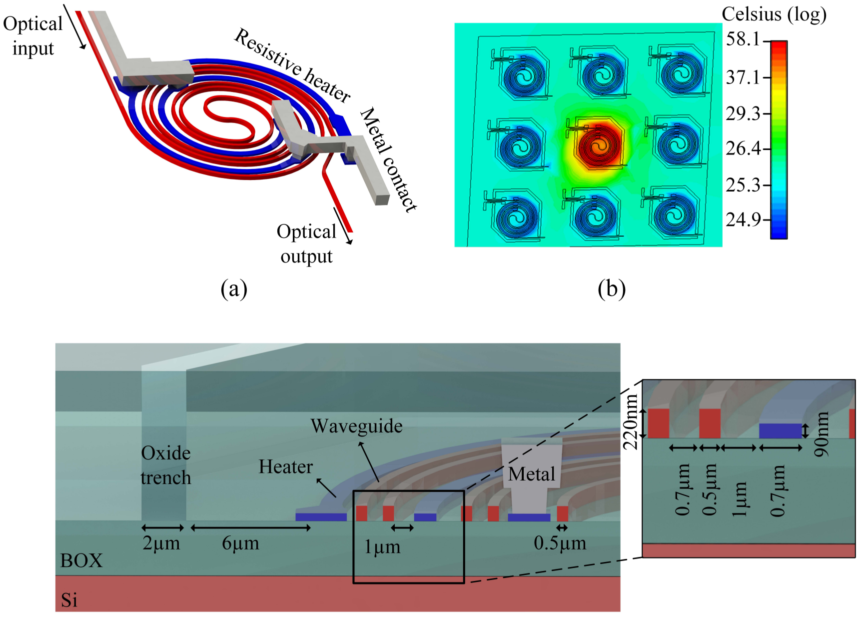

(a) (b)

(c)

Figure 3.10: (a) Schematic of the designed compact spiral phase shifter (b) Thermal simulation of the phase shifter showing temperature change in and outside of the phase shifter structure (c) Cross section of the phase shifter (not to scale) showing the dimensions and sizes of the design.

tical path length, which corresponds to a certain amount phase shift. Therefore, the phase shift is a function of the induced current. For 18 mW of power consumed by this distributed resistor, a phase shift of 2π is experienced by the light at the output the phase shifter. The compactness of the phase shifter is one of the key factors to obtain a high lateral thermal isolation. To further increase the isolation between the neighboring phase shifters, an oxide etch offered by the fabrication process is placed around the phase shifter unit to reduce the lateral thermal conductance and crosstalk. Therefore, the shortest heat exchange path for the phase shifter is through the 2 µm thick BOX layer to the substrate which defines the thermal time constant of the phase shifter. The high thermal conductance of silicon provides a uniform temperature across the bulk to the first order which does not contribute to thermal crosstalk between the phase shifters if all the optical paths are length matched on the chip. Therefore, here, the phase shifters are placed more than 20 µm apart to achieve a low thermal cross-talk.

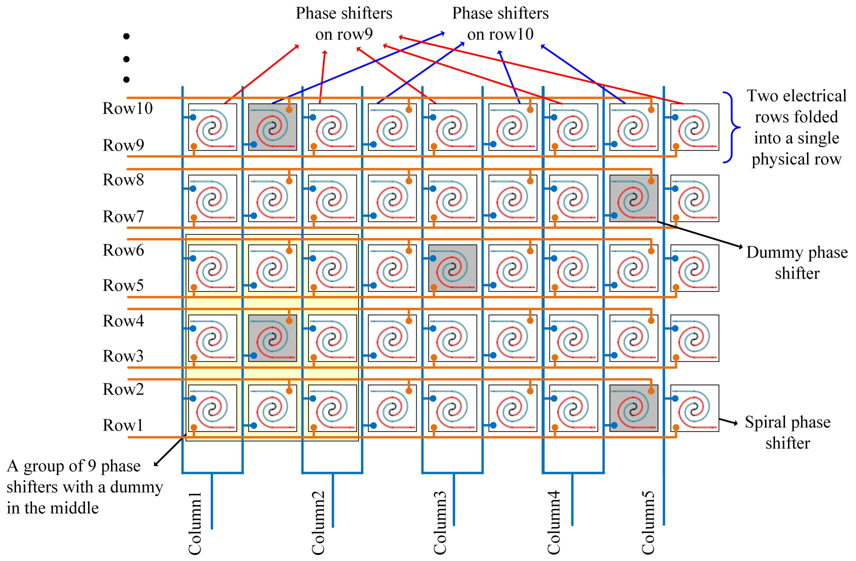

Figure 3.11: The schematic of the designed folded row-column electrical access grid for the phase shifters.

Row-column power delivery network

To provide a scalable and compact electrical interface for the phase shifter power delivery and activation, a row-column access grid is designed connecting each phase shifter to a unique row-column pair. Figure 3.11 shows the structure of the power delivery grid in which the 128 phase shifters, one for each radiating element, in addition to 16 dummy phase shifters, are placed in a 16×9 row-column grid. However, the electrical connection of the phase shifters to grid is realized through a a 32×4 matrix (columns 1-4) plus a column of 16 rows (column 5). In other word, the electrical interface is designed as a folded ow-column network in which 8 of the physical columns form 4 pairs with the columns of each pair being jointly driven while their associated phase shifters being connected to separate rows. One major advantage of this folded architecture is the reduction of absolute and relative optical path length on the chip, which corresponds to lower loss and higher coherence between the optical waves fed into the antennas. Moreover, the physical length of the electrical routing on each columns is reduced by half, which leads to lower line resistance, or equivalently, a smaller metal width for the electrical routings. The reduced metal width in turn decreases the optical loss induced by the interaction of the metal lines with light and reduces the overall chip area due to the more compact metal routings.

The dummy phase shifters, which are identical to the other phase shifters, are electrically connected to the row-column power grid but optically not active (not connected) are uniformly distributed in the network. There is a dummy phase shifter at the center of each group of 9 phase shifters (Fig. 3.11) in the row-column grid. While silicon has a high thermal conductivity, to further reduce the temperature non-uniformity in the bulk, and accordingly the cross-talk between phase shifters, the dummy phase shifters are actively adjusted and powered such that the local temperature of the bottom bulk silicon is controlled and the temperature gradient of the bulk is minimized.

The number of required phase shifter drivers is significantly reduced from 144 (for an individual access network) to 37 in the folded row-column architecture, correspondingly reducing the electronic circuit complexity. However, due to the shared rows and column between the phase shifters, a time sharing mechanism should be implemented to deliver power to the phase shifters at each column sequentially. This necessitates a dedicated electronic driver circuitry, which is discussed in the next section.

3.5 Phase shifter network driver

Using a DAC to drive the rows of the phase shifter network (similar to earlier works [62]), results in a large power consumption by the output stage of the driver. This unnecessary power consumption comes from the voltage drop on the DAC output. For a given supply voltage, a fraction of the voltage is delivered to the row and the rest has to be dissipated on the electronic circuitry itself. To improve the efficiency of the driver circuitry, PWM deriving signals are used to deliver power to the rows. Since the PWM driver is a switching mode circuit, either the current or voltage across the switch will be small at any instant of time leasing to a superior power consumption compared to DAC. Since multiple phase shifters on different columns share the same row, the power delivery to the phase shifters on each row is time multiplexed. Therefore, the rows of the network are driven periodically such that in each cycle each column is switched to the positive supply voltage for one fifth of the cycle while the rows are switched accordingly to ground for a digitally adjustable period of time for each column. Therefore, five PWM signals deliver power to the phase shifters sequentially and the width of the pulses defines the amount of power delivered to each phase shifter and its effective phase shift, accordingly.

To further illustrate the low power consumption nature of the PWM driver in this design, the simplified model of Fig. 3.12(a) is considered. The two main sources

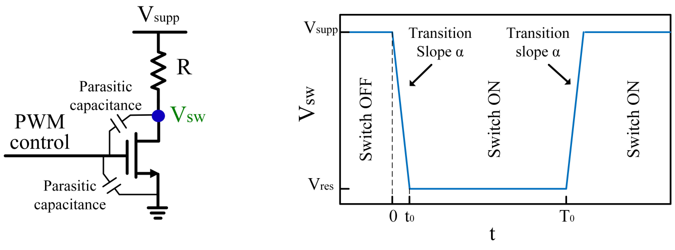

(a)

(b)

Figure 3.12: (a) Schematic of a simplified PWM driver with only one transistor switch (b) Simplified voltage drop on the switch versus time.

of loss in this circuit are the the power consumed by the switch due to its finite voltage drop, and the switching frequency dependent dynamic power wasted due to charging and discharging the capacitors. Since the capacitors are relatively small and the required switching frequency for the phase shifters of this design is relatively low, the dynamic power consumption is negligible compared to the phase shifter. To quantify the dynamic power consumption, dissipated power by a 1pF capacitor (much larger than the capacitances in the circuit) which is charged and discharged to 2.5 V (the maximum tolerable voltage by the transistors) with a 4 MHz switching frequency (used for this system) is considered. The wasted power by the charging and discharging of this capacitor is

$$P = fCV^2 = 4MHz \times 1pF \times (2.5V)^2 = 25\mu W, \tag{3.2}$$

which is much smaller than the average power delivered to a phase shifter ($\approx$ 10 mW).

The other main contributor to the PWM circuitry power consumption is the finite voltage drop on the switch during the on-state state as well as the voltage on the switch in transitions times. The simplified linear transition curves of Fig. 3.12(b) can be used to study the power consumption by the switch due to the finite voltage drop. In this first order model, the switching transitions are approximated as straight lines with slope of $\alpha = V_{supp}/t_0$. The average power consumption is achieved by integrating the power over a cycle and averaging as

$$\begin{aligned} P_{sw} &= \frac{1}{T}\int_0^T \frac{V_{sw}(V_{supp} - V_{sw})}{R} dt \approx \frac{V_{supp}^2 t_0}{6RT} + \frac{V_{supp}V_{res}}{R}, \\ P_{total} &\approx \frac{V_{supp}^2}{R}, \\ \eta &= \frac{P_{total} - P_{sw}}{P_{supp}} = 1 - \frac{t_0}{6T} - \frac{V_{res}}{V_{supp}}, \end{aligned} \tag{3.3}$$

in which P_{sw} is the power consumed by the switch, P_{total} is the total power delivered by the supply, and η is the power efficiency. The rest of the parameters used in equation (3.3) can be found in Fig. 3.12. Therefore, (3.3) concludes that fast transition times and small residual voltage drop on the switch can significantly reduce the power consumption of a PWM driver compared to a DAC. A DAC is always connected between the load it is driving and the supply voltage source. Therefore, The difference between V_{supp} and the load voltage will inevitably drop on the DAC, leading to the same average power consumption as the load which is much large than a PWM driver.

While the PWM scheme and row-column power delivery network increases the power efficiency of the system, the time sharing between N columns (here $N = 5$) increases the required peak driving voltage by a factor of $\sqrt{N}$. Moreover, a higher current handling capability is required for the driver since N phase shifters are being driven by a single driver port. Due to limitations on the area occupied by the electrical routing on the photonic chip as well as the electromigration considerations, yet even a higher drive voltage is desirable. Therefore, considering the maximum required power which corresponds to a 2π phase shift, the resistance of the phase shifter is adjusted to minimize the current and use the maximum available voltage. Moreover, the driver switching transition needs to be fast to enable precise phase control and avoid non-linear dependence of power on duty cycle induced by slow rise and fall times. These requirements, as well as the breakdown and reliability considerations in a CMOS technology, present an interesting design challenge for the driver design.

In this work, a peak drive voltage of 10 V with 8 bit pulse width resolution is considered for each optical phase shifter. However, 10 V is beyond the voltage breakdown tolerance of the standard transistors in high speed CMOS processes. Thus, a breakdown voltage multiplier [107] switching stack is designed to generate the PWM switching outputs while guaranteeing reliability and safe operation condition for the transistors. Moreover, to further protect the transistors from the unwanted overvoltage and reduce the switching transition time, a soft turn-on circuit is incorporated in the design as an interface between the digital PWM generator unit and the output switching stack. The functionality of the soft turn-on block is to initiate the switching in a controlled fashion.

Switching stack

The design of the high voltage switch which is capable of performing a fast PWM switching with a 10 V peak voltage is shown in Fig. 3.13. This switch stack utilizes a breakdown-voltage multiplier architecture which includes a stack of five thick-gate-oxide 2.5 V transistors, (M_1-M_5). To prevent over-voltage on the devices and guarantee reliability, the total voltage on the stack is distributed evenly among these transistors. Moreover, a positive feedback self-charging/discharging mechanism is devised which consists of M_6-M_8 and a resistive divider and is capable of performing fast switching with a small rise/fall time.

To illustrate the performance and design procedure of the switch stack, we consider the operation of the transistors as they go through a switching cycle. Before the switching happens, during the steady off-state, the digital PWM generator circuitry keeps the gate of M_1 shorted to ground and thus off-state resulting in zero current passing through the stack. The gate of M_2 is connected to a constant 2.5 V voltage source. Therefore, the drain node of M_1 is charged to this voltage as well which is the maximum possible voltage on this node and eliminates the possibility of voltage breakdown for M_1. Moreover, during the active operation, the drain node of M_1 will never get fully charged to 2.5 V due to the finite time constants of the circuit and thus breakdown safety for the transistor is guaranteed. For the rest of the stack transistors, M_2-M_5, a voltage distribution along the stack is provided by the resistive bias network such that there is an extra breakdown safety margin for each transistor to avoid overvoltage situation during the off-state.

The switching transition from the off-state to the on-state is initiated by increasing the gate voltage of M_1 leading to this transistor sinking current through the stack. It should be noted that, due to the time varying voltages over the transistors, exceeding the breakdown voltage during the transition states either because of systematic design problems or fabrication induced non-idealities, is more likely. In this transition phase, the PMOS transistors $M_6 - M_8$ form positive feedback loops with $M_3 - M_5$, respectively, and discharge their gate charges as the output voltage drops. As a result of the transition, all the gate voltages are eventually reach 2.5 V and their drain-source voltages to a small voltage close to zero which forms the on-state for the stack with all the transistors conducting current.

To further study the details of the switching mechanism, a single block of the stack as shown in Fig. 3.14 is considered. In this unit block, M_n is the switching transistor, M_p forms the positive feedback for the discharge phase, and C_b and C_g include

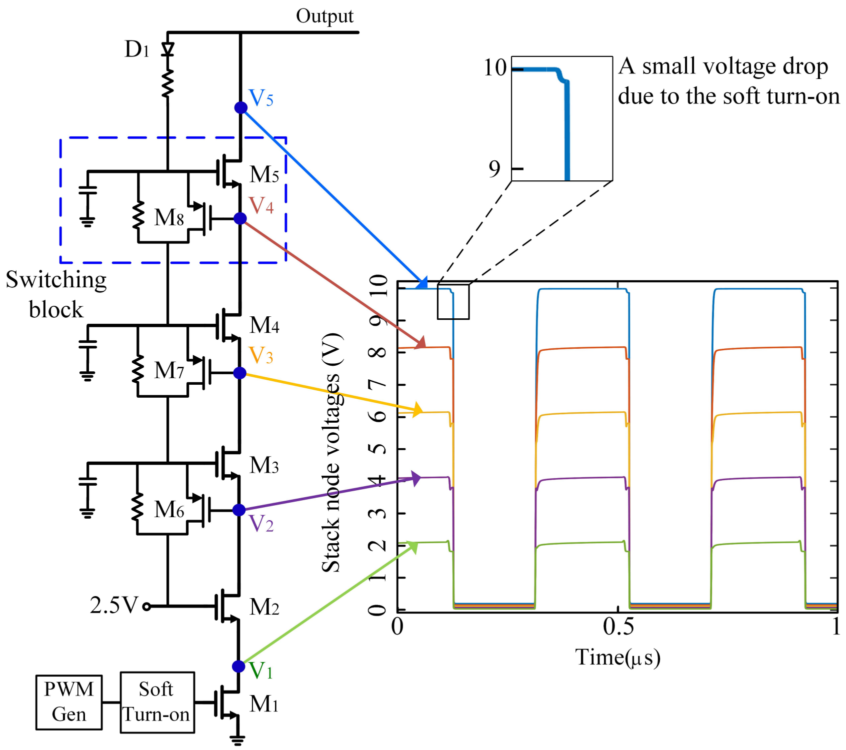

Figure 3.13: Stack of 5 transistors to form a high swing switch. $(W/L)_{1-5} = 64\mu m/0.28\mu m$, $(W/L)_{6-8} = 4\mu m/0.28\mu m$, $C_1 = 364fF$, $C_2 = 164fF$, $C_3 = 110fF$.

the total parasitic capacitance between the nodes they are connected to. During the off-state, the source and gate voltages of M_n and M_p are equal, which turns both of them off with zero current flowing through the stack. When the transition starts, increasing I_1 discharges C_b and reduces the source voltage of M_n. Due to the relative small parasitic capacitances of the transistors, in the absence of the external capacitor C, the time constant of the gate node is very small. Therefore, the gate voltage of M_n will also drop while the transistor is still off and its drain voltage is at the previous value. Therefore, dropping source voltage results in momentary drain-source and drain-gate overvoltage. To avoid this scenario, the external capacitor C is added as shown in Fig. 3.14(a), which increases the time constant of the gate node and provides the charge for C_g as the source voltage of M_1 drops. Charging C_g while keeping the gate voltage of M_n temporarily constant results in a gate-source voltage increase that eventually activates the transistor. The transition time that it takes for I_1 to charge C_g by V_{th} (the threshold voltage) and put the NMOS transistor of the i'th block in the stack at the verge of the on-state can be calculated by estimating the

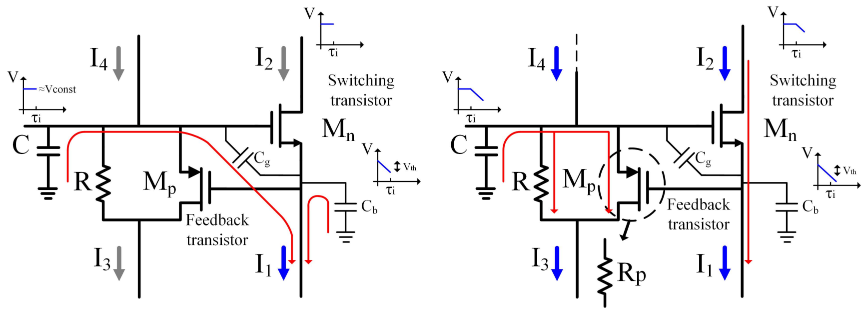

(a) (b)

Figure 3.14: A single block of the stack (a) before activation (b) after activation.

average of I_1, namely I_{ave}, as

$$\tau_i = (C_n + C_p)\frac{V_{th}}{I_{ave}} = C_u L^2 V_{th}(1+\alpha)\frac{1}{I_0}, \tag{3.4}$$

where

$$C_n + C_p = C_u WL(1+\alpha), \quad I_{ave} = \frac{W}{L} I_0. \tag{3.5}$$

C_n and C_p are the total parasitic capacitances of M_n and M_p, respectively, which are connected to the source node of M_n. $\alpha = C_p/C_n$ is defined to capture the relative strength of the two transistors in the unit and is related to the size ratio of M_p and M_n, and $C_u = C_n/(WL)$ is the normalized capacitance and a technology dependent constant. W and L are the width and length of M_n, respectively, and $I_0 = I_{ave}/(W/L)$ is the normalized average current with respect to the transistor sizing.

As the transition phase continues, eventually V_{gs} exceeds V_{th} and both M_n and M_p turn on[2]. Therefore, M_n starts sinking current and lowering its drain voltage, starting the transition process for the next (upper) block of the stack and M_p participates in finishing the transition phase with a stronger current it provides. Therefore, the total switching fall time is

$$\tau_{tot} = \sum_{i=1}^{N=5} \tau_i, \tag{3.6}$$

where τ_1 and τ_2 are the time delays caused by M_1 and M_2, respectively, and can be calculated easily by considering their parasitic capacitances.

While the analysis guarantees safety upto the point that V_{gs} exceeds V_{th}, further analysis is needed for the time after the stack block of Fig. 3.14 is turned on. As

---

[2] For simplicity of the analysis, it is assumed here that the two transistors have the same threshold voltage. However, extending the derivation for different threshold voltages is straightforward.

mentioned, after M_n and M_p are active, M_n starts sinking current and initiating the activation process for the next block. At this phase, M_p can be modeled by an average resistance R_p performing in parallel with R, as shown in Fig. 3.14(b), leading to a gate voltage of M_n with a time constant τ_p. For the gate voltage of M_3, the time constant is $\tau_p = (R||R_p)C$, resulting in[3]

$$V_{g,M3} = (V_{g0} - 2.5V)e^{-t/\tau_p} + 2.5V. \tag{3.7}$$

Equation (3.4) suggests that a smaller size for M_p reduces the delay time τ by lowering α. However, the sizing of M_p and the value of C should consider two extreme cases that lead to overvoltage. On one hand, the capacitor C should be large enough to hold the gate voltage of M_n long enough initially such that it enters the strong on-state. Otherwise, a similar scenario to what discussed above will happen due to the current passing through C_g and discharging C which results in drain-source overvoltage if the gate and source voltages of M_n drop while the drain voltage is still high. On the other hand, an overly large capacitance for C leads to a large time constant τ_p, delays the gate voltage drop while the source node of M_n is discharging, and results in gate-source overvoltage. This situation can be avoided by increasing the size of M_p that reduces τ_p at the expense of a larger α. Therefore, the value of capacitance for C should be adjusted to be the smallest value that strongly turns on M_n and initiates the upper stage with the largest I_0. The sizing of M_p is accordingly adjusted to be the smallest value considering the value of C. The expression describing the gate voltages of M_4 and M_5 is more complicated due to the time varying nature of the drain voltages of M_7 and M_8. These equations collectively yield the required sizing for for each stage to maximize I_0 and minimize τ_{tot}.

Once the transition phase is over and the stack is fully switched, it provides a current path for the output node to ground with a finite voltage drop across the switch. The output on-voltage of the stack is a function of the current passing through the switch and on the size of the transistors. Since the functionality of the switch in a safe condition depends on I_0 to the first order, which is calculated for a normalized size of the transistors, if a larger total current in the on phase is targeted or a lower

---

[3] Once the upper blocks enter the transition phase, an extra current factor is sourced to the gate node through I_4 (Fig. 3.14), which can be modeled by an increase of the time constant τ_p. Moreover, the time constant of the gate node includes other factors that are in the current flow path to the 2.5 V voltage source. The circuit analysis to derive the more exact time constant is straightforward and will not be discussed here.

on-voltage drop is desired, the size of the structure can be scaled[4] accordingly. In this project, the residual on-voltage is adjusted to be less than 203 mV for an output current of 10.3 mA, which is small enough to achieve a low power consumption in the switch and a high driver efficiency. For the stack to properly function in the on-state, the diode D_1 (Fig. 3.13) is included to prevent the flow of a reverse current through the resistors due to the smaller drain voltage of M_5 compared to its gate voltage.

The last phase of the switching cycle is the transition back from the on-state into the off-state. This process which is initiated by the control circuitry turning M_1 off, is followed by charging M_1's drain node via the current M_2 provides. This increased voltage on the drain node of M_1 leads to a smaller gate-source voltage for M_2 that corresponds to a reduced sinking strength for transferring the current delivered by M_3, which eventually results in a voltage rise on the drain of M_2. This the mechanism of turning off which happens sequentially for all the transistors in the stack, and restores the mid-point voltages in the circuit to their off-state values. The critical part of transition to off-state is that the gate voltages of $M_3 - M_5$ should increase to their final values with the same trend of the increase in the drain voltages to prevents overvoltage on the drain-gates. This can be achieved by adjusting the absolute value of the resistors in the divider chain. Therefore, while the gate voltages in the off-state depend only on the relative values of the biasing resistors, their absolute values are adjusted according to the required time-constant during the rise time.

Soft turn-on

Equation (3.4) shows that reaching the threshold voltage, $V_{th} = 0.475\,\text{V}$, of the transistors is the main component causing delay in the stack transistors sequentially turning on. Moreover, the delay between individual units increases the drain-source voltage and necessitates extra voltage margin to prevent the occurrence of overvoltage. To address this issue and provide a faster switching transition, here, a soft turn-on block is designed which also increases the immunity of the stack to experiencing voltages exceeding the transistor breakdown voltage rating. The soft turn-on block achieves this by partially turning the switches on before applying the full switching signal such that a small current of 160 µA starts flowing through the stack which puts all transistors at the verge of turn-on. Then, the full switching

---

[4] Second order effects in sizing can be included by investigating the simulation result for the node voltages.

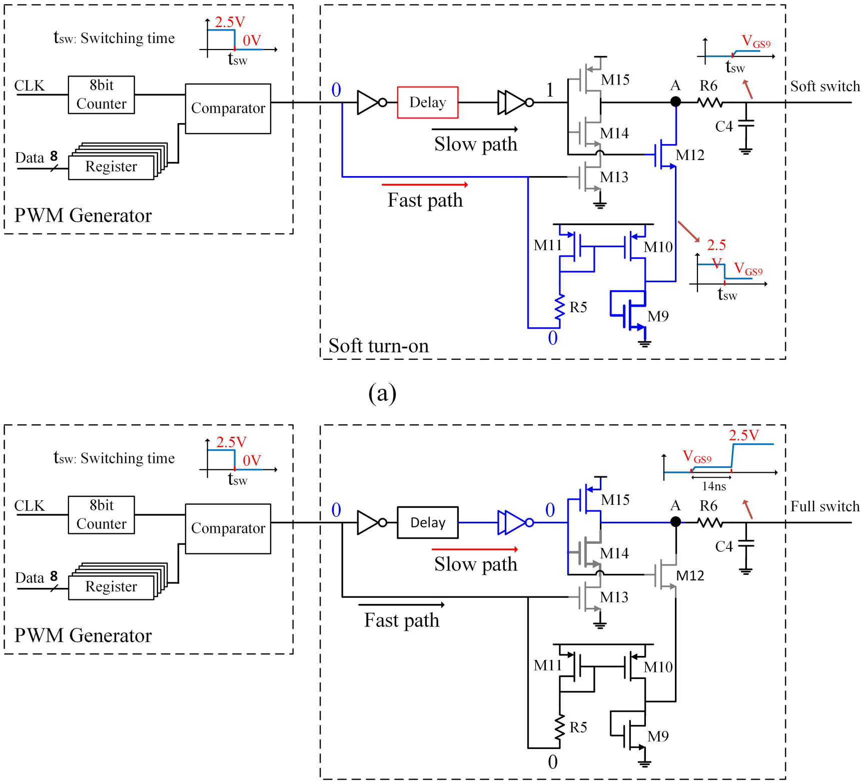

(a)

(b)

Figure 3.15: (a) Initial activation of the stack transistors through the fast path which raises the output trigger voltage by V_{th}. (b) Full switching of the stack through the main path delivering a strong switching command after 14 ns of delay.

occurs by applying the strong switching signal and results in all the transistors transitioning to strong conduction mode.

To achieve this, a delay cell is embedded in the soft turn-on block as shown in Fig. 3.15 that postpones the propagation of the digital switching signal while sending it through a fast path. The signal of the faster path increases the gate voltage of M_1 to V_{GS9} (M_9 is a relatively large transistor such that its gate-source voltage its close to the threshold voltage). This happens after the switching signal turns M_{13} off which disconnects the path from node “A” to ground through M_{14} resulting in V_{GS9} being transferred to this node via M_{12}. The resistor R_6 and capacitor C_4 form a lowpass filter to damp the switching spikes on node “A”. Therefore, M_1, and subsequently all the switching transistors in the stack, transition to the verge of turn-on. After almost 14 ns, the strong switching signal passes through the delay block and M_{15} connects node “A” to VDD for full switching. The initial turn-on voltage is disconnected in this phase by M_{12} (Figure 3.16). This 14 ns provides enough time for the stack soft

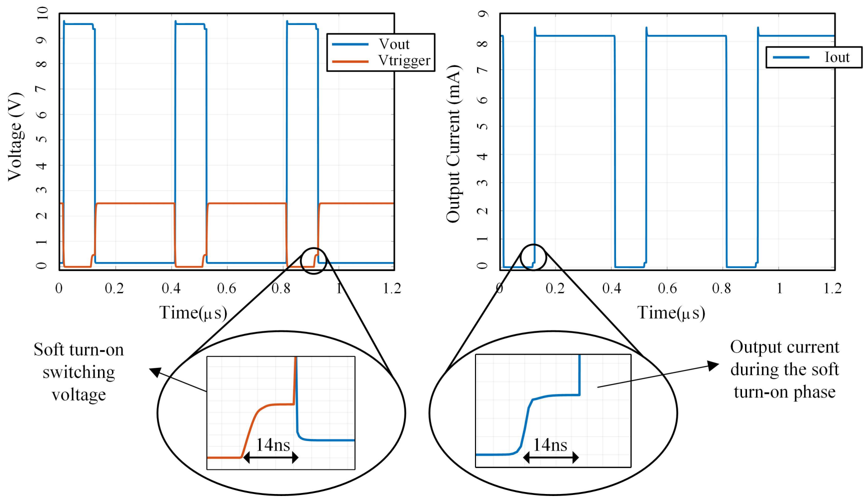

Figure 3.16: Simulation result for the generated PWM signals with soft turn-on switching. The soft turn-on circuit delays the strong switching signal for 14 ns and pre-activates the stack.

turn-on in addition to a 6 ns safety margin.

3.6 System design

Figure 3.17 shows the block diagram of the photonic chip accompanied by the CMOS electronic driver chip forming the two-chip sparse OPA system. A focusing grating coupler is used as the optical input port for coupling the laser light at 1.550 nm, which is delivered to the system by an optical fiber, into an on-chip dielectric waveguide. The focusing grating coupler introduces 6 dB of insertion loss. The system includes two power splitter structures. The input power splitter network is a 1-to-16 divider that is fed by the input port and generates 16 equal amplitude outputs through four layers of binary tree power divider. Each output is then delivered to a folded row. Each folded row unit includes a 1-to-8 power splitter (3-layer binary tree) as shown in Fig. 3.18(d). This secondary splitter structure further divides the optical power which are then routed to the eight optically active phase shifters in the row. Therefore, the power splitter networks in series generate 128 equal-power branches. Figure 3.18(a) shows the design of each individual power splitter which is a symmetric Y-Splitter [108] and thus provides an even amplitude distribution at output branches. Other advantages of these splitters are the small input reflection of −28 dB and a compact footprint which is leads to robustness to fabrication mismatches and chip temperature variations. The phase of the 128 branches are adjusted in the phase shifter network. The phase shifter network is

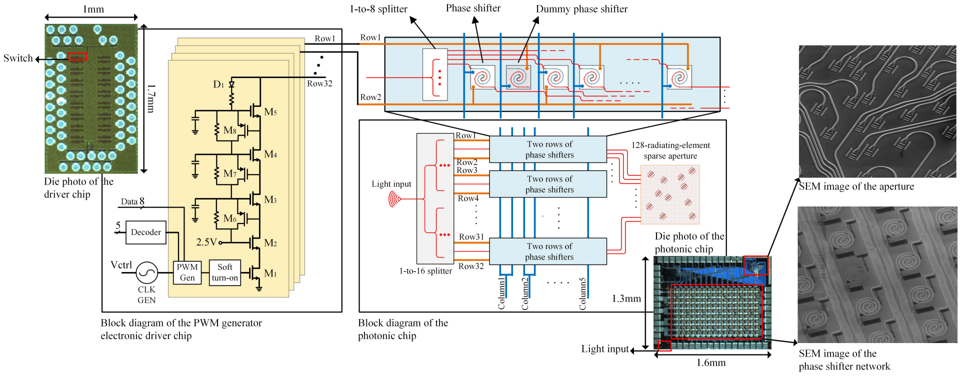

Figure 3.17: Schematic diagram of the OPA chip-set and the die photos of the fabricated chips.

electrically interfaced with the electronic chip, and through full 2π phase control capability any arbitrary wavefront can be generated. The processed optical signals are then routed to the radiating aperture with minimum optical path length mismatch between the 128 branches and fed to the nano-photonic antennas.

The high heat conductivity of the silicon substrate leads to a relatively uniform heat distribution in the bulk. If the temperature of the chip varies, due to this uniformity the temperature of all the optical waveguides on the chip changes together. Therefore, ideally, for a path lengths matched design far-field pattern will not get affected by the temperature variations. However, inevitable fabrication mismatches induce path length mismatch between different optical signals which leads to a different phase shift variation for each path. A more severe case happens if a temperature gradient is formed on the chip which results in different waveguides being exposed to different temperatures. It should be noted that once the phases are adjusted to form a beam, the angular position of the beam does not alter with temperature variation. However, side lobe level starts increasing and eventually for very large temperature gradient or temperature change, it gets buried in the side lobes. The temperature gradient is mainly cause by different phase shifters consuming different power levels in operation. Therefore, three resistive heaters are placed at the corners of the photonic chip to balance any potential large thermal gradient over the chip. Moreover, uniformly placed dummy phase shifters are embedded in the phase shifter network and are powered actively to cancel the local thermal gradients. To form a feedback loop for controlling the on-chip heaters, three point to absolute temperature (PTAT) sensors are placed on the photonic chip away from the phase shifter network. Each of these sensors is a set of 5-to-1 ratio junction diodes and measure the substrate

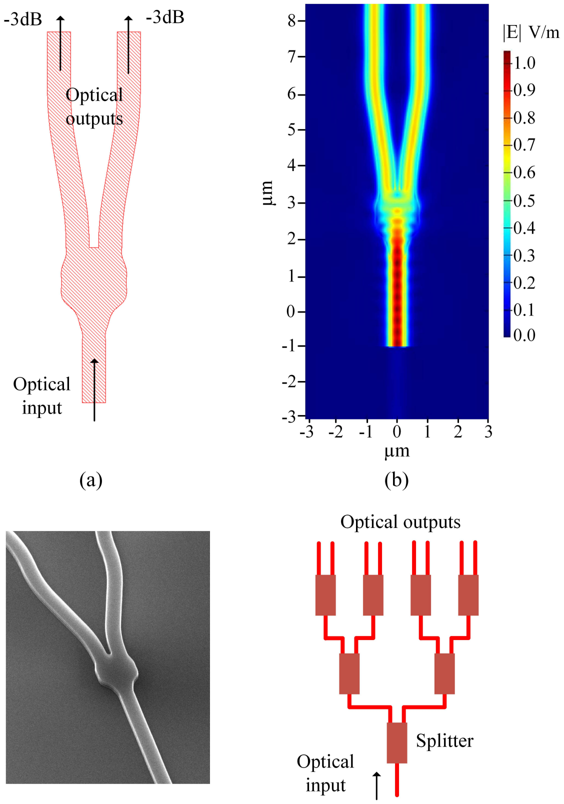

(a) (b)

(c) (d)

Figure 3.18: (a) A single 3 dB splitter with a small footprint of the splitting region (b) EM simulation of the 3 dB splitter showing a uniform power distribution and negligible input port mismatch (c) SEM image of the fabricated splitter (d) The 1-to-8 binary tree splitter network.

temperature underneath itself. The current sources required for driving the sensor diodes as well as the voltage readout circuitry are external to the photonic chip.

The electrical interface to the rows and columns of the phase shifter network is provided via bonding pads connecting the photonic chip to the electronic chip. There are 32 individually controlled PWM drivers on the electronic chip which are delivering power to the rows of the phase shifter network. As explained in section 3.5, each PWM driver includes a stack switch, a soft turn-on block, and a digital PWM generator. The width of the driving pulse is digitally programmable for each driver through the on-chip digital controller. This forms a convenient control interface for the system. The PWM driver cycles over all the columns with a cycling rate of 4 MHz. This is high enough for the power delivered by the PWM signals to be filtered and averaged by the low-pass response of the phase shifters and avoid phase shift ripples. The electrical columns of the phase shifter network are controlled synchronously with the PWM generation phases by a multiplexer that through switching the columns between 0 and 10 V selects which column should be powered for each phase.

Figure 3.17 shows the die photo of the two fabricated chips. The photonic chip is fabricated on a standard silicon photonics platform with a 2 µm BOX thickness and a 220 nm silicon device layer for designing photonic components. Moreover, two etch levels of 90 nm and 150 nm into the silicon layer, multiple n-type and p-type doping layers, and two metal layers are available in the process for designing various electro-optical systems. The electronic chip is fabricated in a standard 65 nm CMOS process that offers thick oxide transistors with a 2.5 V breakdown voltage rating which are used in designing the switching stack transistors.

3.7 Measurement setup and results

The optical insertion loss of the on chip waveguides are measured 2.5 dB/cm. This leads to a small loss for milliliter scale waveguide lengths on the chip and does not considerably affect the performance of the system. The overall insertion loss of the 7-layer power splitter is 2.8 dB with each individual power splitter contributing 0.4 dB, and the output of the 128 branches after split is uniformly distributed within less than 1 dB variation. Moreover, the splitters are robust to fabrication mismatches and thermal variation due to their compact size and geometrical symmetry. Scaling the array and embedding a larger number of elements requires more layers of the splitter tree with the inevitably added insertion loss. However, since adding each layer doubles the number of output branches, the logarithmic growth of the optical loss versus the number of elements yields a small impact on the system performance as it scales.

To characterize the performance of the spiral phase shifters a Mach-Zehnder modulator is formed on the same chip using a spiral phase shifter (identical to the ones used in the phase shifter network) as a test structure. The input light to the modulator is split into two branches as shown in Figure 3.19(a) with one of the modulator arms having a spiral phase shifter on the light path and then recombining the two arms at the output. Driving the modulator with different power levels causes the corresponding phase shift being induced in the phase shifter leading to different power levels at the output waveguide, accordingly. This amplitude response of the modulator which is a function of the phase shift and thus the applied drive signal is shown in Fig. 3.19(b) versus the input drive voltage and the calculated corre-

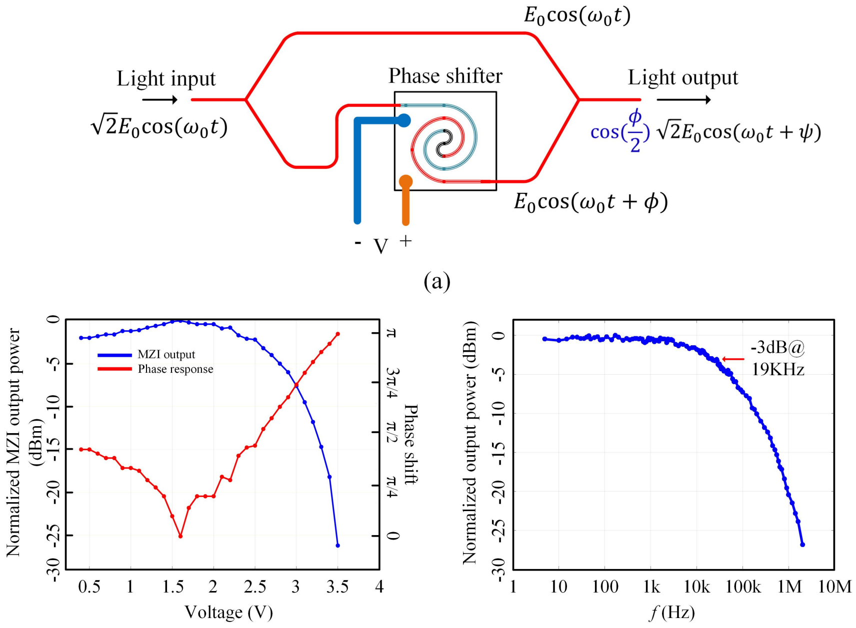

(a)

(b)

(c)

Figure 3.19: (a) Mach-Zehnder modulator for characterizing the phase shifter (b) Output power of the Mach-Zehnder modulator versus the applied voltage to the phase shifter and its corresponding phase shift. (c) Frequency response of the phase shifter.

sponding phase shift for the phase shifter. The constructive interference between the output of the two arms are not expected to happen at zero phase shift here since the two optical paths are not length matched. Therefore, the first occurrence of the constructive interference leading to a peak of the output amplitude happens at an offset voltage. The measurement result of the Mach-Zehnder modulator shows a π phase shift for a drive power of 10.6 mW. Moreover, the measured frequency response of the phase shifter using the modulator test structure (Fig. 3.19(c)) shows a 3 dB bandwidth of 19 kHz. This response is fast enough for applications such as wireless optical communication to allow a feedback mechanism to easily follow any mechanical movements and drift in real time.

The cycling rate of the PWM driver is designed to be adjustable in the range of 0.7 MHz to 14 MHz. This cycling rate is high enough compared to the phase sifter frequency response for the driving ripples to get suppressed by the low-pass filtering nature of the phase shifter. Two exemplary measured PWM signals which are generated by the CMOS chip to drive two of the rows with two different duty cycles are shown in Fig. 3.20 The fall time is 12 ns which is imposed by the speed of the switch action. On the other hand, the rise time of 71 ns is dominated

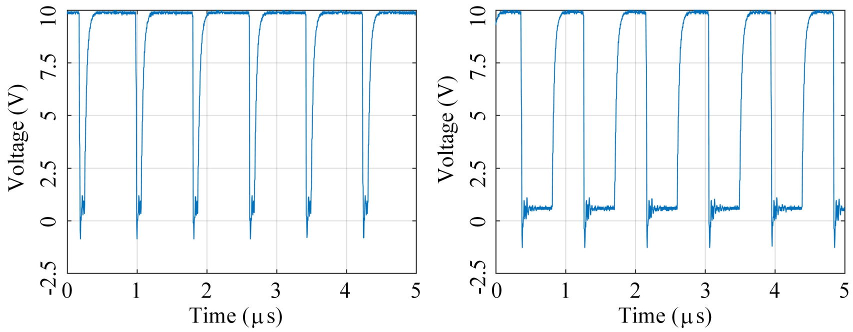

Figure 3.20: Exemplary PWM signals generated for driving two of the rows with two different duty cycles.

by the parasitic components at the output node of the interface. The on-voltage of the PWM drivers (for the whole switching stack) is 480 mV which leads to a significantly lower power consumption by the electronic circuitry compared to conventional DAC-driven OPAs, as discussed previously. For a π phase shift, the power consumption of each PWM driver, which is connected to a single row of the phase shifter network, is 1.3 mW. The main factor in driver power consumption is the output switch stage and the power consumed by soft turn-on block, which is less than 10 µW, is not a considerable.

Fig. 3.21(a) shows the schematic of the system characterization setup for the full OPA system in which the two chips are mounted and connected electrically on a printed circuit board (PCB). The PCB also includes the regularized supply lines for the chips, a readout circuitry for the PTAT sensors, and a micro-controller to digital interface the drivers and a desktop computer. The input light source for the system is a laser source of wavelength 1.550 nm with 2 dBm output power which is transferred by an optical fiber and coupled to the photonic chip through the input focusing grating coupler. The camera which is placed 30 cm away from the aperture with its lens removed captures the far-field pattern of the radiation via the photonic chip aperture. The far-field region for the antenna array starts approximately at 3 cm away from the aperture and thus the camera is well positioned in the far-field region. Light emitted by the OPA aperture propagates towards the camera aperture and impinges on the photo-detectors. In the absence of the camera lens, it directly records the radiation pattern. The output of the camera as well as the PTAT sensors are then collected by the desktop computer. The computer also sends commands to the micro-controller which is responsible for programming the electronic chip accordingly, controlling the pulse-widths, and eventually adjusting the phase shifts.

Table 3.1: Comparison Table

	This work	Caltech (2015) [46]	USC (2015) [83]	USC (2018) [62]	MIT (2017) [61]	Intel (2016) [85]	MIT (2016) [86]
Aperture	2D	2D	2D	1D	1D	1D	1D
Number of radiating elements	128	16	64	1024	1024	128	50
Minimum element spacing	5.6 μm	50 μm	33 μm	2 μm	4 μm	5.4 μm	2 μm
Maximum steering angle	16°	1.8°	1.6°	45°	23°	80°	46°× 36°
Beamwidth	0.8°	0.5°	0.45°	0.03°	0.021°	0.14°	0.85°× 0.1°
Side-lobe suppression (dB)	12*	6	11	9	10	8.9	8
Power consumption mW**	10.6 mW	N.R.	19.2 mW	54 mW	N.R.	80 mW[XX]	17.4 mW
Integrated electronics/photonics	Yes/Yes	No/Yes	Yes/Yes	Yes/Yes	No/Yes	No/Yes	No/Yes

* Side lobe level is reported for the broad-side beam
** Per element at π phase shift

Therefore, the desktop computer is the processing center of a feedback loop that process the data and adjust the phase shifters. The OPA is calibrated through an optimization process to form an optical beam using the real-time gray-scale output image of the camera. Through this process, the optimization algorithm changes the power delivered to the each phase shifter to adjust its phase shift and the changed far-field pattern which is capture by the camera is fed back to the optimizer for the next optimization step. The optimization is a gradient ascend algorithm that maximizes the power directed to the pixels of a certain region on the camera aperture which converges to forming an optical beam.

Figure 3.21(b) shows the image formed on the aperture of the camera after forming the optical beam by adjusting the phase shifters. The lens of the camera is removed and thus the image corresponds to the projected far-field pattern. The high intensity

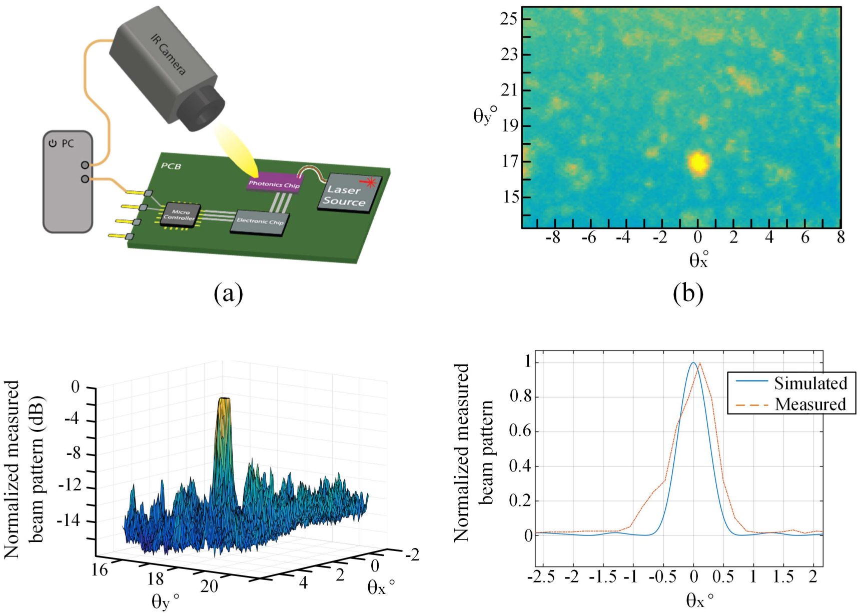

(a) (b)

(c) (d)

Figure 3.21: (a) Measurement setup (b) Radiation pattern of the formed beam (the yellow spot) captured by the camera (c) Captured pattern by the camera (d) Simulated and measured results of the beam pattern for $\phi = 0$ (e) Simulated and measured results of the beam pattern for $\phi = \pi/2$.

region in the image (the yellow spot) is the location of the formed optical beam. The output data of the camera is plotted in 3D in Fig. 3.21(c), which shows the largest side lobe level of -12 dB for the broadside beam. In this figure, θ_x and θ_y are elevation angles for azimuth angles of $\phi = 0$ and $\phi = \pi/2$, respectively. To measure the radiation pattern of the OPA a single photo-detector rotates along the θ_x axis while recording the light intensity. The measured and simulated patterns are shown in Figure 3.21(d) and Fig. 3.21(e) with the measured result achieving a beamwidth of 0.8° and a steering range of 16° in both steering angles. This is the largest number of resolvable spots (steering range over beamwidth ratio) among all reported 2D optical phased arrays.

Figure 3.22 demonstrates the beam steering capability of the sparse OPA. Through purely controlling the phase of the radiating elements, the optical beam is steered to several angles over the 2D field-of-view as shown in Figure 3.22(a). The OPA system has the capability of performing as a lens-less projector by steering the beam towards different angles through sequentially adjusting the phase shifts. To further elaborate this capability, letter “A” is projected on the camera aperture illustrated in Fig. 3.22(b).

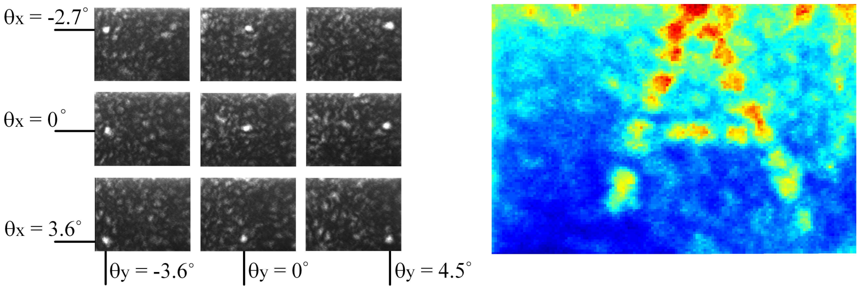

(a) (b)

Figure 3.22: (a) Illustration of the beam steering capability by forming a beam at multiple angles (b) The letter “A” projected by beam steering.

Table 3.1 presents a summary of the implemented sparse OPA transmitter chip-set with a PWM drive along with a comparison against state-of-the-art OPAs in the literature. As listed in Table 3.1, previously reported OPAs with 2D apertures are limited to a small steering range which is due to the large size of the nano-photonic antennas used in these works as well as the area required inside the aperture for optical feed distribution. The narrow beamwidth reported by these works is a consequence of large element spacing. However, the total number of resolved spots, which is defined by the steering range over beamwidth, illustrates the performance limitations in the previously reported OPAs with a 2D aperture. While the 1D aperture OPAs achieve a higher resolution, their electronic beam steering capability using the adjustable phase shifters is restricted to only one dimension.

Table 3.1 also demonstrates the power consumption of OPA systems. Assuming an average π phase shift for each phase shifter, the measured mean power consumption of this design is 10.6 mW per radiating element for a given beamforming configuration. This is only the comparison of the power consumed by the phase shifters while there are two other main factors which contribute in reducing the power consumption of the system: the power saving due to the PWM drive and the reduction compared to an equivalent uniform array. In other words, when the full OPA system is considered, the power efficiency of the PWM driver contributes a large factor in the low-power design of the system. Moreover, since the beamwidth of the presented OPA is equivalent to a uniform OPA with 484 elements, 484 phase shifters are needed if it is achieved via a uniform OPA, leading to a higher overall power consumption .

3.8 Conclusion

In this work, a nonuniform sparse 2D OPA transmitter with adaptive beamforming and beam steering capabilities is demonstrated. The sparse aperture structure facilitates the feasibility of optical feed distribution in a low-cost single layer photonic process as well as potential radiation pattern adjustment that paves the way for a large scale 2D OPA. The demonstrated 128-element OPA with a beamwidth of 0.8° and a 16° grating lobe-free steering range achieves the largest reported number of resolvable spots among the state-of-the-art single wavelength OPAs. Moreover, a PWM driven row-column power delivery network is implemented for adjusting the optical phase shifters that significantly reduces the complexity of the electronics circuitry and increases its power efficiency. To drive the phase shifter network, a high-swing PWM driver with a soft turn-on activation is designed. This two-chip solution OPA is fabricated in a 65 nm CMOS process and an SOI silicon photonics foundry.

Chapter 4

OPTICAL PHASED ARRAY RECEIVER

In this chapter, an integrated photonic receiver system is demonstrated with the capability of on-chip adaptive manipulation and processing of an incident wavefront on its aperture. First, an analytical framework is established to study the wavefront sampling through an array of receiving antennas and methods for reconstructing the captured wavefront is discussed. The building blocks of the receiver including an antenna array and an optoelectronic mixer network are explained. The mixer down-converts the received optical samples to radio frequencies while maintaining their phase and amplitude information. It also provides a relatively large conversion gain that leads to a high reception sensitivity as well as robustness to noise and interference. The rest of the chapter is followed by presenting two OPA receivers with one-dimensional and two-dimensional apertures which are the first high sensitivity OPA receivers demonstrated in the literature. Finally, measurement results are discussed and the capability of the OPA receivers to function as a lens-less camera is demonstrated[1].

4.1 Introduction

In many optical systems, precise engineering and manipulation of an optical wavefront is required and plays as an essential function of the systems to achieve the desirable performance [109]–[112]. Conventionally, discrete optical components such as various types of lenses were used to performed this task which usually lead to a bulky form factor for the system. However, the capability of active wavefront manipulation on an integrated platform significantly reduces the size of many conventional optical systems and leads to reduced cost, scalability, and better manufacturability [113]–[116]. In addition, such an active flat optics solution will further open the possibility for devising many novel applications and functionalities that were not feasible conventionally [117]–[121].

To sample an incident optical wavefront an array of receiving antennas can be used forming the aperture of the integrated system. If the processing of these samples is linear, the system can be considered a general form of a phased array

---

[1] The work presented in this chapter was done in collaboration with Behrooz Abiri and Aroutin Khachaturian.

receiver in optical domain or an OPA receiver which is the counterpart to the OPA transmitter (discussed in details in the previous chapters) with reciprocal functionalities. Therefore, it can potentially form and steer a reception beam via electronically controlling the phase shift and amplitudes of the received samples and collect light selectively from any desired direction. An OPA receiver also has the capability of suppressing undesirable light impinging on the aperture from other directions, multipath reflections, or even active jammers. This angular or spatial reception selectivity is highly valuable in many applications, such as LiDAR and point-to-point communication systems. In a LiDAR system, directive reception can be used to collect light only from the spot that is being illuminated while rejecting all the unwanted spuriously illuminated points and multipath reflections. This can significantly enhance the detection sensitivity and directly translates to range, resolution, and accuracy of the system. An OPA receiver can also be beneficial in optical wireless communication systems with multiple active links in the same room (space) via minimizing the unwanted interference between channels and increase the fidelity of the communication link utilizing its selective directivity.

Furthermore, an active flat optics OPA receiver has the potential capability of enabling other applications which might not be feasible or practical with conventional optics, such as emulating the functionality of a lens on a flat active silicon chip with negligible thickness and performing lens-less imaging. This feature allows for elimination of the lenses which are usually bulky and require sizable physical depth to perform imaging. The OPA receiver integrates the functionality of the all lens in the system on a very thin and flat active area [24], [25].

Previously, an OPA transmitter was suggested to be utilized in a receiver setting based on the reciprocity of electromagnetic wave propagation [83]. However, such a simple architecture does not provide the required reception sensitivity for a practical system due to the fundamentally different design trade-offs in designing transmitters and receivers. Since received signal at the receiver input is typically very weak, such a direct power detection receiver architecture suffers from out-of-band signals, stray light, noise, and other sources of interference.

Here, an integrated photonics architecture is developed that captures the incident wavefront by sampling it through an array of antennas and is capable of arbitrarily manipulating the optical wavefront on-chip. To detect weak received signals with high accuracy and achieve a high sensitivity, an optoelectronic mixer is devised which down-converts the received samples while providing conversion gain and adjustable phase shift. The rest of the chapter discusses the analytical framework, design, measurements, and the demonstration of the implemented OPA receiver as a lens-less camera.

4.2 The theory of operation

In this section, the theory of the waveform reconstruction using an OPA receiver is discussed and design of the 1-by-32 and 8-by-8 OPA receivers are explained, accordingly. Figure 4.1(a) shows the general setting of the receiver system with antenna elements arranged in a 2D array and impinging wave-front captured by the receiver antennas. According to the sampling theory, using only the samples of the measured waveform at a finite number of points is enough to reconstruct the full incident electromagnetic wave-front, where the reconstruction accuracy is determined by the number of spatial samples, the element spacing, and the signal-to-noise ratio of the received signals.

The aperture of the photonic receiver consists of a set of photonic receiving elements (nano-photonic antennas) that, in its simplest form, distributed on a planar surface. The receiving elements capture the incident light (optical electromagnetic wave) and couple it to an on-chip waveguide. The schematic of the receiving elements with 1D and 2D FOV are shown in Fig. 4.2(a) as well as the waveguide that they couple the captured light into it. In an aperture with uniform element placement, the elements are located at

$$(x_n, y_m) = (nd, md), \quad 0 \le n < N, \qquad 0 \le m < M, \tag{4.1}$$

where n, m, N, and M are integer numbers and d is the element spacing. While uniform arrays are mathematically more tractable, it should be noted that non-uniform element spacing, forming an aperiodic or a sparse array, can be used to increase the grating-lobe-free steering range. Such apertures has been used for OPA transmitters [21], [85].

Considering an impinging electric field at an angle (θ, ϕ) with a complex amplitude of $E_i(\theta, \phi)$, the coupled electric field by the element at $(0, 0)$ to its waveguide is

$$E(0,0) = \int_0^{2\pi} \int_0^{\pi} G(\theta, \phi) E_i(\theta, \phi) d\theta d\phi. \tag{4.2}$$

In this equation, $G(\theta, \phi)$ is the reception pattern of each single receiving element and quantifies the collection strength for a matched polarized plane wave with a

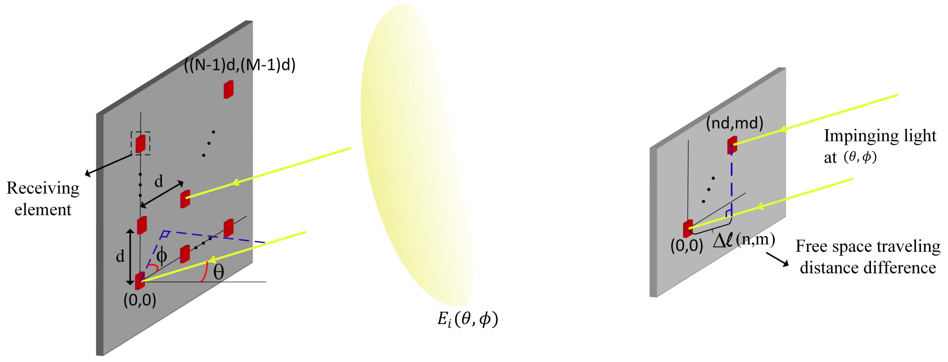

(a) (b)

Figure 4.1: (a) The general setting of the receiver operation (b) Free space traveling distance difference between elements for a plane wave impinging at an angle (θ, ϕ).

Poynting vector impinging at the direction of (θ, ϕ)[2]. For an element at (nd, md) (not at the origin), the plane wave incident at (θ, ϕ) travels a different distance in free-space before reaching the antenna as shown in Fig. 4.1(b). This path difference is

$$\Delta l(n, m) = nd \sin\theta \cos\phi + md \sin\theta \sin\phi, \tag{4.3}$$

which for a coherent light of wavelength λ translates to a phase shift of $(2\pi/\lambda)\,\Delta l(n, m)$. Therefore, the coupled electric field into the receiving element at at (nd, md) is

$$E(n, m) = \int_0^{2\pi} \int_0^{\pi} G(\theta, \phi) E_i(\theta, \phi) \exp^{-i\frac{2\pi}{\lambda}\Delta l(n,m)} \, d\theta d\phi. \tag{4.4}$$

The output of the aperture is a set of waveguides carrying the captured electromagnetic wave incident on each antenna, $\{E(n, m)\}$. These signals differ in angle dependent phase shifts and form a sample set of measurement of the incident wave-front. This set of measurements can be used to reconstruct/estimate the incident wave-front, $E_i(\theta, \phi)$, at every angle (θ, ϕ). The accuracy of the wave-front reconstruction is a function of the number of receiving elements and their location. If the sampling result for the whole incident plane is available, an exact reconstruction of $E_i(\theta, \phi)$ would be possible. However, sampling an infinite plane requires an infinite number of elements in both x and y directions which is not feasible in real implementations. Therefore, only a finite aperture size can be sampled which results in reconstruction non-idealities analogous to the diffraction limit in conventional optical systems.

---

[2] If the polarization of the incoming wave deviates from the matched polarization by ψ on the Poincare sphere, a matching factor of $\cos(\psi/2)$ is added to $G(\theta, \phi)$.

A powerful method to reconstruct $E_i(\theta, \phi)$ is forming a linear combination or a weighted sum of the samples $E(n, m)$. The weighting coefficients are complex values $b_{(n,m)}(\theta_0, \phi_0)$ which are functions of the angle (θ_0, ϕ_0) for which E_i is reconstructed. Each complex coefficients can be implemented by applying a phase shifts of $\angle b_{(n,m)}(\theta_0, \phi_0)$ and an amplitude gains of $|b_{(n,m)}(\theta_0, \phi_0)|$ to the corresponding sample. This is similar to the functionality of a typical lens in which different phase shifts are introduced to the different parts of the wave-front. However, a lens performs a fix wave-front manipulation which is determined in fabrication. On the other hand, the photonic receiver system has the capability of adaptively applying any phase and amplitude to the received wave-front on the chip. For the system demonstrated here, only phase shifting operation is considered for each captured sample using a tunable phase shifter. Therefore, the system can adaptively perform the functionality of any conventional lens on the chip. Moreover, since the phase shifts are adjusted precisely on the chip, the equivalent effect of the surface irregularity of conventional lenses is much lower. In particular, the equivalent lens of the photonic receiver chip is 1.55 µm thick with less than 2 nm surface roughness control.

In phased array processing [122] with uniform amplitude gain for the elements, a phase shift of

$$\Delta\phi(n, m) = \frac{2\pi}{\lambda}(nd \sin\theta_0 \cos\phi_0 + md \sin\theta_0 \sin\phi_0), \tag{4.5}$$

is applied to the signal received by the element at (n, m), $E(n, m)$. This phase shift cancels the propagation phase difference added to the samples for the wave incident at (θ_0, ϕ_0). Therefore, the received signals for the incident wave at (θ_0, ϕ_0) are in-phase after the phase shift is applied. Summing these weighted signals yields

$$\begin{aligned} E_R(\theta_0, \phi_0) &= \sum_{n=0}^{N-1} \sum_{m=0}^{M-1} E(n, m) e^{i\Delta\phi(n,m)} \\ &= \sum_{n=0}^{N-1} \sum_{m=0}^{M-1} \int_0^{2\pi} \int_0^{\pi} G(\theta, \phi) E_i(\theta, \phi) \exp^{i(\Delta\phi(n,m) - \frac{2\pi}{\lambda}\Delta l(n,m))} d\theta d\phi. \end{aligned} \tag{4.6}$$

$$E_R(\theta_0, \phi_0) = \int_0^{2\pi} \int_0^{\pi} G(\theta, \phi) P(\theta, \phi, \theta_0, \phi_0) E_i(\theta, \phi) d\theta d\phi. \tag{4.7}$$

$$P(\theta,\phi,\theta_0,\phi_0) = \sum_{n=0}^{N-1}\sum_{m=0}^{M-1} e^{-i\frac{2\pi d}{\lambda}\left[n(\sin\theta\cos\phi-\sin\theta_0\cos\phi_0)+m(\sin\theta\sin\phi-\sin\theta_0\sin\phi_0)\right]}. \tag{4.8}$$

$P(\theta,\phi,\theta_0,\phi_0)$ is the array pattern or array factor at angle (θ_0,ϕ_0) and is a function of element spacing, d normalized to the wavelength and the number of elements in each direction, N and M. The total receiving pattern of the whole system is the product of the array pattern and the receiving element pattern, $G(\theta,\phi)\ P(\theta,\phi,\theta_0,\phi_0)$, and determines the coupling strength for the incident wave at each direction. In the Fourier optics context, such a function is called the point spread function, PSF. The receiving pattern of the system has the shape of a beam pointing towards $(\theta=\theta_0,\phi=\phi_0)$. Therefore, the electric field $E_i(\theta_0,\phi_0)$ corresponding to all the receiving elements for the light impinging at the angle (θ_0,ϕ_0) constructively interfere and maximized the integral of equation (4.7) while light at other angles are averaged out and suppressed by the integration. In an OPA receiver, the receiving pattern $P(\theta,\phi,\theta_0,\phi_0)$ is adjustable by applying associated phase shifts for different angles to collect the wave $E_R(\theta_0,\phi_0)$ impinging at (θ_0,ϕ_0).

4.3 2D Receiver Aperture

The OPA receiver with a 2D aperture presented in this work has an 8-by-8 uniform array of compact nano-photonic antennas functioning as receiving elements. Each antenna collects the incident free-space propagating light and couples it into an on-chip waveguide at its output port. Figure 4.2 shows the design of the receiving antenna. The antennas are optimized to collect the electromagnetic wave at $\lambda = 1,550nm$ with a compact footprint of 5 µm by 2 µm. It consists of three silicon slabs to diffract the light and a tapered quadratic mode converter to focus and couple the collected light into the output waveguide mode. The mode converter is also tapered vertically using two etch levels and the spacing between the diffracting slabs are optimized to achieve the maximum receiving effective area. The normalized antenna reception pattern and and a the antenna effective aperture versus elevation angle θ_x are shown in Figs. 4.2(c) and 4.2(d), respectively. This antenna achieves a maximum effective area of 1.33 µm^2 for an incident wave at $-8.6°$ and 1.55 nm wavelength. The bandwidth of the system is determined primarily by the reception bandwidth of the antenna, which has a 3 dB bandwidth of 43 nm in this design.

Figure 4.2(c) shows the element placement and signal routing for the OPA system, which has a FOV of 8° determined by the aperture element spacing of 11.2 µm.

This spacing is limited by the antenna size, routing waveguide size and the required minimum spacing between the waveguides, as well as the number of elements in each row and column. The aperture of an OPA transmitter suffers from the same limitations. Recently, novel solutions have been proposed for OPA transmitters to reduce the element spacing and increase the FOV such as sparse [21] and non-uniform [85] element placement and multi-layer photonics [123], [124] that can be adopted for the receiver as well.

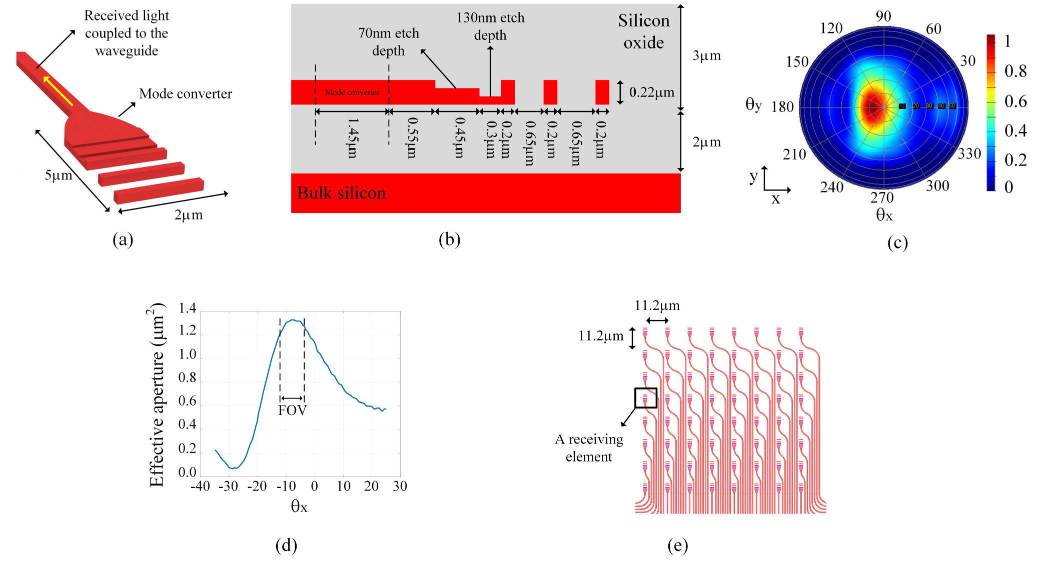

Figure 4.2: (a) A single receiving element (b) cross section of the receiving element with detailed dimensions (c) Reception pattern of a single element, $G(\theta, \phi)$ (d) Effective aperture of the receiving element versus θ_x (e) The 8-by-8 array of receiving elements.

The array pattern $P(\theta, \phi, \theta_0, \phi_0)$ for $(\theta_0 = 0, \phi_0 = 0)$ is shown in Fig. 4.3 for two different element spacings. The finite beam width of the main lobe is due to the limited extent of the aperture leading to an artifact similar to the diffraction limit for imaging systems and lenses.

In addition to the main lobe the array pattern $P(\theta, \phi, \theta_0, \phi_0)$ includes a number of grating lobes for $d > \lambda/2$ [72] as well because of the periodicity of $e^{i\theta}$ with period 2π (equation (4.8)). For $d \leq \lambda/2$ only a single period appears in the pattern and thus the array pattern has no grating lobe and the incident wave-front $E_i(\theta, \phi)$ can be reconstructed for $0 \leq \theta \leq \pi/2$ and $0 \leq \phi < 2\pi$. The presence of the grating lobes affects the performance of the system through aliasing as predicted by sampling theory by picking up unwanted signals from the direction of grating lobes and overlay them on the desired signal. Since the total pattern is the product

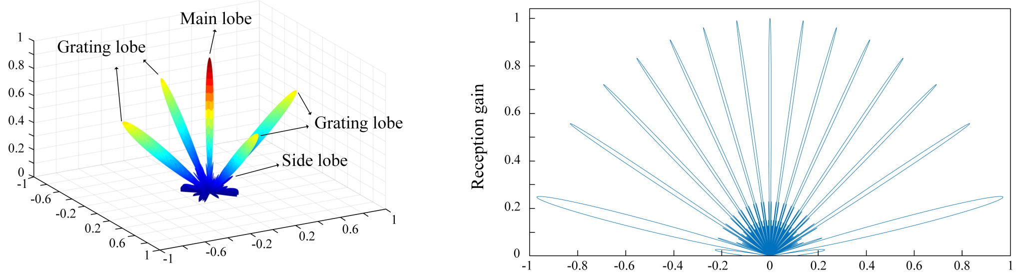

(a)

(b)

Figure 4.3: (a) Array pattern of an 8-by-8 array with $d/\lambda = 1.3$ and $(\theta_0 = 0, \phi_0 = 0)$ (b) Array pattern of the designed OPA receiver for $\phi = 0$ and $(\theta_0 = 0, \phi_0 = 0)$ (element spacing = $11.2\mu m$). It is assumed that one side of the chip is blocked and light impinging on the aperture comes only from $0 \leq \theta \leq \pi/2$

of the array pattern and the antenna pattern, the grating lobes can be suppressed by engineering the element pattern, $G(\theta, \phi)$. Moreover, a physical spatial filter can be used to block the light impinging from the unwanted direction and limit the FOV. Therefore, the FOV of the system is defined by the grating-lobe-free steering range or the aliasing free range which is the maximum angular range that can be received and reconstructed. In addition to the grating lobes, side lobes [72], which are other minor picks in $P(\theta, \phi, \theta_0, \phi_0)$, can reduce the accuracy of the reconstruction. The average side lobe level is inversly proportional to the number of elements and decreases as the array scales.

4.4 Optoelectronic mixer

In many real situations, the received light by the antennas is a weak signal. The minimum signal level that a receiver is capable of detecting for a given signal-to-noise-ratio (SNR) defines the sensitivity of the system. Therefore, a high performance receiver should detect and amplify the received signal while introducing the least amount of extra noise. In electronic receiver systems, to reduce the impact of the added noise of the receiver blocks, the received signal is amplified using a low-noise amplifier first. The stronger amplified signal is more robust to the detrimental effects of the noise of the subsequent detection and processing stages. Unfortunately, such a low noise amplifier is not available for integrated silicon photonic systems. An electronic low-noise amplifier can be used after photodetection to reduce the impact of the electronic noise of the following receiver stages. However, the losses and added noises before the LNA such as the photodetector noises severely reduces the

SNR of the signal.

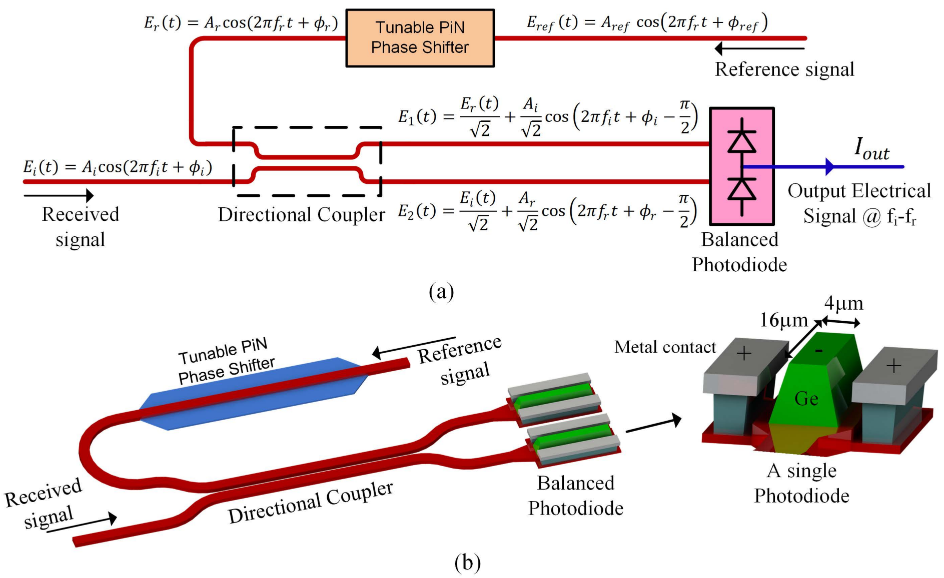

Figure 4.4: (a) Block diagram of the optoelectronic mixer (b) simplified drawing of the integrated optoelectronic mixer.

In this work, to suppress the impact of the optical loss and detection noises an optoelectronic down-conversion mixer is designed as the first stage of the receiver chain. The mixer is input a reference light in addition to the received signal and down-converts the received signal to radio frequencies while preserving the signal information. The output signal is also amplified through the conversion and thus the received optical wavefront can be robustly processed in the electronic domain with stronger signal processing tools.

The designed optoelectronic mixer is shown in Fig. 4.4 which includes a 90-degree hybrid directional coupler[57], [125], a PiN diode phase shifter in the reference path, and two photodiodes forming a balanced photodiode [126], all of them integrated on the chip. The mixer is fed with the received signal and the reference signal at its two optical ports and generates a current at its electrical output port. The PiN phase shifter is a pin-diode and introduces optical phase shift through the carrier injection effect [127]. Passing a current through the PiN diode determines the phase shift provided by the phase shifter which is can be adjusted on a range more than 2π and thus capable of adding an arbitrary phase to the reference signal. Figure 4.5(a) shows the cross section of the designed PiN diode phase shifter in which a p+ and an n+ region form the anode and cathode of the diode, respectively. The silicon waveguide in between the two doped regions is the the intrinsic region of the PiN diode as well as an optical path for light. As shown in Fig. 4.5 the distance between the doped regions and the optical mode provides a safe margin to prevent optical loss. The phase shifter structure is 500 µm long and for 28 mA of injected current provides a 2π phase shift. Moreover, there is a 25 µm spacing between the adjacent mixers on the chip that results in a negligible thermal and electrical cross-talk between the phase shifters. The directional coupler is formed using a symmetric structure of closely spaced waveguides. An epitaxially grown germanium layer is used to form the two photodiodes with the size of each photodiode being 16 µm by 4 µm.

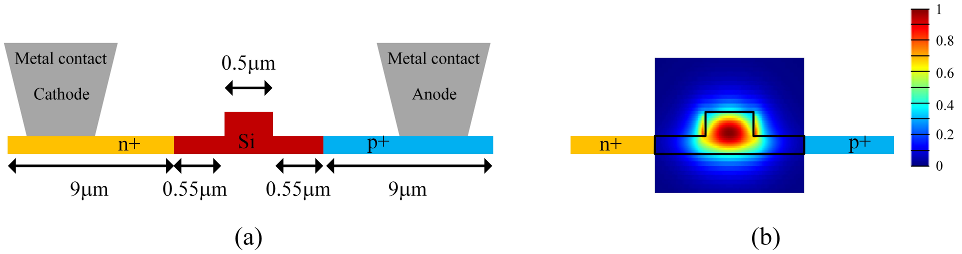

Figure 4.5: (a) Structure of the PiN diode phase shifter (b) Optical mode propagating inside the phase shifter (the doped regions do not interfere with the optical mode, avoiding optical insertion loss).

To understand the functionality of the mixer, the signal flow through the structure, Fig. 4.4, can be considered. The phase of the reference light which can be arbitrarily modified is adjusted to ϕ_r by the PiN phase shifter. The received light by the antenna and the adjusted reference signal, which are

$$E_i(t) = A_i \cos(2\pi f_i t + \phi_i), \tag{4.9}$$

$$E_r(t) = A_r \cos(2\pi f_r t + \phi_r), \tag{4.10}$$

respectively, are then fed into the two input ports of the directional coupler using on-chip waveguides. Therefore, the 90-degree hybrid directional coupler evenly distributes the input optical power of each port between the two output ports and yields the sum of the two input signals. Moreover, the transferred signal to the through port of the directional coupler (for each input port) experiences a 90° phase shift [57]. Therefore, the two output waves of the directional coupler in the form of a low-frequency envelope and an optical carrier at frequency $(f_i + f_r)/2$ are

$$E_1(t) = \frac{1}{\sqrt{2}}\left(A_r^2{+}A_i^2{+}2A_rA_i\cos(2\pi(f_i{-}f_r)t{+}\phi_i{-}\phi_r{-}\pi/2)\right)^{\frac{1}{2}}\cos(2\pi\frac{f_i+f_r}{2}t{+}\psi(t)). \tag{4.11}$$

$$E_2(t) = \frac{1}{\sqrt{2}}\left(A_r^2{+}A_i^2{+}2A_rA_i\cos(2\pi(f_i{-}f_r)t{+}\phi_i{-}\phi_r{+}\pi/2)\right)^{\frac{1}{2}}\cos(2\pi\frac{f_i+f_r}{2}t{+}\psi(t)). \tag{4.12}$$

It can be seen that the two 90° phase shifts lead to 180° out of phase envelopes or beat components at the two output ports. Feeding these signals into the photodiodes generates photo-currents which are proportional to the optical power determined by the envelope of the optical signal squared, divided by two [126], [128]. Therefore, the total output current which is the combination of the two photo-currents is

$$I_{out}(t) = (RA_r)A_i\sin(2\pi(f_i-f_r)t+\phi_i-\phi_r) = 2R\sqrt{P_rP_i}\,\sin(2\pi(f_i-f_r)t+\phi_i-\phi_r), \tag{4.13}$$

in which R is the responsivity of the photodiode and $(f_i - f_r)$, beat component frequency. The beat component frequency is adjusted to be a few Megahertz due to the convenient and quality of electronic processing at these frequencies. However, any frequency range that electronic components meet the bandwidth and accuracy requirements of the down-converted signal can be used. As equation (4.13) shows, both amplitude and phase of the received signal are preserved at the output current. Moreover, the amplitude of the reference signal appears as a gain factor at the output and its phase provides an tuning parameter for adjusting the phase of the output current through the PiN phase shifter. In case of the phased array processing, the reference phase ϕ_r for the receiving element at (n, m) can be adjusted to $\Delta\phi(n, m)$. In a standard 50 Ω system, the amplitude gain factor corresponds to the power gain of $P_{electrical}/P_i = 100R^2P_r$. Heterodyne detection scheme used in the mixer topology provides an extra conversion gain of P_r/P_i compared to the direct detection with power gain of $P_{electrical}/P_i = 100R^2P_i$. This gain factor can be used to amplify the signal in the optical domain by increasing the magnitude of the reference signal effectively at the first stage of the receiver chain.

In addition to providing a gain factor, the phase shift control of the mixer is embedded in the reference path leaving the received signal path undisturbed. Another advantage of this system is that amplitude control can be achieved by either controlling the reference signal amplitude or electronic amplification of $I_{out}(t)$. Moreover, the stray light and interferers that reach the photodiode produce near-DC components at the output that are distinguished from the beat frequency $(f_i - f_r)$ and can be easily filtered electronically. Furthermore, the $1/f$ noise components of the post-processing electronic blocks can also be filtered without disturbing the spectral content near the beat frequency.

As discussed, the optoelectronic mixer provides the capability of tuning both the amplitude and phase of the output signal by adjusting the phase and amplitude of the reference signal as well as manipulation of the current in the electronic domain. Due to the short wavelength of the optical signals, phase shift operation in the optical domain is especially desired due to the simpler and more accurate optical phase shifter implementations. On the other hand, amplitude adjustment using a variable gain amplifier in the electronic domain is much more efficient. Moreover, since both amplitude and phase of the received signal are preserved at the output current, further more complicated signal detection processing techniques can be performed in the electrical domain to improve the sensitivity and accuracy of the receiver system.

To improve the SNR of the detected signal, the conversion gain of the optoelectronic mixer, RA_r, can be increased by increasing the reference signal level. This leads to a stronger output mixed component while the shot noise associated with the photodiode dark current and the electronic noise sources later in the chain remaining the same. The output current of a single photodiode is

$$I_{tot} = \frac{I_{out}}{2} + I_{Dark} + \frac{RP_{ref}}{2} + \frac{RP_{Rx}}{2}, \tag{4.14}$$

in which P_{ref} and P_{Rx} are the reference and received signal powers, respectively, and I_{Dark} is the dark current flowing through the photodiode due to its bias voltage. Therefore, the SNR of the detected signal after passing through the receiver chain is

$$SNR = \frac{P_{signal}}{P_{noise}} = \frac{(2R^2 P_{ref} P_{Rx})}{(4eI_{tot} + \overline{I^2}_{n,TIA})BW} \cong \frac{RP_{Rx}}{eBW} \frac{1}{1 + \frac{2I_{Dark} + \overline{I^2}_{n,TIA}/2e}{RP_{ref}}}, \tag{4.15}$$

where BW the signal bandwidth, $\overline{I^2}_{n,TIA}$ the current noise power spectral density of the electronic circuitry referred to the input of the transimpedance amplifier (TIA), and e is the charge of an electron. While increasing P_{ref} improves the SNR, the SNR of the system has an upper limited of

$$SNR \cong \frac{RP_{Rx}}{eBW}. \tag{4.16}$$

As the SNR approaches this limit, little improvement is achieved through increasing P_{ref} and the SNR depends mainly on the received signal power. In this situation, the receiver system operates in the shot noise limited regime and the detected signal is robust against the detrimental noise sources in different receiver blocks.

4.5 Design and fabrication of the OPA receiver

The OPA receiver is fabricated in a standard silicon photonic process with a single photonic layer. The photonic layer is a 220 nm thick silicon slab with two etch levels of 70 nm and 130 nm and is used for designing optical components. The nano-photonic antennas in the 8-by-8 array aperture (Fig. 4.2) receive the incident light and feed it into single-mode dielectric waveguides. The waveguides are 0.5 μm in width, and are used for routing the optical signals on chip with a negligible insertion loss. A dedicated optoelectronic mixer is used for every received signal by an antenna. A strong laser light for the reference signal is coupled to the chip through a focusing grating coupler and split into 64 equal-power branches using a 6-level binary splitter tree. Each branch feeds the reference input port of a mixer. The cathode of the PiN-diode phase shifters are tide together and shorted to the electrical ground pin while the anodes are routed to separate pads. The pads are accessed through off-chip electronic drivers to control the phase shifts in each mixer independently.

The simplified schematic of the designed OPA receiver architecture with only 4 elements is shown in Figure 4.6(a). Since the phase shifts are independently adjusted by the PiN phase shifters, summing the output current yields the phased array processing output of equation (4.6). The summation is achieved through the Kirchhoff current law by simply connecting all the mixer output nodes together. If the phase shifter associated with the antenna element at (nd, md) is adjusted to $\Delta\phi(n, m)$, the the total output current (after summation) is the phased array output signal. This current is routed to an on-chip pad and transferred off-chip for further electronic amplification and processing. Figure 4.6(b) shows a die photo of the fabricated chip and zoomed-in images of the building blocks.

The total output current of the photonic chip with the adjusted phase shifts is

$$I_{tot} = \frac{I_{out}}{2} + I_{Dark} + \frac{RP_{ref}}{2N_{rx}} + \frac{RP_{Rx}}{2}, \tag{4.17}$$

in which P_{ref} is the total reference power, P_{Rx} is the received signal powers, I_{Dark} is the dark current flowing through the photodiode, and the number of receiver

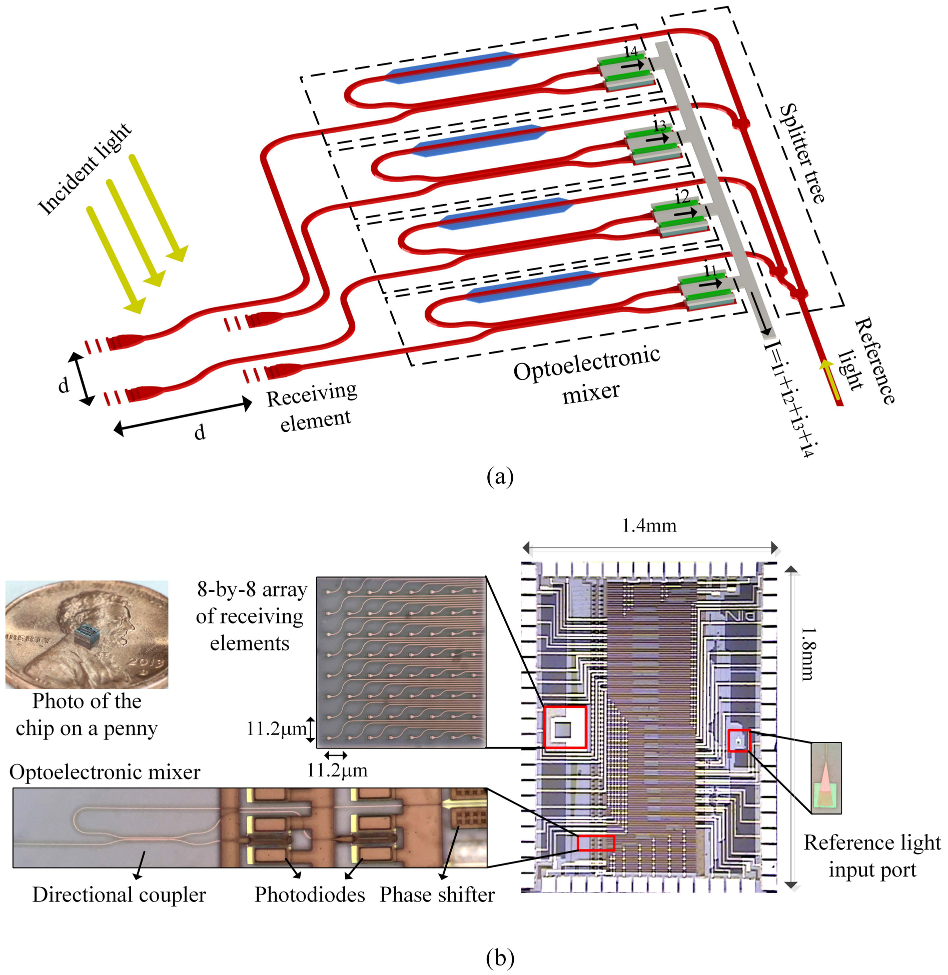

Figure 4.6: (a) A simplified diagram of the receiver architecture with a 2-by-2 array aperture. (b) Photo of the fabricated chip and the building blocks.

element in the phased array is denoted by N_{rx}. For a particular reception angle, the signals from the balanced detectors add coherently. Therefore, the total signal to noise ratio, SNR, of the receiver phased array is

$$SNR = \frac{P_{signal}}{P_{noise}} = \frac{N_{rx}(2R^2 P_{ref} P_{Rx}/N_{rx})}{(4eI_{tot} + \overline{I^2}_{n,TIA})BW} \cong \frac{N_{rx} R P_{Rx}}{BW(e + \frac{2N_{rx} I_{Dark} + \overline{I^2}_{n,TIA}}{2RP_{ref}/N_{rx}})}, \quad (4.18)$$

with $\overline{I^2}_{n,TIA}$ the current noise power spectral density of the electronic circuitry referred to the input of the trans-impedance amplifier (TIA), BW the signal bandwidth, and e the charge of an electron. By increasing P_{ref}, the system SNR is limited by the shot-noise of the photo-diodes,

$$SNR \cong \frac{N_{rx} R P_{Rx}}{eBW}. \quad (4.19)$$

At this limit, SNR depends only on the total received signal power collected by all the receiver elements and can be improved by having a larger number of receiving elements. As a result, this system is robust to the detrimental noise sources in the detection chain.

The noise performance of the receiver system is critical in ranging and sensing applications. To increase the sensitivity, a directive transmitter should be used to focus the light on various points through steering [ ] [ ] [ ]. Therefore, sending light from the transmitter to the target does not involve any free-space traveling loss. If the OPA receiver presented in this work is used for ranging and assuming a target with reflection coefficient of σ, based on radar equation [39], to obtain a given SNR, transmitted signal level of

$$P_{Tx} = \frac{(4\pi r)^2}{64\sigma G_{Rx}\lambda^2} \cdot \frac{eBW}{2RSNR} \tag{4.20}$$

is required in which $G_{Rx} = 34$ is the directivity of the designed receiving elements, r is distance the object is placed at, $\lambda = 1.55\mu m$ is the wavelength of optical signal, and 64 accounts for the number of elements in the array. For signal bandwidth of 1KHz, and SNR of 10, transmitted signal power required to detect the reflections back from an object in 100m is $P_{Tx} = 0.96W$. This shows the potential of these architectures to be used in ranging and sensing applications. Moreover, scaling the aperture to have a larger number of elements reduces the required transmitted power and improves the system efficiency.

4.6 Characterization and Measurement

To characterize the PiN phase shifter, a Mach-Zehnder interferometer (MZI) test structure, Fig. 4.7(a), is fabricated on the same chip with a phase shifter replica in one of its arms. The input light is split into two equal power branches, the phase shifter introduces an extra phase shift to one arm, and the two branches are combined back into a single waveguide providing an interference result. Therefore, the two branches constructively interfere for zero phase shift (produce maximum output power) and fully destructively interfere for π phase shift (leading to ideally zero output power). Figure 4.7(b) shows the variation of MZI output optical power as well as the added phase shift (calculated according to the output power) versus the injected current into the phase shifter. This measurement shows that for 14 mA of injected current a π phase shift is introduced by the phase shifter. Fig. 4.7(c) shows the loss and power consumption of the phase shifter versus the injected current. The insertion loss of the phase shifter is 0.3 dB and its active loss for phase shifting is 0.17 dB/mA. The measured frequency bandwidth of the designed PiN-diode phase shifter is 707 MHz which is limited by the on-chip routing and pad parasitics as well as the parasitic components associated with the wire bonds. The intrinsic bandwidth of the PiN-diode phase shifter is in the range of several GHz, which requires integrated electronics and travelling wave structure design to be realized [127].

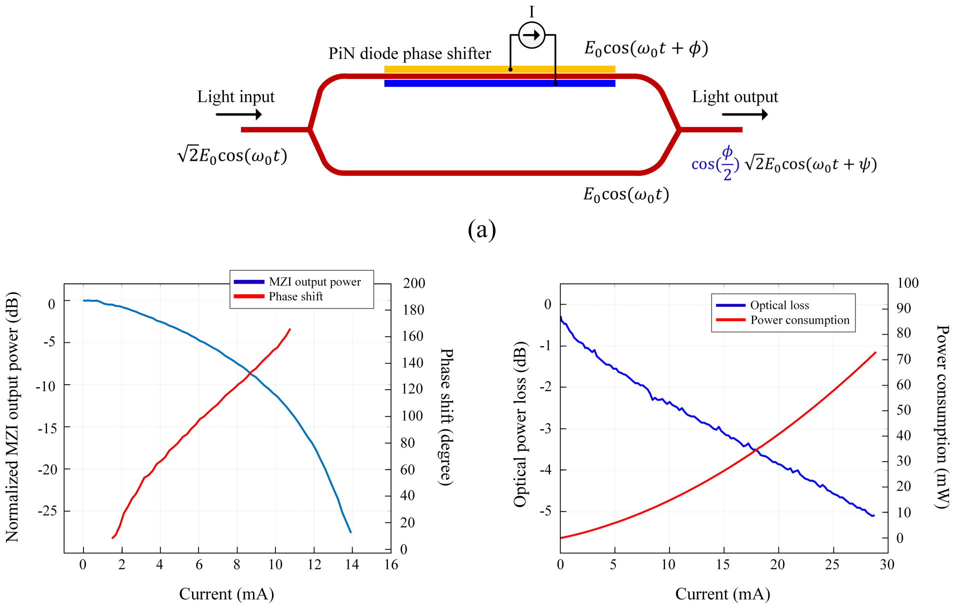

(b) (c)

Figure 4.7: (a) PiN diode phase shifter is placed in an MZI structure for characterizing the phase shift versus injected current (b) Output power of the MZI versus the electrical current passing through the diode, and the calculated associated phase shift of the PiN diode (c) Loss and power consumption of the PiN diode phase shifter versus electrical current passing through the diode.

The measured responsivity of a single photodiode is 0.4 A/W. The current noise of the 128 photodiodes in the receiver architecture are independent. Therefore, since the current of the photodiodes are added through Kirchhoff's current law, the noise power of the output current 128 times the noise power of a single photodiode. The dark current of a single photodiode versus the applied reverse bias is shown in Fig. 4.8. Here, a 0.5 V reverse bias is applied to the photodiodes to provide enough dynamic range while generating low additive noise associated with the dark current. This results in a total dark current of 2 μA at the output node and a current noise power of $6.4 \times 10^{-25} A^2/Hz$.

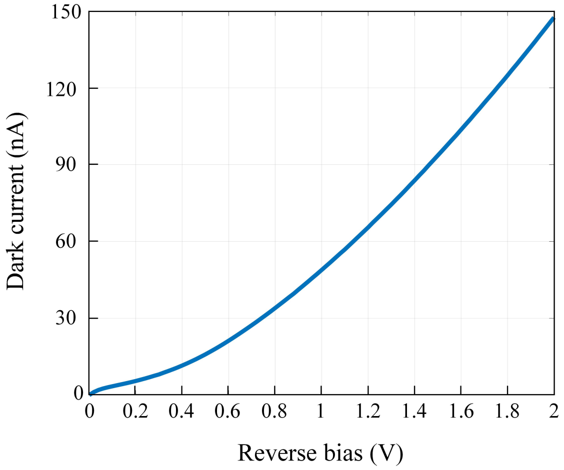

Figure 4.8: Dark current of a single photodiode versus the applied reverse bias.

Figure 4.9 shows the measurement setup. The photonic chip is mounted on a printed circuit board (PCB) which includes sixty-four driver blocks to control the phase shifters and a current readout circuitry to capture the output signal of the system. Each phase shifter driver block includes a 10-bit digital-to-analog converter (DAC), followed by an amplifier and a series resistor. The resistor is in series with the on-chip pin-diode and results in a wider dynamic range and more linearity for controlling the current flowing through the phase shifter. Therefore, by inputting a 10-bit binary value to the DAC, the current flowing through the phase shifter and thus its phase shift is controlled. A micro-controller provides the digital interface between the DACs and a desktop computer which sends the commands to program the DACs. A low noise TIA is used at the output of the receiver system to set the bias voltage of the photodiodes and amplify the total output current. The TIA is followed by an intermediate frequency (IF) detector that measures and digitizes the amplitude of the mixed component and sends it to the computer. Therefore, a closed feedback loop is formed so that the computer can read the output of the receiver chip and adjust the phase shifts accordingly.

The laser source providing the reference light and illumination always suffers from phase noise, i.e., random variation of the phase. Equation (4.13) shows that if there are variations in ϕ_i and ϕ_r the output mixed component will also adopt the variation as $\phi_i(t) - \phi_r(t)$. If two independent laser sources are used for reference and illumination, the corresponding phase noise components will also be independent, maximally add up, and degrade the sensitivity of the system [129]. To increase the sensitivity of the system the two lasers should be locked so that the phase noises

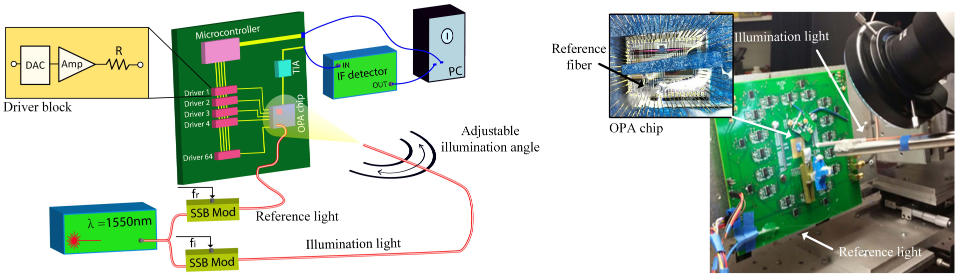

(a) (b)

Figure 4.9: (a) Diagram of the measurement setup (b) Measurement setup.

follow each other and partially cancel at the output. An ideal situation is using a single laser source for both reference and illumination signals and thus the phase noise components will be fully correlated. However, in real implementations, the two light paths will not be perfectly length matched and thus the two phase noises defer by a time delay ($\phi_i(t) = \phi_r(t - \tau)$). Therefore, minimizing the propagation length of the two path leads to a smaller residue in the subtraction and lowers the phase noise of the output mixed component. Here, a single laser source of 1.55 nm in wavelength with 100 KHz of line-width is used to provide both reference and illumination light. To generate two different frequencies f_i and f_r, two single-sideband (SSB) modulators are added to the reference and illumination paths to shift the optical frequency by 1.15 MHz and −1.75 MHz, respectively. Therefore, the frequency of the mixed component output by the system is $f_i - f_r = 2.9MHz$. While shifting the frequency of only one of the signals is sufficient for the operation of the system, having SSB modulators on both paths increases the extinction ratio of the mixed component over residual spectral content cause by SSB modulators non-idealities.

The reference light is coupled to the chip with a coupling loss of 6 dB and the fiber carrying it is fixed on the chip with a transparent glue. Each splitter of the splitter tree has an insertion loss of 0.3 dB and the on-chip waveguides used for routing the optical signals have a negligible insertion loss of 2 dB/cm. On the other hand, the illumination fiber is used as a source illuminating the chip from different angles. A reception beam at different angles is formed by adjusting the phase shifts according to equation (4.5). The receiver pattern for each beam is then measured by sweeping the illumination fiber over incident angles (θ, ϕ) and recording the amplitude of the output current. The measured beamwidth and maximum side lobe level for $P(\theta, \phi, 0, 0)$ are 0.75° and −10 dB, respectively. To form a beam at (θ_0, ϕ_0), its

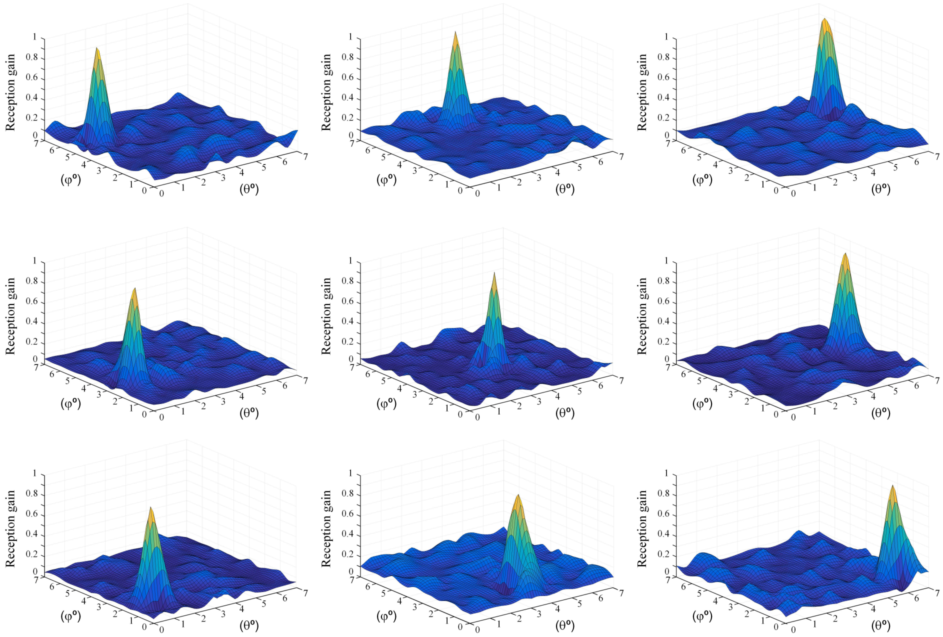

Figure 4.10: Measured reception pattern for various angles.

corresponding phase shifts should be adjusted through programming the DACs. Therefore, each beam setting has an associated DAC setting which is a repeatable setting and no phase shifter drift is observed in pattern measurements over different time spans. Figure 4.10 shows the measured pattern for several angles (θ_0, ϕ_0) over the FOV of the system.

The sensitivity of the receiver is characterized by carefully designing the receiver chain and considering all the noise sources. A two-stage with a transimpedance gain of $120,000\Omega$ is used to convert the output current of the chip into a strong voltage. This conversion gain is large enough for the noise floor of the output being determined by the TIA not the internal noise of the IF detector. The TIA produces a 120 nV output voltage in response to 1 pF of input photo-current which corresponds to −125 dBm output power in a 50 Ω system. In the absence of the optical signals, the measured output noise of the IF detector is −97 dBm/Hz, which is caused by the total electronic circuitry and photodiodes dark current noise. Therefore, the corresponding input referred noise of the TIA is $6.9 \times 10^{-22} A^2/Hz$. To achieve the maximum sensitivity according to equation (4.15), the shot noise of the photocurrent caused by the reference signal should dominate other noise sources which yields $2eRP_{ref} >> 6.9 \times 10^{-22} A^2/Hz \quad (P_{ref} >> 5.5mW)$. In practice, with $P_{ref} = 15dBm$, we achieved 3 dB higher noise floor as shown in Fig. 4.11. Considering the 6 dB coupling loss of the reference light and the total of 1.8 dB splitter-tree loss, this result is in a relatively good agreement with the theory. Therefore, the reference power of −11 dBm is delivered to each optoelectronic mixer which corresponds to a mixer gain of 79 dB for a −90 dBm (1 nW) of received signal. This reference power level is large enough for the effect of the noise of the TIA and photodiode to be negligible, which yields the maximum sensitivity of the system.

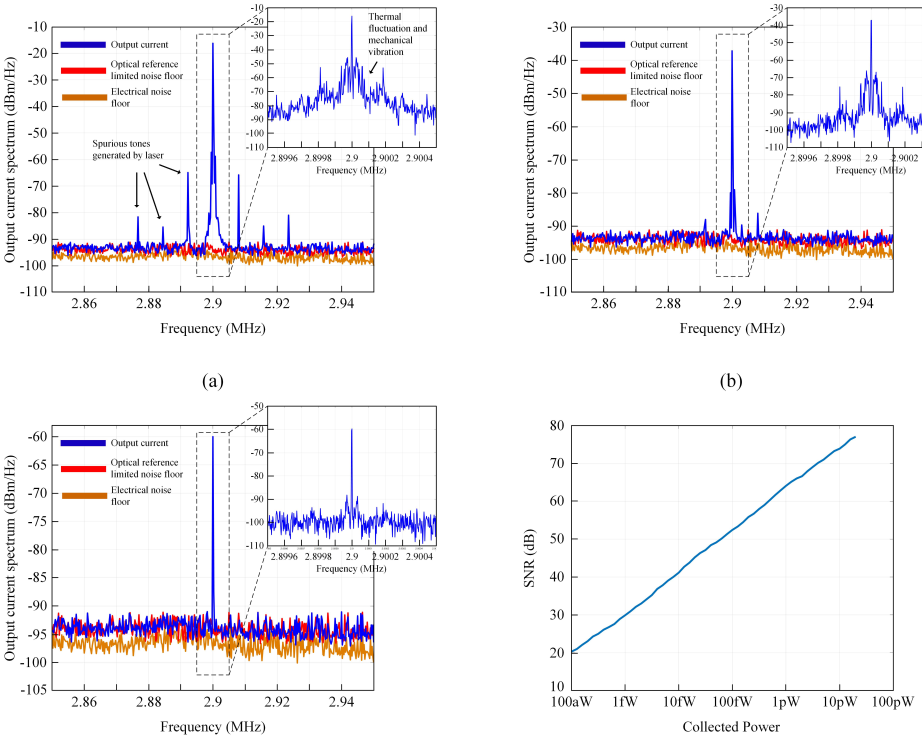

(a) (b)

(c) (d)

Figure 4.11: (a)-(c) Spectrum of the output signal with a 1Hz resolution bandwidth for 20pW, 200fW, and 2fW of collected power respectively. Red curve shows the noise floor due to the shot noise of the reference signal which is adjusted to be well above the electronic noise floor to gain the maximum sensitivity (d) SNR of the detected signal versus collected incident power.

Using the adjusted reference power level and TIA gain, the SNR of the detected signal versus the received incident power is measured. The illumination fiber distributes the light on a spot with 7.7mm diameter. The total collection area of the aperture (collected power by all the antennas) is $64 \times 1.33\mu m^2 = 85.12\mu m^2$. The measured power spectrum of the detected signal for three different collected power levels: 20pW, 200fW, and 2fW are shown in Figs. 4.11(a)-4.11(c) and the output SNR versus collected power is shown in Fig. 4.11(d). The spectral content of the output signal includes weak spurious phase modulation tones as well which originate from the laser source (Fig. 4.11(a)). If these spurious signals are the limiting factor for an application, a more stable laser with a narrower line-width can be used. In addition to the extra laser noises, thermal fluctuations and mechanical vibrations which are independent in the illumination and reference paths appear in the power spectrum of the output signal and limit the close-in SNR to 30 dB (Figs. 4.11(a)-4.11(c)). These variations that affect the stability of ϕ_i and ϕ_{ref} have a relatively low frequency bandwidth,usually less than 1 kHz, which is not considerable in many applications. The SSB modulators and multiple polarization controllers in the two path add a total of 10 m of fiber. Integrating the SSB modulators on the chip will eliminate the extra fiber, and significantly reduces the length difference between the two paths and consequently their uncorrelated thermal and mechanical fluctuations.

The directive reception capability of the OPA receiver enables this system to operate as a lens-less camera by steering the reception beam over the FOV and collect light selectively from all directions. Figure 4.12(a) shows the imaging setup arranged for demonstrating the imaging capability of the system. In this setup, a sheet of plexiglass is used as an imaging subject which is covered by copper and patterned to scatter light. This subject is placed in front of the chip and illuminated by the illumination fiber from the back side. Therefore, light wave with strong intensity travels toward the chip from the open spots while the covered areas are dark to the chip. Through the imaging process, the reception beam is steered across the FOV while the intensity of the collected light is recorded for each angle. Therefore, converting the recorded intensity into gray-scale and tiling them next to each other yields the image of the scene in front of the chip. Figure 4.12(b) shows the images taken by the 8-by-8 OPA receiver for multiple imaging subjects. While the pixel count and resolution of the image is limited by the reception beamwidth which is 0.75° for this OPA system, a larger margin for the beamwidth is considered here to achieve a more clear distinction between neighboring pixels and avoid the signal pick-up by the tail of the reception beam. To represent the imaging result, a 4×4 pixel array is used to illustrate the image formation details.

4.7 Conclusion

In this work, an integrated flat optical receiver architecture is demonstrated that captures the incident wavefront via sampling it with nano-photonic antennas and processes it on-chip. A high-performance integrated optoelectronic mixer is devised for down-converting the sampled optical signals received by each antenna to a radio frequency signal (which can be processed in the electronic domain) while preserv-

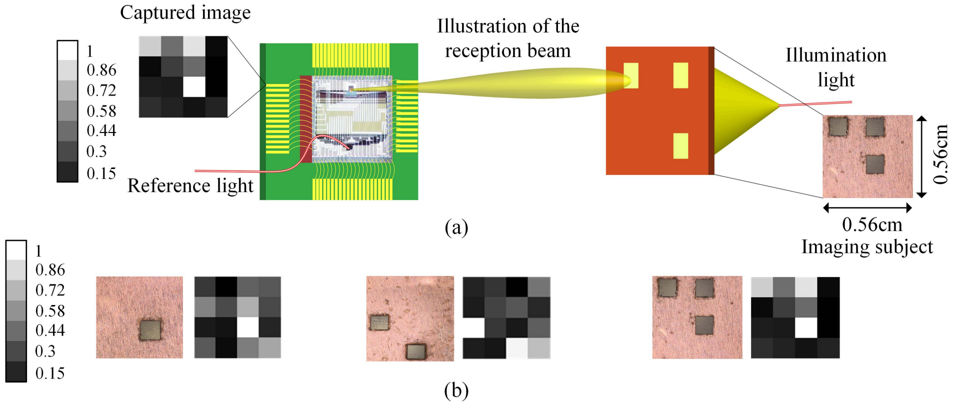

(a)

(b)

Figure 4.12: (a) Setup configuration for lens-less imaging (b) Images taken from imaging subjects.

ing their phase and amplitude information. The mixer provides a relatively large conversion gain and allows for a detection process robust to noise sources in the system. Moreover, stray light and interference signals coupled to the antennas and photodiodes are rejected through heterodyne mixing and filtering. The adjustable phase shifter embedded in the mixers in addition to the electronic domain gain control, provides arbitrary wavefront manipulation capability which can be performed to achieve the desired functionality. Using this system which functions as a thin on-chip adaptive flat optical receiver, the first high-sensitivity OPA receivers with a one-dimensional and two-dimensional apertures are presented. Beamforming and steering capability of these receiver chips are demonstrated and their lens-less imaging capability is proved via imaging an object by electronically steering the reception beam.

Chapter 5

OPTICAL PHASED ARRAY TRANSCEIVER

In this chapter, an integrated active flat optic system is presented which has the capability of high-sensitivity high-resolution 3D imaging. There are various challenges faced by integrated photonic systems in realizing robust high-resolution imagers. First, these challenges are discussed in detail and limitations of the current integrated architectures to address them are explained. Then, a double spectral sampling method is devised to employ the properties of both the nano-photonic transmitter and receiver to realize a transceiver with significantly enhanced performance. The transceiver illuminates multiple points simultaneously and records all the reflections at the same time while having the capability of extracting the information regarding each point and rejecting the unwanted signals. While addressing the signal integrity issues in 3D imaging, this transceiver also features low complexity and low power consumption. The parameters and the design of the building blocks of the implemented system are explained[1].

5.1 Introduction

The wavefront manipulation capability, high-sensitivity reception, as well as low fabrication cost and compact form factor make integrated photonics a good candidate for realizing 3D imagers. Moreover, its potential application in LiDAR (Light Detection And Ranging) [48] attracted a great deal of interest recently due to the increasing demand in 3D photography, self-driving cars, and next generation of smart phones. Conventional LiDARs, operating based on mechanical components, are bulky and expensive. Integration of nano-photonic projection/reception systems on a chip, capable of adaptive beamforming, holds a promising future for these applications due to their compact form factor, low cost, and high yield enabled by integrated solid-state platforms.

The output data of a 3D imager not only includes a picture of the scene being imaged, but also the distance of each pixel in the picture from the imager. A laser-based 3D imager works by introducing temporal variations to a coherent light wave which is used for illuminating the scene. The illuminated wave reflects from the objects and the imager determines the distance by measuring the round-trip time

---

[1] The work presented in this chapter was done in collaboration with Aroutin Khachaturian.

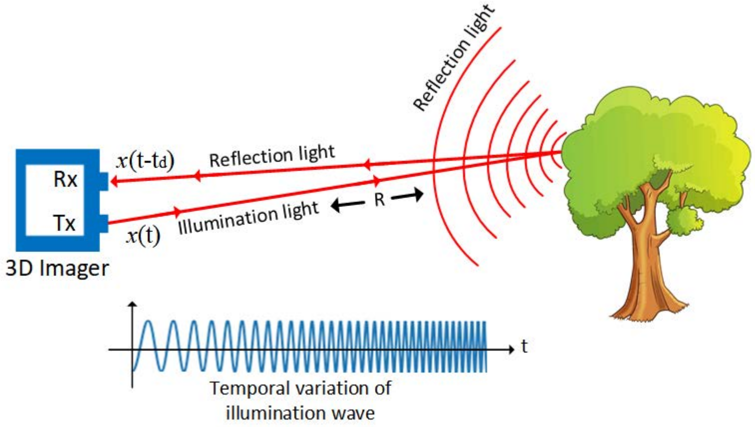

Figure 5.1: Conceptual schematic of 3D imaging with a LiDAR system.

of the wave, considering the speed of light in free-space. The round-trip time of the reflected wave can be calculated using knowledge of the history of the temporal modulation waveform. To perform imaging, the full scene can be flashed with the modulated laser light, followed by recording the reflections from all the points utilizing a lens and a detector array on the receiver side. However, due to the power limits of the available laser sources (those which are feasible to use and suitable for these applications) and eye safety restrictions, one point at a time is illuminated via forming a beam and the beam is scanned over the field-of-view to image the whole scene. This provides larger spontaneous optical power at each point and yields a higher SNR for the detection process. Figure 5.1 shows a conceptual schematic of such a 3D imager in which the transmitter (TX) illuminates a point with an optical beam and the receiver (RX) captures the reflection. The beam is steered over the FOV and measurements of the corresponding reflections are put together to form an image. The time delay (round-trip time) between the transmitted and received signals is

$$t_d = 2R/c, \tag{5.1}$$

in which R is the distance between the system and the object, and c is the speed of light. A large variety of waveforms can be used to modulate the illumination light such as pulsing and frequency chirping. For pulse modulation, a periodic sequence of short pulses with engineered amplitude (and even phase/frequency) are used to illuminate the scene. While post-laser optical modulators can be used to create pulses by gating the output light of the laser, the laser itself is usually designed to generate short pulses to avoid the optical power loss caused by the gating function of the modulator. In contrast to pulse modulation which is mainly an amplitude modulation scheme, frequency chirping varies the frequency of the laser light by linearly sweeping it between two frequencies periodically. A simple frequency chirped waveform is

$$x(t) = \begin{cases} A\cos(\omega_0 t + \frac{1}{2}\zeta t^2 + \phi) & 0 < t < T \\ x(t+T) = x(t). \end{cases} \tag{5.2}$$

While the optical frequency of the waveform is chirped in equation (5.2), an alternative modulation method is using a frequency chirp in the RF domain and employing the optical signal as a carrier. Therefore, the chirped signal is added to the optical carrier with an amplitude modulator following the laser. In this case the modulated laser waveform is

$$\begin{aligned} x(t) &= A(t)\cos(\omega_0 t + \psi) \\ A(t) &= \begin{cases} A_0(1+\alpha)\cos(\omega_m t + \frac{1}{2}\zeta t^2 + \phi) & 0 < t < T \\ A(t+T) = A(t). \end{cases} \end{aligned} \tag{5.3}$$

In addition to these chirp signals with a saw-tooth shape, triangular chirps and chirps with a continuous phase at cycle transitions [130] can be used to achieve better spectral properties.

Modulation and signal preparation are performed at the back-end processing of the transmitter. The front-end of the system performs conditioning and engineering the wavefront for illumination which mainly includes forming a nicely shaped beam and steering it. Among various methods of beamforming and steering discussed in section 2.3, electronic beamforming is desirable due to its reliability and faster scanning speed. While a silicon photonic platform is potentially capable of integrating all the system parts on the same chip, here, we only consider front-end wavefront processing on the chip. Using an array of nano-photonic antennas, an engineered wavefront can be generated for illuminating the scene which makes an optical phased array a candidate technology.

The reflected light is captured with an optical receiver and is compared to the signal in the transmission path (as a reference) to extract the time delay it experienced. In the case of amplitude modulation, such as pulse or amplitude chirp, a photodetector can be used to remove the optical carrier and extract the modulation signal through direct detection. Therefore, the calculation of the round-trip time can happen in electrical domain. For the case of amplitude/phase modulation, a simple photo-detector can not extract the variations and requires other techniques such as heterodyne detection for down-converting the optical signal to electronics for processing. However, a heterodyne mixing method can be used for amplitude modulations as well to achieve higher SNR for detection.

The comparison process between the reference signal and the received signal can be performed via calculating the correlation of these two signals. While various methods can be used to determine this correlation in the optical or electronic domains, it is also possible to integrated the correlation process and the photo-detection by using the modulated light in the transmitter as the reference for heterodyne detection. As an example, for frequency chirping of equation (5.2), the simplified output of the double balance heterodyne detection is [23]

$$I_{out} = Het\{x(t), x(t - t_d)\} = 2RA_0^2 + 2A_0^2 \cos(\zeta t_d t + \psi), \tag{5.4}$$

in which R is the responsivity of the photo-diode. Therefore, the mixer output current is a sinusoidal wave and its frequency is an indication of the time delay t_d. It should be note that the periodicity of the modulation signal is not considered here which leads to a periodic output signal with instantaneous frequency of ζt_d while its Fourier spectrum includes delta functions at integer multiples of $\omega_m = 1/T$. The heterodyne detection mixer can perform as a correlator for the amplitude chirp, equation (5.3), as well although some extra spectral content will be generated at the output current due to the varying amplitude which need to be filtered carefully.

While the operation principle of an optical 3D imager is well-known, utilization of integrated photonic as system front-end (on both of the transmitter and receiver sides) put forth many challenges. These challenges are accentuated when there are stringent performance requirements such as the capability of detecting an object at 200 m distance with at least 3 cm resolution in the presence of near by objects at 1 m that reflect a much stronger signal. In the next section, a more detailed discussion of the challenges in such systems are presented and in section 5.3 the proposed integrated optical transceiver system overcoming these challenges is explained.

5.2 Challenges in implementing a large scale imager

While a functional chip-scale 3D imager is a very attractive technology, OPA transmitters and receivers investigated in the literature face several unresolved challenges that hindered the realizing of a system that meets the demands of a useful product. Overcoming all these challenges requires novel architectures that benefit from the advantages of both transmitter and receiver systems. Here, we discuss and illustrate the difficulties in designing an on-chip coherent imager system. In the following sections, the proposed multi-beam OPA transceiver is explained that opens a door to a fully functional system by overcoming all these challenges.

The most well-known obstacle in designing OPA systems is scaling the aperture to achieve a narrow beamwidth. While sparse aperture design discussed in Chapter 3 achieves narrower beamwidth without increasing the number of antenna elements, it comes with the cost of reduced beam efficiency. A non-uniform array can still be used to modify and improve the pattern characteristics such as sidelobe level. However, to achieve both narrow beamwidth and high beam efficiency, the number of array elements needs to increase. A uniform array with 1024 elements placed at $\lambda/2$ spacing yields a beamwidth of 0.1° in broadside which is an acceptable resolution for a 3D imager with a mega-pixel resolution. However, a phase shift controlled 2D OPA transmitter needs a 1024 by 1024 array (more than a million antennas) to achieve this image resolution and a 1D aperture OPA that utilizes wavelength sweeping to cover both directions requires a highly stable laser as well as a very narrow antenna pattern. An antenna with a narrow pattern (0.1°) has a long footprint and suffers from the fabrication induced non-idealities. While for a 1D aperture the antennas spacing can be reduced close to a single wavelengths and achieve a relatively large FOV, the routing difficulties, as discussed in Chapter 3, will impede the scaling of a single photonic layer 2D array without sacrificing the FOV.

The scaling of the OPA architecture is not limited to the aperture and as the number of antennas increases, the number of back-end photonic components such as phase shifters and splitters as well as the electronic interface and drivers will also scale proportionally leading to a very large and expensive photonic chip. In addition to the large footprint, power delivery to the photonic phase shifters and sinking the generated heat due to their power consumption is another OPA system design challenge. Assuming a 10 mW average power consumption for a thermal phase shifter, more than 10 W of power will be dissipated on an OPA system with a 1000 elements. The chip temperature rise due to the generated head and temperature variation when phase settings are changed can disturb the functionality of the photonic components on chip. Instead of low-speed thermal phase shifters, PN phase shifters with a relatively small power consumption can be used. However, these phase shifters suffer from both insertion loss and phase shift dependent loss and create other issues for the system functionality. Therefore, the desirable phase shifter should offer low loss as well as capacitive terminal impedance to achieve a tolerable power consumption on the chip.

Scaling the OPA will increase the optical loss of the system as well which is mainly due to the optical splitter insertion loss and the increased on-chip routing length. Moreover, fabrication mismatches will have more severe impact on a larger scale OPA. In particular, the larger number of power splitters will increases the non-uniformity of the power distribution between the antennas. Moreover, the random phase drift cause by fabrication induced non-idealities in photonic waveguides grows with waveguide length. Another scaling difficulty is the complexity of the electronic interface. The large size of the electrical pads and the number of electrical connections in two-chip solutions lead to a complicated interface and expensive packaging. While using monolithic integration or 3D integration of the two chips significantly reduce the interface complexity, they can potentially suffer from a lower yield and more expensive fabrication cost.

In addition to scaling the OPA system to achieve high resolution, to realize an on-chip OPA system with competing performance, the beam efficiency and sidelobe suppression are important factors that should be considered as well. Beam efficiency is the fraction of the radiated power inside the main beam. For a uniform phased array, the beam efficiency is 45% for 3 dB beamwidth and 80% for the null-to-null beamwidth. The fraction of the radiated power outside of the main beam not only reduces the illumination power on the desired spot and is effectively equivalent to optical loss, but also its reflection towards the detector causes interference and reduces the receiver sensitivity. These reflections are more detrimental when they reflect from a closer object compared to the reflection of the main beam. For instance, if main beam reflect from an object four times as far, it experience 12 dB more propagation loss (assuming the same reflectively for the objects). Moreover, since the spurious reflection comes back from broader range of angles and potentially multiple objects, a strong clutter will be formed flooding the main beam reflection signal. This effect is more exaggerated for the side lobes which are stronger peaks in the pattern. Based on the above explanation, a side lobe which is 12 dB smaller than the main lobe will have the same reflection magnitude. Therefore, a strong side lobe suppression and high beam efficiency is crucial for achieving high performance and resolving a high the objects with high accuracy.

The limited radiation efficiency of nano-photonic antennas is another source of spurious illumination. The optical power fed into an antenna is partially coupled to the free-space and a fraction of the power will travel towards the substrate or propagate forward. These waves can reflect from the bottom of the chip and/or interact with other photonic structure on the chip and leak into the free-space adding a random stray light to the illumination background. This effect can be severely detrimental particularly in photonic chips with a single photonic layer that the maximum achievable antenna efficiency is limited to about 60% (see Chapter 5) due to the close to symmetrical geometry of the design. Finally, if the optical wave is modulated off-chip or early on the transmitter chain, the fiber-to-chip coupling loss and any leakage from the waveguides and other photonic components can potentially cause a spurious illumination on the scene. These stray light has the same detrimental effect of the out-of-FOV fraction of power in radiation pattern and create a clutter in the detected signal spectrum.

The finite sidelobe level which is hard to reduce below 20 dB due to the temperature sensitivity of the phase shifters and phase tuning inaccuracy, leakage of the stray light to scene illumination, clutter, and external interference are the challenges the optical receiver should overcome to achieve high detection sensitivity. Therefore, having only a photodetector is not sufficient to resolve the desired signal and filter the unwanted parts. If an antenna array is used to capture the reflected wave, achieving a large enough effective area without exceedingly scaling the number of receiving elements and the receiver architecture poses new challenges for the design. More detailed discussions are presented in Chapter 6 regarding the approaches and techniques to improve the effective aperture of nano-photonic antennas on integrated platforms.

In addition to efficient wavefront shaping, generation, and reception, a useful 3D nano-photonic imager should have a repeatable and accurate performance as well. Non-idealities in the fabrication of integrated photonic chips degrade the similarity between the photonic components. Therefore, identically designed phase shifters will differ in the amount of phase shift they provide for a the same drive signal and a random phase drift will be experienced by light traveling in each waveguide. Such random deviations from the original design which vary from one chip to another necessitate a feedback mechanism for a calibration mechanism. Moreover, the phase shifter frequency response and phase shifting speed determines how fast the system can change the wavefront shape or steer a beam that eventually determines the imaging frame-rate. In many applications a real-time 3D imager is required, which sets a relatively high minimum beam steering speed of several hundred MHz.

5.3 Double spectral sampling transceiver array

The capability of integrated photonics to engineer the wave-front on both transmitter and receiver sides introduces extra degrees of freedom and an extended design space for novel architectures that can overcome practical challenges. Here, a double spectral sampling method is introduced with an under-sampled transmitter aperture followed by under-sampling the incident wave-front on the receiver aperture. While none of these two samplings are aliasing free, the beam shape of the generated wave-front provides unambiguous extraction of the information. The reduced complexity of this system on both transmitter and receiver sides significantly improves/solves the discussed challenges in the previous section.

The primary challenge of the array design for OPAs is reducing the element spacing while increasing the aperture size. Reducing the elements spacing increases the grating-lobe-free FOV with only a single lobe in the array pattern for $d = \lambda/2$, and a larger aperture size translates to a smaller beamwidth and correspondingly a higher illumination/imaging resolution. If the aperture size is increased by increasing the element spacing (without increasing the number of elements), beamwidth improves but the array pattern will include more grating lobes. On the other hand, reducing the element spacing with a constant element count reduces the aperture size and thus the width of the beam that can be generated by the aperture. Therefore, improving both of these factors for a uniform array simultaneously, necessitates scaling the number of elements in the array. However, as discussed in section 5.2, scaling the OPA system is not desirable due to the increased complexity of the system architecture, power consumption, optical loss, etc. Moreover, the large footprint of the nano-photonic antennas and optical coupling of closely spaced photonic components add more complications to the design and reduce system performance.

An alternative perspective to study this trade-off is considering an array aperture as a surface with a continuous excitation which is sampled at discrete locations and individual antennas are used to radiate these samples as impulse (point) sources. As explained in section 2.3, the far-field pattern of a radiating surface is the Fourier transform of the excitation on the surface (equation (2.3)). If the continuous excitation of the aperture $E(x, y)$ with a Fourier transform of $E_f(f_x, f_y)$ is sampled at discrete locations along the x and y axes with sampling periods of X_t and Y_t, respectively, according to the sampling theory [131], the Fourier spectrum of the samples is the overlay of $E_f(f_x, f_y)$ with all its replicas shifted by integer multiples of $1/X_t$ and $1/Y_t$ along f_x and f_y, respectively. In other words, the Fourier spectrum of the sampling is

$$E_{fs}(f_x, f_y) = \sum_{m_x=-\infty}^{+\infty} \sum_{m_y=-\infty}^{+\infty} E_f(f_x + \frac{m_x}{X_t}, f_y + \frac{m_y}{Y_t}). \tag{5.5}$$

Propagation towards the far-field has a low-pass filtering effect on the spectral content [7] such that only spectral components with

$$f_x^2 + f_y^2 \leq \lambda^2, \tag{5.6}$$

will be present at the far-field. This effect can also be understood by studying equation (2.3) which shows that there are no real valued angles θ and ϕ corresponding to the spatial frequencies f_x and f_y out of this range. Therefore, equation (5.6) specifies the spectral components that form the far-field which is called the *visible range*. For 1D arrays, Y and f_y can be ignored to simplify the analysis without loss of generality and array pattern is studied for $\phi = 0$. Therefore, the visible range for a 1D array reduces to

$$|f_x| \leq \lambda, \tag{5.7}$$

and

$$f_x = \frac{1}{\lambda} \sin\theta. \tag{5.8}$$

Here, for presentation clarity purposes, we do not show the low-pass filtering effect in the derivations while its effect is considered.

Assuming that the spectral components of the continuous excitation $E(x, y)$ are mainly inside the visible range, for sampling periods of $X_t = Y_t = \lambda/2$, the spectral replicas will fall outside of the visible range and are far enough to avoid aliasing in the far-field, Fig 5.2(b). Therefore, these replicas (which are artifact of sampling) are filtered out by the low-pass property of free-space propagation and will not affect the radiation pattern. Increasing the element spacings X_t and Y_t which translates to reducing the sampling frequency can causes aliasing and more than one replica of the spectral content will appear in the visible range. For instance, for element spacing $d = \lambda$, 2 replicas are present in the far-field, Fig. 5.2(c), and for $d = 2\lambda$, 4 replicas.

While undersampling might leads to aliasing in general, if the aperture excitation is adjusted to form a beam, its Fourier transform is localized in only a fraction of the visible range, and sampling will not cause any spectral overlap or aliasing (Fig. 5.3), and thus the replicated beams are still distinguishable. In other words, the grating lobes which are formed due to aliasing do not overlap even if only two samples

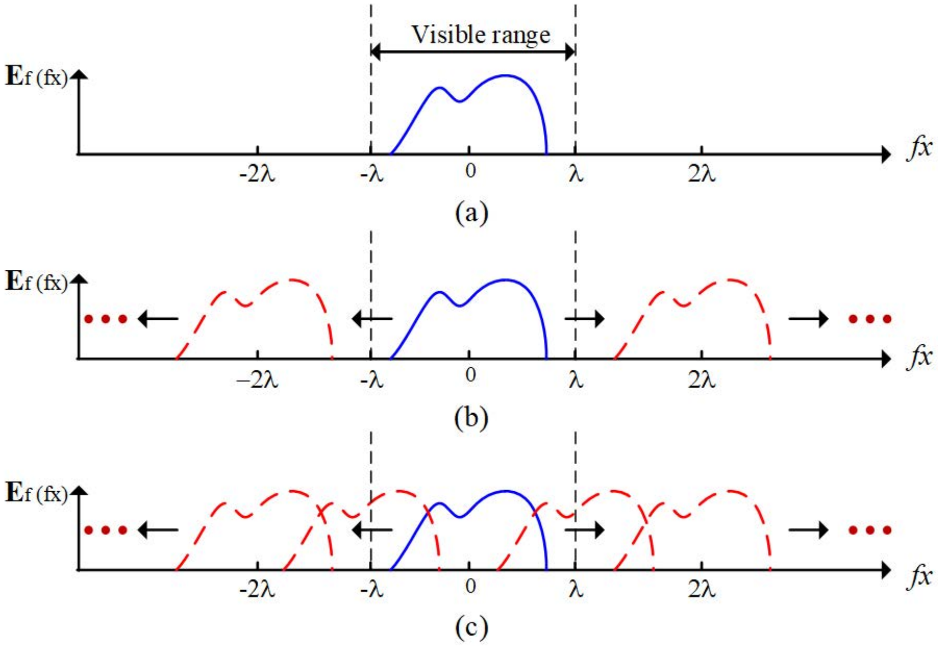

Figure 5.2: (a) Fourier transform of the aperture excitation which is simplified to one dimension (1D array) $E_f(f_x, f_y)$ (b)

are used in each dimension for the whole aperture. Therefore,undersampling the aperture yields a multi-beam transmitter and each beam covers a fraction of the FOV through beam steering.

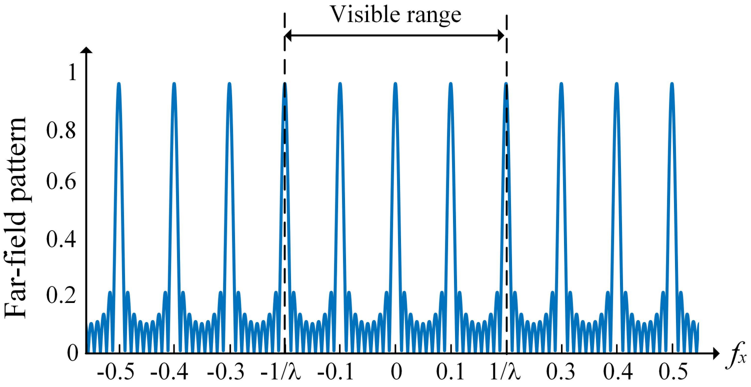

Figure 5.3: (a) Undersampling an aperture which is tuned to form a beam does not lead to aliasing.

Since an undersampled transmitter radiates multiple beams, the receiver used to record the reflection needs to be directive to separate the signals coming back from each beam. Therefore, the waveform of the incident wave-front should be captured by the receiver to extract information about the direction of incidence[2]. A single photodetector can not be used for this purpose since it does not record any information about the shape of the incident wave and only measures the incident amplitude. To record the electric field distribution on the receiver aperture an array of receiving elements can be used to sample the impinging wave-front. Since propagating back from the far-field to the receiver adds another Fourier transformation to the field distribution, the spectrum of the received wave is the same as equation (5.5) due to the Fourier transform *duality* property. The effect of sampling on the receiver aperture with antennas which are spaced X_r and Y_r apart along x and y directions leads to a spectral content of

$$E_{Rxfs} = \sum E_f(f_x + \frac{m_x}{X_t} + \frac{n_x}{X_r}, f_y + \frac{m_y}{Y_t} + \frac{n_y}{Y_r}), \tag{5.9}$$

in which *sum* is over all the indices. This equation can be modified to

$$E_{Rxfs} = \sum E_f(f_x + \frac{m_x X_r + n_x X_t}{X_{tr}}, f_y + \frac{m_y Y_r + n_y Y_t}{Y_{tr}}), \tag{5.10}$$

$$X_{tr} = X_t X_r \quad \text{and} \quad Y_{tr} = Y_t Y_r. \tag{5.11}$$

Therefore, the undersampling on the receiver aperture adds extra aliasing components to the spectrum. If the width of the beam is small enough such that all the shifted replicas of $E_f(f_x, f_y)$ are separated which translates to

$$\frac{(m_x - m_x^{'})X_r + (n_x - n_x^{'})X_t}{X_{tr}} \geq BW_x \quad if \quad (m_x, n_x) \neq (m_x^{'}, n_x^{'}), \tag{5.12}$$

and

$$\frac{(m_y - m_y^{'})Y_r + (n_y - n_y^{'})Y_t}{Y_{tr}} \geq BW_y \quad if \quad (m_y, n_y) \neq (m_y^{'}, n_y^{'}), \tag{5.13}$$

there is no overlap between the replicated beams and the information can be extracted. If equation (5.12) is not met, the overlap between the replicas will create large side lobes. Moreover, this equation does not considered the amplification of side lobes created by one aperture with a grating lobe of the other. Therefore, to achieve the optimum values of $X_{t,r}$ and $Y_{t,r}$ for minimum side lobe, we can perform an optimization over these parameters. For a 1D OPA transceiver, only X_t and X_r are relevant which are the sampling periods (element spacing) on the transmitter and receiver, respectively. Since these are only two free variables, it is also possible to plot the maximum side lobe level of the full transceiver chain versus X_t and X_r.

---

[2] Lenses perform wave-front processing in many optical systems.

Figure 5.4 shows the plot for the maximum side lobe level of a transceiver with an 8-element array on the transmitter side and an 8-element array on the receiver side achieving the minimum of −17.85 dB for $X_t = 2\lambda$ and $X_r = 2.75\lambda$. Figure 5.5 shows the same plot for a 16-element arrays on both transmitter and receiver sides achieving minimum side lobe level of −24.3 dB for $X_t = 2.9\lambda$ and $X_r = 2\lambda$[3]. In these plots, a minimum of 2λ element spacing is assumed considering the typical size of the nano-photonic antennas.

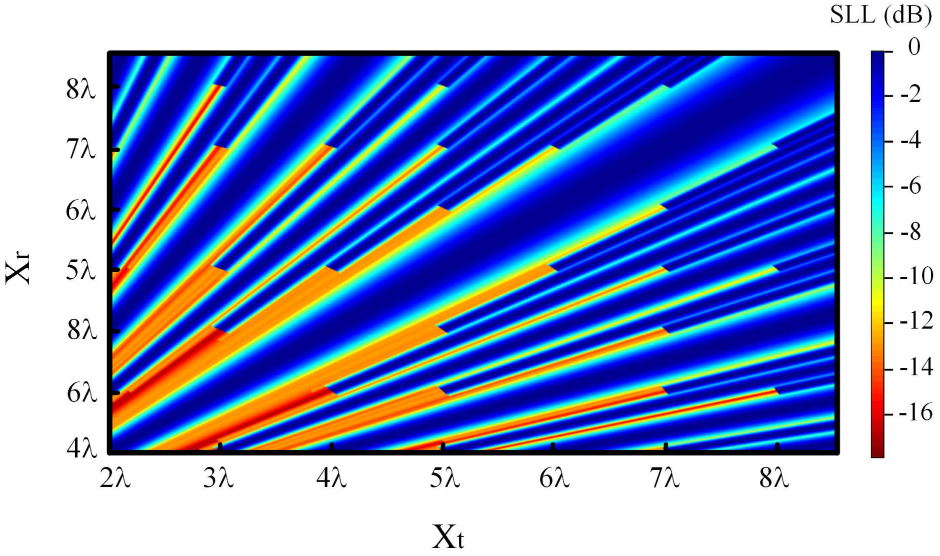

Figure 5.4: Side lobe level of the transceiver with an 8-element array transmitter and an 8-element array receiver with minimum side lobe level of −17.85 dB .

It should be noted that in equation (5.10) an infinite aperture is assumed for the receiver. To understand the effect of the limited aperture, the receiver can be modeled as an OPA receiver. Since the receiver element spacing is larger than $\lambda/2$, its array pattern has several grating lobes. However, for a large receiver aperture, if the receiver pattern is steered across the FOV, maximum of one receiver beam overlaps with one transmitter beam at each steering angle, Fig. 5.7. Therefore, the signal reflected from each illuminated point can be captured by the receiver when the other points are filtered by the array pattern and steering the beam collects all the information. However, the finite aperture size (and thus beamwidth) of the transmitter and receiver leads to an averaging effect for the neighboring points of the main beam direction. To consider this effect and also achieve a faster optimization/sweep

---

[3] If element spacings are limited to only integer multiples of $\lambda/2$, then the non-overlapping condition is met only if the integer coefficients are co-prime with respect to each other, leading to a co-prime sampling technique [132], [133].

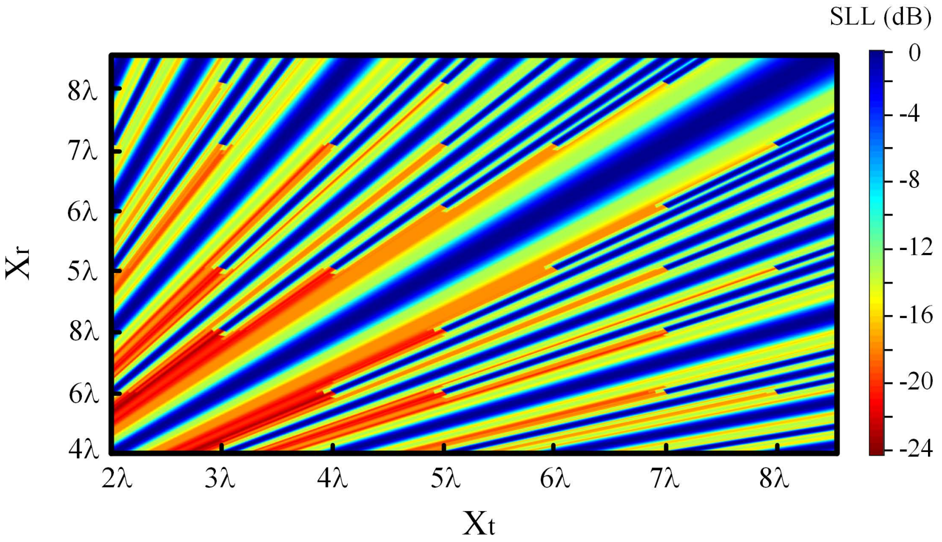

Figure 5.5: Side lobe level of the transceiver with an 16-element array transmitter and an 16-element array receiver with minimum side lobe level of −24.3 dB .

algorithm, the patterns of the transmitter and the receiver can be multiplied to get the full transceiver pattern.

Figure 5.6 shows the transceiver design with 2-element arrays on the transmitter and receiver apertures. The beam patterns of the two aperture are wide and have a considerable overlap that leads to large transceiver pattern side lobes. Increasing the number of elements, Fig. 5.7, reduces the beamwidth and thus higher isolation between information of the beams. Since the element spacing is defined by the maximum side lobe level, to further reduce the overlap and account for angle tuning inaccuracies, larger element count can be used and the optimization should be repeated. Since efficient power splitters are in the form of binary trees, the practical element counts are integer powers of 2.

5.4 Transmitter design

While the nano-photonic transceiver architecture, explained in the previous section, can be implemented with both 1D and 2D array apertures, the proof-of-concept system here is designed for a 1D aperture to avoid routing complexities of the 2D arrays and achieve higher resolution for a given number of elements. Moreover, a 1D-FOV antenna has the benefit of higher radiation efficiency in the transmitter setting, and larger effective area in the receiver setting compared to a 2D-FOV antenna on the same platform (see Chapter 6). The designed antenna here, Fig.

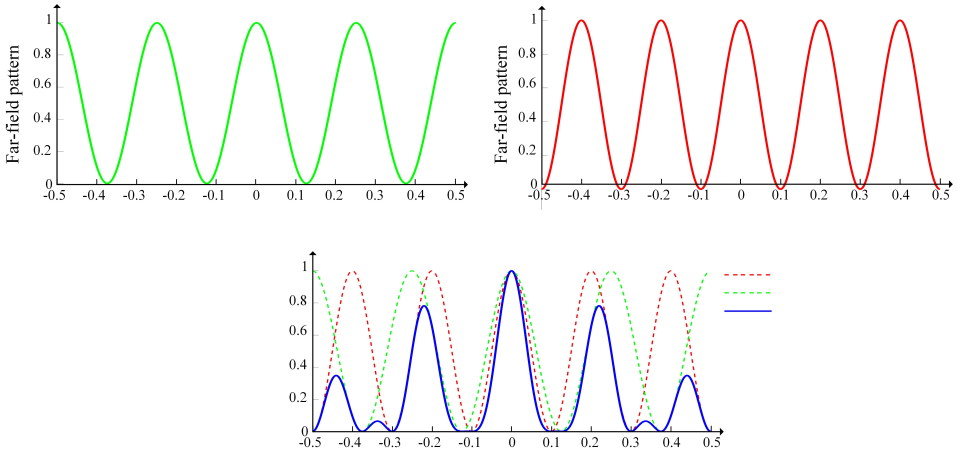

Figure 5.6: A transceiver with 2-element arrays on both transmitter and receiver sides (a) Transmitter pattern (b) Receiver pattern (c) Transceiver pattern which is the product of the transmitter and receiver patterns.

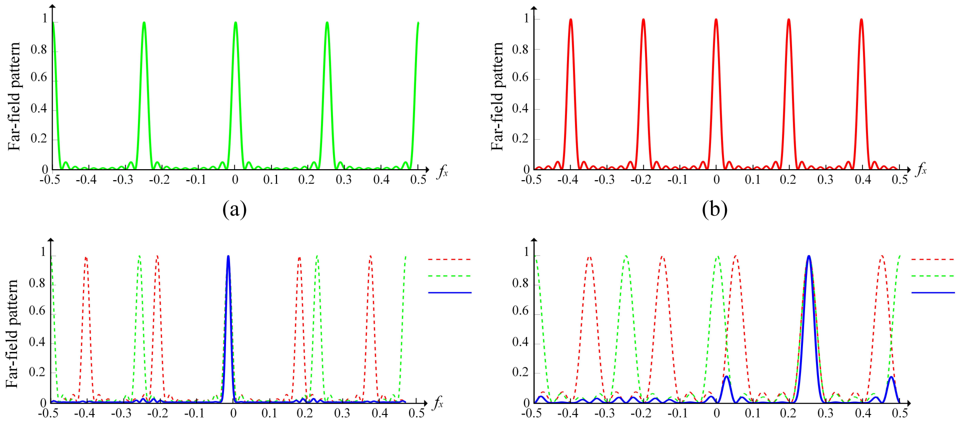

(a) (b) (c) (d)

Figure 5.7: A transceiver with 8-element arrays on both transmitter and receiver sides (a) Transmitter pattern (b) Receiver pattern (c) Transceiver pattern which is the product of the transmitter and receiver patterns.

5.8(a), has 1.5 µm-wide silicon gratings encompassed by a 2.5 µm-wide piece of 90 nm-thick silicon slab. The 1.5 µm grating width yields a 60° FOV along θ_y and the slab facilitates a longer propagation distance for the wave on the antenna structure, and thus a more uniformly distributed electric field pattern. The electric field intensity is desired to be relatively uniform on the antenna aperture to achieve a narrow beamwidth along θ_x. The width of the antenna pattern in θ_x direction determines the system resolution in this direction. Therefore, the antenna is 150 µm long to achieve a narrow beamwidth as well as high radiation efficiency. Since the width of the routing waveguide is 0.5 µm, a mode converter is designed to match the input feed to the antenna. The grating duty-cycle is optimized to achieve the maximum radiation efficiency at 1.550 nm wavelength. The achieved radiation efficiency for the antenna is 60% and its far-field radiation pattern is shown in Fig. 5.8(b).

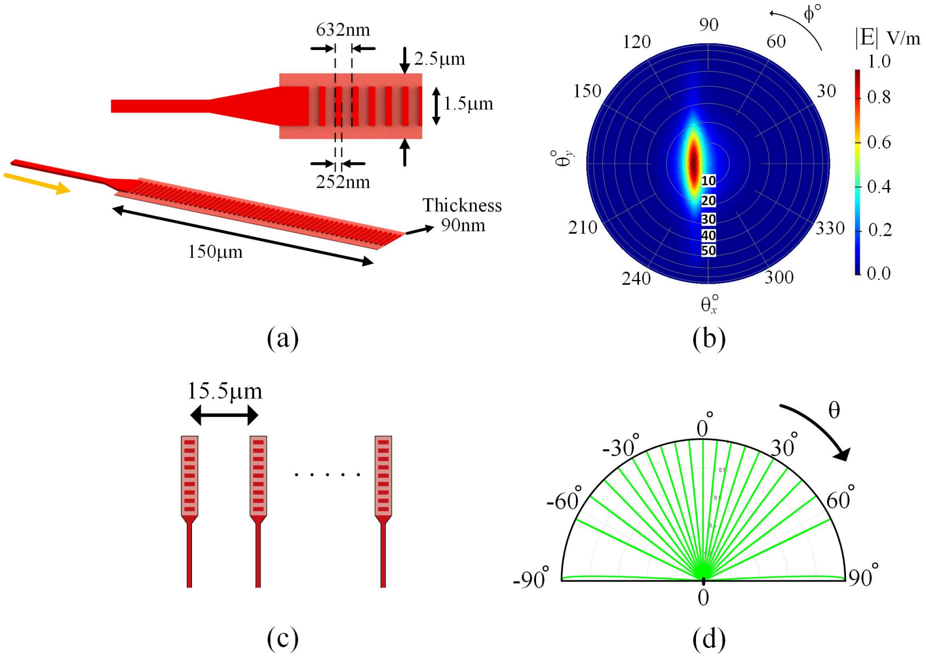

(a) (b)

(c) (d)

Figure 5.8: (a) Schematic of the nano-photonic antenna with a 1D FOV. (b) Far-field radiation pattern of the antenna (c) The antennas are placed on a 1D array with d=15.5 µm=20λ/2 element spacing. (d) Array pattern with 21 total beams for which 10 beams fall inside the antenna FOV.

The aperture is formed by placing 128 antennas on a uniform 1D array with 15.5 µm element spacing (Fig. 5.8(c)). This spacing, which is equal to 10λ, is large enough to avoid any coupling between the antennas and their feeding waveguides, and results in 10 beams in the 60° FOV of the antenna along θ_y direction as shown in the array pattern of Fig. 5.8(d). The beamwidth of each of the lobes in the array pattern is 0.04° which translates to 1500 resolvable spots on the FOV. The radiation pattern of the antenna is designed for 150 µm and can be swept along θ_x by tuning the optical wavelength.

The optical feed to the antennas are processed by a network of phase shifters. As discussed in section 5.2, the phase shifter should feature low loss, high speed, and low power consumption characteristics. Moreover, the fabrication effort for implementing the phase shifter should be compatible to integrated silicon photonic platforms and maintain the low-cost feature of the process. To satisfy all these performance requirements, here, hybrid organic polymer phase shifter [134] is chosen for realizing the phase shifter. However, for initial verification and demonstration purposes, the design is compatible to function as a PiN phase shifter by default and polymer will be added through a post-processing. Figure 5.9 shows the structure of the phase shifter in which the phase shift is induced by the injected charge flowing from the positive node to the negative node. The insertion loss of the phase shifter is minimized by providing enough spacing between the doped regions and the optical mode. However, the PiN phase shifter introduces an average active insertion loss of 4 dB, suffers from phase shift dependent amplitude variation (due to the varying loss), and consumes a relatively high power. Introduction of polymer is a relatively easy post-processing step of pouring the material on the chip while the aperture and input optical port are covered. While a deep oxide etch is offered by the fabrication process and can be used to remove the silicon oxide above the phase shifters, in the primary design this oxide etching step is skipped to avoid any pollution of the photonic surface and to have a reliable characterization of the system with PiN phase shifters. Thus, the etching required for application of polymer will be performed in-house afterwards, polymer will be applied, and a sealing layer will be added to protect it from degradation. Poling the polymer can be done through the driving ports. When the post-processing steps are finalized, the phase shifter is a polymer-clad phase shifter that the electric field dependence of the waveguide clad changes its effective index and thus the phase shift experienced by light traveling inside is achieved.

The input light for this system is provided by an external laser source which can be modulated externally by an arbitrary signal for ranging such as a chirp or pulse sequence. The modulated light is then coupled into the transmitter through the input focusing grating coupler. A 7-layer binary power splitter is used to split the input

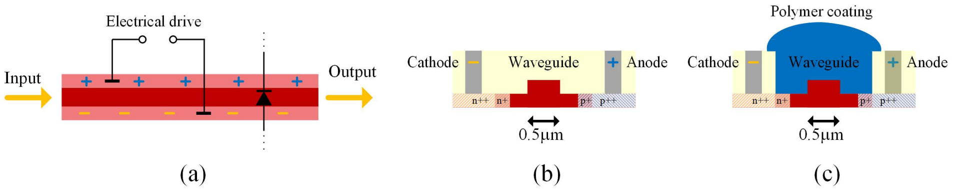

Figure 5.9: (a) PiN diode phase shifter compatible with a polymer phase shifter (b) Cross-section of the phase shifter operating in the PiN diode mode (c) Cross-section of the phase shifter after applying the polymer.

light into 128 equally powered branches which are then fed into the phase shifters. Each individual splitter is a compact symmetric Y-junction (Fig. 2.3) which has high robustness to fabrication mismatches and thermal variations on the chip.

To achieve high sidelobe rejection and precise beam steering directionality, the wavefront needs to be accurately controlled. Since there are several sources of non-ideality during the fabrication process that lead to random phase error for the antenna optical feeds, here, a phase measurement network is designed to measure the relative phase of the optical signals right before entering the antenna. The phase measurement network is shown in Fig. 5.10(a) in which a small fraction of propagating light in the neighboring optical feeds are sampled through a short-length coupler, and the two light samples combine with a Y-junction to interfere with each other. Therefore, the amplitude of the interference is then measured with a compact photodiode which yields a measure of the relative phase of the two sampled light. The collection of phase measurement results are used in a feedback loop to fine tune the optical phases.

Figure 5.10 shows the schematic of the transmitter and a die photo of the fabricated chip. The chip is fabricated in a standard single-photonic-layer low-cost silicon photonics process. Since the transmitter has only 128 elements the complexity of the electronic drive circuitry and photonic circuit is significantly reduced. Moreover, since most of the chip area is occupied by the phase shifters; having only 128 phase shifters yields a relatively small chip area of 3 mm by 3.7 mm and a low power consumption.

5.5 Receiver design

The receiver aperture is co-designed with the transmitter aperture in accordance with the double spectral sampling method explained earlier. The same long 1D-FOV antennas are used for the receiver as well since the transmitter and receiver

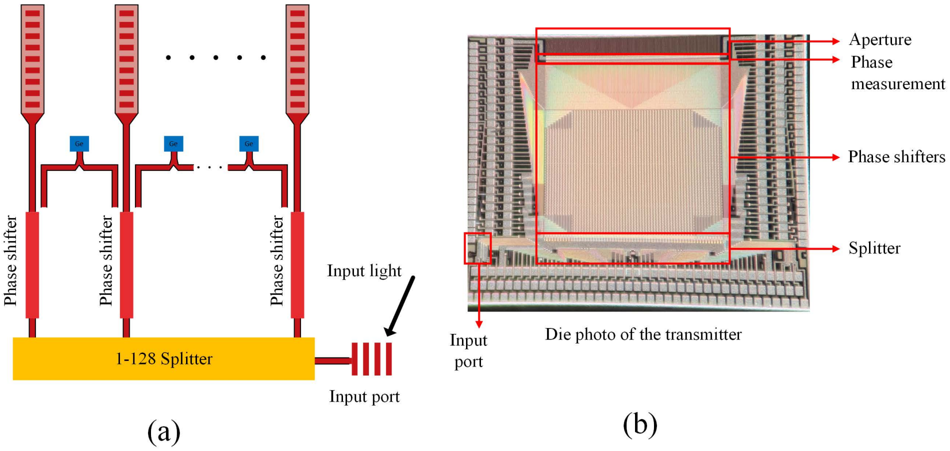

Figure 5.10: (a) Schematic of the transmitter architecture with relative phase readout for the neighboring antennas (b) Die photo of the fabricated chip.

patterns should be directed towards a same angle for a given wavelength. Moreover, the 1D-FOV antennas have much more relaxed FOV-effective aperture trade-off as discussed in Chapter 6 and have a relatively large effective area due to their long length. The designed antenna here, which is the same as the transmitter antenna, has a peak effective area of 26 μm^2 and the same normalized receiving pattern of Fig. 5.8(b) according to the reciprocity property explained in Chapter 6. The receiver aperture also has 128 elements which are spaced d=10.85 μm apart as shown in Fig. 5.11. Therefore, the total effective aperture of the receiver is 3328 μm^2.

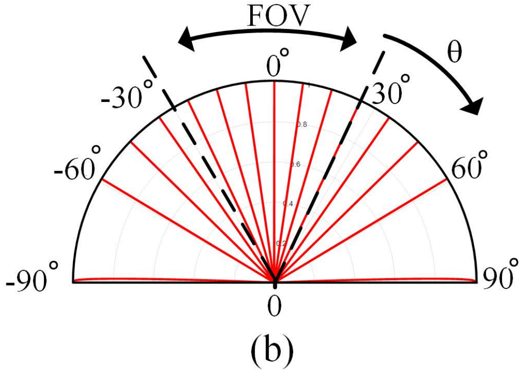

Figure 5.11: (a) The receiver antennas are placed on a 1D array with d=10.85 μm=20λ/2 element spacing. (b) Array pattern with 15 total beams for which 7 beams fall inside the antenna FOV.

To achieve high detection sensitivity, heterodyne detection is used to down-convert the received signals. The received signal by each antenna is routed into an optoelectronic mixer. The architecture of the mixers are similar to the mixers explained in Chapter 4.4, except they do not have a phase shifter in the reference path. Moreover, the reference signal is replica of the modulated transmitted signal with an IF frequency shift. Therefore, the mixer also performs a correlation between the transmitter and received signals as well as low-pass filtering the result and generating an output current at the electrical IF frequency while maintaining the optical phase and amplitude of the optical wave carrying the received signal. Opto-electronic correlation significantly relaxes the bandwidth requirements for the electronics. Therefore, while the spectral content of the received signal is correlated and down-converted and became and easier signal to process, the phases of the optical signals are preserved for later processing. The electrical signals are then amplified and digitized and the information of the illuminated points is extracted by an inverse Fourier transform performed in a DSP. The DSP processing is adjusted to detect interference and unwanted received signals and remove them through creating a notch at the corresponding angles. The output of this process yields the data regarding all the angles at once.

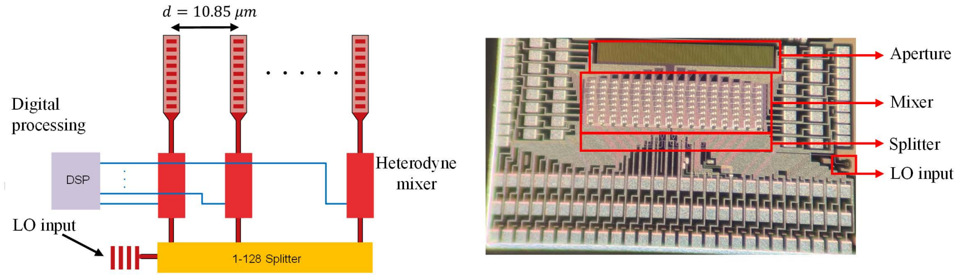

(a) (b)

Figure 5.12: (a) Schematic of the receiver architecture (b) Die photo of the receiver chip.

5.6 Conclusion

In this work, a transceiver architecture for high resolution 3D imaging is implemented. To overcome the challenges in of realization of a practical 3D imager on low cost integrated photonic platforms, a double spectral sampling method is devised that benefits from the advantages of both nano-photonic transmitter and receivers. This architecture features low power consumption, small chip area, and relatively low complexity of the photonic circuits.

Chapter 6

BREAKING FOV-APERTURE TRADE-OFF WITH MULTI-MODE NANO-PHOTONIC ANTENNAS

[1] R. Fatemi, P.Khial, A. Khachaturian, and A. Hajimiri, “Breaking fov-aperture trade-off with multi-mode nano-photonic antennas,” *IEEE Journal of Selected Topics in Quantum Electronics*, 2021.

In this chapter, novel nano-photonic antenna structures to break the fundamental trade-off between antenna FOV and effective aperture are investigated. First, the fundamental electromagnetic limits, as well as the constraints enforced by standard silicon photonics platforms on improving antenna FOV and effective aperture, are discussed. The approximated performance upper limits are derived and quantified. By revisiting and deviating from the conventional assumptions leading to these constraints, high-performance multi-mode antenna structures are demonstrated that achieve performance characteristics beyond the conventionally perceived limits. Finally, dense receiving arrays with pillar multi-mode antenna are discussed, an antenna array with more than 95% collection efficiency and 170° FOV is demonstrated, and the operation of a coherent receiving system utilizing such an antenna array aperture is presented[1].

6.1 Introduction

Nano-photonic antennas are a class of nano-structures on photonic platforms that shape the optical wavefront [35]–[41] or interface an integrated active flat optic system with free-space [20], [23], [43]–[45], [135]. The wavefront shaping antennas, usually realized as metasurface structures, capture the incident light and radiate back into the free-space. These antennas enable the nano-scale control of the wavefront by adjusting its local amplitude, phase, and polarization and found applications in lenses [37], lasers [38], spectroscopy and nano-imaging [39], light emitters in LEDs [40], polarization control devices [41], etc. In these devices, an array of dielectric/metal optical antennas are periodically patterned which are excited by an incident wavefront and radiate a secondary wave.

---

[1] The work presented in this chapter was done in collaboration with Aroutin Khachaturian.

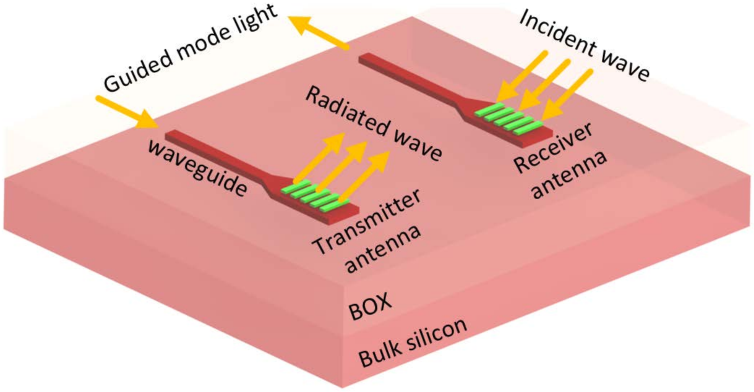

Figure 6.1: Schematic of a standard SOI silicon photonics platform consisting a bulk silicon substrate and a buried oxide layer (BOX). Optical components including transmit/receive photonic antennas are fabricated by patterning the silicon layer on the BOX.

A second type of nano-photonic antennas has emerged recently by the advent of integrated active flat optic systems. In this context, an antenna is defined as a transducer that couples the guided mode into the free-space mode and vice versa [20], which is the same definition used for conventional microwave antennas. In other words, an antenna is an on-chip component that in the transmitter setting is fed with a guided mode and radiates into the free-space, and in the receiver setting, captures the free-space incident wave and couples it into a waveguide (Fig. 6.1). Nano-photonic antennas have application in many recently demonstrated integrated photonic systems such as optical phased array transmitters [20], [43], [44], [56], [136], [137] and receivers [23], [26], nano-photonic coherent imager [45], wireless optical communication [138], lens-less cameras [25], etc.

In the early implementations of integrated photonic systems, conventional grating couplers were used as transmitter antennas [43]–[46], [138]. However, the large footprint of a grating coupler is a limiting factor in many systems such as dense antenna arrays. Moreover, the need to selectively/collectively improve specifications of the antennas such as FOV, radiation efficiency, and form factor has recently motivated the researchers to devise novel antenna topologies with improved performance. Deviating from grating structures allowed to achieve higher radiation efficiency [20]. Moreover, an ultra-compact broadband antenna is realized via optimization of the silicon slab etching pattern [136]. In addition to devising novel antenna structures on a single photonic layer process, by adding a high contrast grating on top of the antenna structure [139] and bottom reflectors [135], [140] the radiation efficiency of the antenna is improved significantly. However, most of these works are limited to 1D FOV antennas and have large footprints.

In addition to the transmitter antenna, a photonic receiver system [23], [25], [26], [45] also incorporates antennas that collect the incident power and output to waveguides. The waveguides are then used to route the optical signals for further processing. Since the received signal is weak in many applications, for a given physical size of the antenna, the largest effective aperture is desired to maximize the signal-to-noise ratio, sensitivity of the system, and robustness to the noise. While techniques such as heterodyne detection [23] can be used to increase the sensitivity of the system, a larger collection area is always beneficial to a receiver system and allows for operating at lower received signal levels and noisier environments. Moreover, the FOV of the antenna needs to be in harmony with the FOV of the system. A limited antenna FOV directly affects the performance of the system. For instance, in an optical phased array, small antenna FOV translates to a limited steering range. Conventional photonic antenna structures impose a compromise between FOV and effective aperture, i.e., a standard antenna with a large effective aperture is limited in the angular range that it can operate and vice versa.

6.2 Receiving photonic antenna

A single-port receiving antenna couples the impinging light into a guided mode within an on-chip planar waveguide. Its effective aperture is defined as

$$A(\theta, \phi) = P_o / S_i, \tag{6.1}$$

where P_o is the total power coupled into the waveguide attached to the antenna port and S_i is the power density (defined by Poynting vector) of a plane wave arriving from the direction defined by (θ, ϕ), assuming they are polarization matched. If the polarization state of the incident light, on the Poincare sphere representation, deviates from the polarization that results in the maximum power collection by an angle ψ, a polarization matching factor of $\cos(\psi/2)$ must be added to the above equation [122], which can reduce the effective aperture (down to zero) for a mismatched polarization. Hence, the ability to couple into both polarizations is a desirable feature of any design. Whenever, there is need for high signal strength and large signal-to-noise ratio (almost always), a high effective aperture is desirable. Effective aperture as a function of θ and ϕ defines the receiving pattern of the antenna. For any given application, a minimum FOV must be achieved, while maximizing the collection area.

Increasing the effective aperture faces limitations in different applications. For instance, in an optical phased array, if the individual element antenna size is increased to collect more power, the element spacing needs to be increased accordingly to fit the antennas. Increasing the element spacing reduces the grating lobe spacing in the array pattern, which can limit the effective grating-lobe-free beam steering range (FOV) of the optical phased array [20]. Moreover, by conservation of energy the effective aperture of each antenna in a large array cannot exceed the unit grid area, defined by the array pitch. If an array is made of individual elements whose standalone effective aperture exceeds this limit, the effective aperture within the array will reduced through the coupling with adjacent elements.

On the other hand, in the transmitter setting, it is desired to maximize the radiation efficiency of the antenna which is defined as the ratio of the total power radiated by an antenna to the net power fed into it[2]. The radiated power is desired to be distributed on a certain angular range or FOV which is a property of the antenna pattern. Antenna pattern or directivity pattern, $D(\theta, \phi)$, is a function of elevation angle, θ, and azimuth angle, ϕ, and characterizes the relative power density in each direction to the average power density radiated by the antenna[3].

There is a well-known antenna reciprocity relationship between the receive and transmit patterns of a single-port antenna that imposes a trade-off between its FOV and effective aperture. We will present a short derivation of this reciprocity and use the setting in the subsequent sections for additional discussions of the FOV and effective aperture trade-offs.

Consider the setting of Fig. 6.2, with the antenna under test (AUT) and a measurement antenna (MA) at a very large distance R at (θ, ϕ) (shown at two different locations in the figure). The MA is polarization matched to the AUT. Both antennas have a single-mode port. Thus, a two-port network model with a scattering matrix of **S** is sufficient to analytically represent the system. The parameters of the scattering matrix depend on the location of the MA and are functions of (θ, ϕ). When AUT is in the transmit mode, the antenna pattern (directivity) of AUT can be measured by sweeping MA over (θ, ϕ). The power transfer from AUT to MA is given by $|s_{21}(\theta, \phi)|^2$ at each (θ, ϕ). Therefore, the directivity of the antenna is proportional

---

[2] In some literature, port mismatch is not included in the radiation efficiency and the net power accepted by the antenna is considered.

[3] The field pattern of the antenna quantifies the magnitude of the field instead of power and thus is the square root of the power pattern.

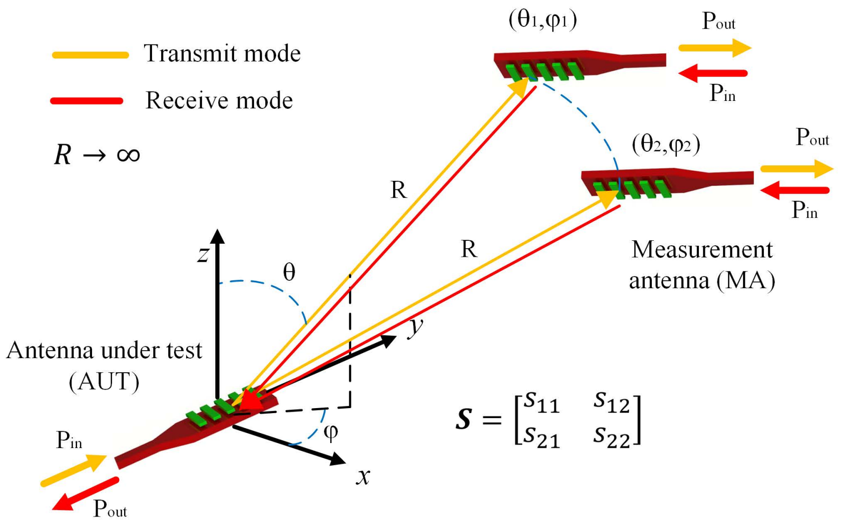

Figure 6.2: Antenna setting for deriving radiation pattern in the transmit mode and effective aperture pattern in the receive mode. Radiation pattern, $D(\theta, \phi)$, and receiving pattern, $A(\theta, \phi)$, of an antenna in a reciprocal medium are linearly related.

to

$$D(\theta, \phi) \propto |\frac{s_{21}(\theta, \phi)}{s_{21}(\theta_1, \phi_1)}|^2, \tag{6.2}$$

in which (θ_1, ϕ_1) are the reference angles. Conversely, with AUT in the receive mode, the MA radiates power and the AUT receives it. Now, the power transfer from MA to AUT is given by $|s_{12}(\theta, \phi)|^2$. The effective aperture pattern (receive pattern) $A_{eff}(\theta, \phi)$ is proportional to

$$A_{eff}(\theta, \phi) \propto |\frac{s_{12}(\theta, \phi)}{s_{12}(\theta_1, \phi_1)}|^2. \tag{6.3}$$

In a reciprocal medium, the scattering matrix is symmetric, i.e. $s_{12} = s_{21}$ [57]. Therefore, the directivity pattern in the transmit mode and effective aperture pattern in the receive mode are linearly related as

$$A_{eff}(\theta, \phi) \propto D(\theta, \phi). \tag{6.4}$$

Hence, the well-known relation between directivity and effective aperture for a single-port antenna that can be obtained by calculating the effective aperture and directivity pattern of an arbitrary antenna which yields [6]

$$A_{eff}(\theta, \phi) = \frac{\lambda^2}{4\pi} D(\theta, \phi), \tag{6.5}$$

in which λ is the wavelength of the electromagnetic wave. In other words, the normalized radiation pattern of the antenna in the transmit mode and its effective aperture pattern in the receive mode are the same. Therefore, a single-port antenna that has a good performance in sending the wave towards a certain direction is also a good antenna for collecting the light impinging from the same direction.

6.3 Fabrication imposed limitations

Aside from the fundamental trade-offs in designing a nano-photonic antenna (discussed in the next section), the single photonic layer platforms, offered by many low-cost silicon photonic foundries, impose further limitations on adjusting and improving the effective aperture and FOV of the antenna. Therefore, in this section, we study the performance parameters of nano-photonic antennas and discuss the limitations of a general form antenna in a silicon photonic platform. Moreover, potential antenna structures to push the performance to conventional fundamental limits are demonstrated. Since the radiation pattern and effective aperture pattern are linearly related, equation (6.5), maximizing antenna's radiation efficiency and directivity yields the maximum effective receiving aperture as well. However, since investigating antenna characteristics in the transmitter setting is more illustrative, the following discussion is examined from the transmitter point of view.

Since dielectric antennas can be safely approximated as lossless, low reflection at the input port of the antenna results in high antenna efficiency. Therefore, the input port of the antenna structure should provide an acceptable matching[4] to maximize the radiated power by the antenna in the transmit mode and correspondingly, its effective aperture in the receive mode. In addition to coupling the input power to the antenna efficiently, its radiation pattern should be adjusted. Antenna pattern or far-field radiation pattern, Fig. 6.3(a), is the same as its aperture Fraunhofer diffraction pattern. In other words, the antenna field pattern is the Fourier transform of the field distribution on the antenna aperture [7]. FOV of an antenna is an angular range on the antenna pattern with a power density higher than a specific threshold (usually considered -3 dB lower than the maximum). Since antenna radiation pattern and effective aperture pattern are linearly related, FOV of the antenna in the transmitter and receiver settings are the same. To derive the relationship between the antenna geometry and FOV, the electric field distribution of the aperture can be thought of an electric field distribution $E(x, y)$ multiplied by an aperture function $A(x, y)$. Therefore, the far-field field pattern is the convolution of the Fourier transforms of

---

[4] S_{11} of less than -20 dB is considered acceptable in many situations [57]

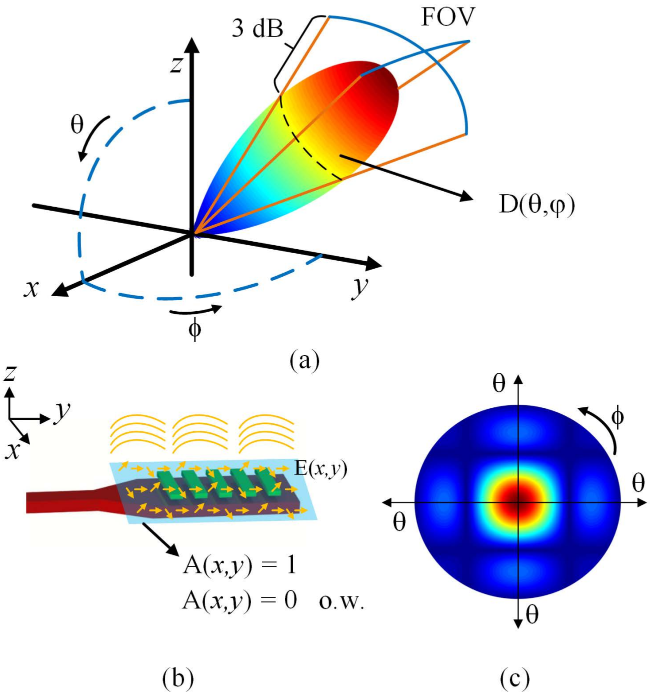

Figure 6.3: (a) Radiation pattern of a transmitter antenna with −3 dB range FOV (b) Conceptual schematic of the aperture electric field distribution, $E(x, y)$, windowed by the aperture function, $A(x, y)$ (c) *sinc* function far-field pattern of the aperture windowing effect which is equivalent to windowing a plane wave traveling in the z direction.

$E(x, y)$ and $A(x, y)$. Since for a smaller aperture size $A(x, y)$ has a wider Fourier transform, it is expected that a smaller antenna size yields larger FOV and a larger antenna size with a larger aperture results in a more directive far-field pattern and narrower FOV.

While this is a simplified but effective relationship between the antenna size and its FOV, the size of the antenna does not yield any information about the specific angular range that the radiated power is directed to. The shape of the antenna pattern depends on the E-field distribution on the antenna aperture. If the aperture window function is approximated with a rectangular function, a uniform electric field distribution on the aperture (which is the case for a windowed plane wave traveling in the positive z direction in Fig. 6.3(b)) yields a far-field pattern which is a *sinc* function centered at $\theta = 0$ (Fig. 6.3(c)). However, the direction of the guided mode is orthogonal to the z direction in integrated photonics. Therefore, a grating coupler, used as a conventional nano-photonic antennas, embeds a periodic structure inside the antenna aperture that modulates the spatial frequency of the electric field and adjusts the far-field pattern direction of the antenna by shifting the Fourier spectral content (far-field pattern) by the spatial modulation frequency. However, since the antenna is fed from one side, the field distribution might deviate from an ideal periodic pattern. While using a grating structure is a straight forward technique to achieve a distribution, other designs obtained by aperiodic and irregular apertures have also been demonstrated recently [20], [136], [141].

In a simple slab antenna, there is radiation from top and bottom of the aperture (positive and negative z), as in Fig. 6.4. With the silicon substrate underneath the antenna, the reflected wave from the interface changes both the aperture function, A(x,y), and distribution of the electric field, E(x,y). The reflection potentially has a wider field distribution and can interact with the neighboring structure and increase the mutual coupling between the antennas in an array. Moreover, the reflected light may travel in a different direction after interacting with the antenna structure again, affecting the antenna pattern. If part of the power radiates in undesired directions, it can cause unwanted peaks in the radiation pattern with undesirable effects. The light that passes through the bulk at the interface hits the bottom of the chip and reflects back, as illustrated in Fig. 6.4 in a simple ray-optics view. This reflection becomes more unpredictable if the interface is not very smooth and can lead to a random pattern, making it very difficult for the elements to produce a repeatable pattern that will limit the system functionality. Since transmit mode radiation pattern and receive mode effective aperture are linearly related, these effects disrupt the receiving functionality of the antenna as well. Therefore, it is desirable to design the antenna so that it couples the light maximally upward to achieve the best directivity and effective aperture, which presents its own challenges in a single-layer low-cost photonic process.

Consider a single layer photonics process that allows for 2D waveguide routing in addition to a few etching masks operating at a wavelength of 1.550 nm with waveguide dimension of 220 nm height and 500 nm width. Without additional etching mask, the only asymmetry in the antenna structure would be due to the silicon substrate at the bottom versus the air interface on the top. To obtain an estimate of the upper bound on the antenna performance in this setting, the reflection and transmittance from silicon oxide into silicon and air for normal angle can be simply calculated based on the Fresnel equations as

$$R_{o2a} = |\frac{n_{ox} - n_{air}}{n_{ox} + n_{air}}|^2 = 0.03, \; T_{o2a} = 0.97 \tag{6.6}$$

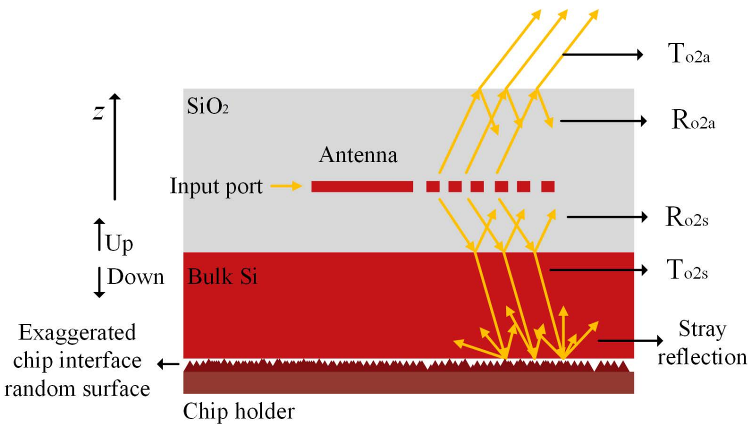

Figure 6.4: A conceptual side-view schematic of the transmitter antenna on a silicon photonic platform with bottom reflections from the Box-Bulk interface and the bottom of the chip.

$$R_{o2s} = \left|\frac{n_{si} - n_{ox}}{n_{si} + n_{ox}}\right|^2 = 0.16, \;\; T_{o2s} = 0.84 \tag{6.7}$$

in which n_{ox}=1.44, n_{si} = 3.4, n_{air} = 1 are the the refractive indices of silicon oxide, silicon, and air, respectively. If we assume that the reflected wave does not interfere considerably with the upward radiation of the antenna and ignore the secondary reflections inside the oxide slab, then for the best case the total light radiated upward is

$$T_{up} = (0.5 \times 0.97 + 0.16 \times 0.5 \times 0.97) = 56\%. \tag{6.8}$$

Constructive interference of the reflected wave and the upward radiating wave can improve the amount of power which will be radiated to the air. However, due to the widening of the reflected beam, the two beams do not overlap or interfere constructively for the most part. Therefore, the above derivation is a close approximation to the practical power efficiencies that are achievable. Even with additional etching levels, only a limited amount of vertical asymmetry can be achieved. For instance, an additional 110 nm etch into a 220 nm silicon slab is still less than $\lambda/4$ with λ being the wavelength of the light inside silicon, 455 nm. Therefore, the electromagnetic wave does not face an effective distinction between the two sides. Figure 6.5(a) & (b) show the best performance achieved by optimizing an antenna with 1D FOV in such a single-layer photonic process which leads to 60% upward radiated power.

The above derivation considers a long antenna structure (which results in a 1D FOV antenna[5]) assuming all the power being radiated upward or downward. To achieve

---

[5] Due to the long dimension of the antenna, and thus aperture function $A(x, y)$, in one direction,

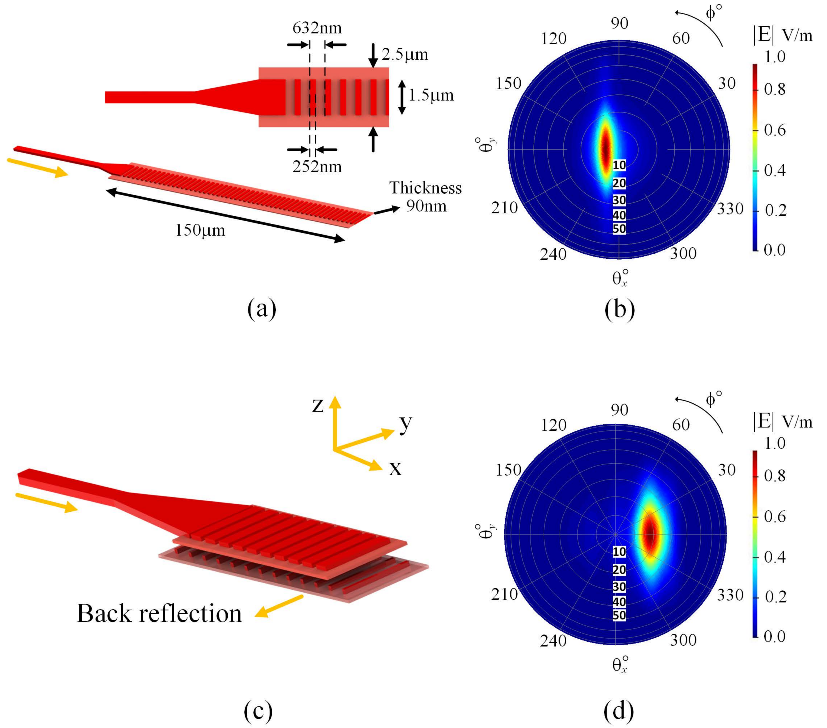

(a) (b) (c) (d)

Figure 6.5: (a)&(b) 1D FOV antenna with 60% upward radiation efficiency with its radiation pattern (c)&(d) Schematic of the 2D antenna with boosted asymmetry for improved performance and its radiation pattern achieving 80% upward radiation efficiecy.

a wide 2D FOV, both in-plane dimensions of the antenna should be relatively small (less than 6 μm). Due to the short length of the antenna structure, a fraction of the forward propagating guided wave continues to move forward and turns into stray light after interacting with other structures on the chip. Therefore, the radiation efficiency of a compact regular grating coupler with a 2D FOV is limited to approximately 33%.

A stronger asymmetry in the structure of the antenna is needed to improve the radiation efficiency. For example, a thicker than $\lambda/2$ silicon slab can achieve a higher asymmetry and thus more efficient upward radiation as shown in Fig. 6.6(a)&(b). Another approach to introduce asymmetry is adding extra dielectric layers in the fabrication process, Fig. 6.6(c) & (d). To demonstrate the potential improvement that can be achieved using a stronger asymmetry, we designed a compact 2D FOV antenna shown in Fig. 6.5(c) & (d). This design shows an example of vertical directivity enhancement to 80% utilizing a silicon back reflector layer.

---

its Fourier transform is narrow in the same direction, providing a 1D FOV.

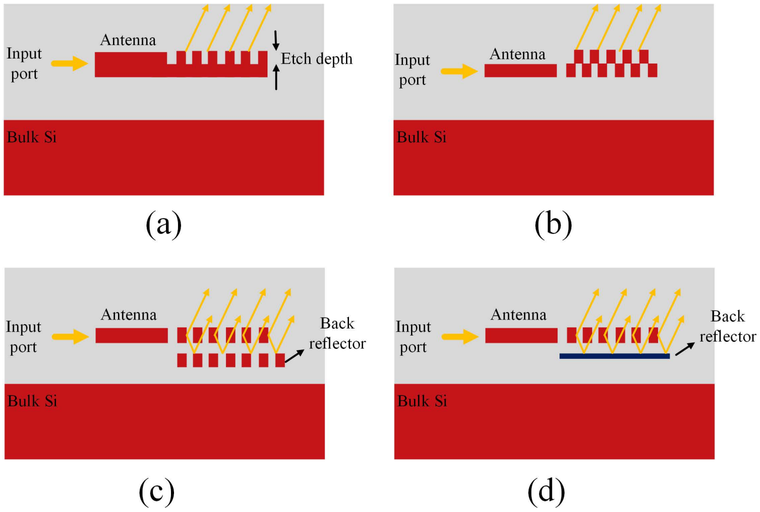

Figure 6.6: Various forms of increasing the asymmetry to improve radiation efficiency (a) using a thicker silicon layer (b) adding a specific silicon layer on the antenna (c) & (d) adding a bottom reflector.

There have been attempts in the past to design transmitter antennas with higher radiation efficiency which are limited to 1D FOV structures. In [139], a high-contrast grating structure is used to improve the performance and a radiation efficiency of 94% is reported at 1.550 nm wavelength. Moreover, antenna designs with an extra dielectric layer to obtain a controlled and improved reflection were demonstrated that achieve close to 90% radiation efficiency [135], [140], [142]. While the specific details of the approaches taken in these works are different, in principle the core idea is to introduce an asymmetry in the structure of the antenna to improve its radiation efficiency. Therefore, other techniques that can overcome some of these limitations by design without the need for additional dielectric layers would be highly desirable, as the added layers increase the fabrication cost and complexity.

6.4 Trade-off between effective aperture and FOV

As discussed earlier, designing a receiver antenna with a large effective aperture is desired in many applications to achieve a larger signal-to-noise ratio. Moreover, it is often desirable for the antenna to be able to collect light from a large FOV, particularly if beam-steering is desirable. However, designing an antenna with both large effective aperture and FOV faces some fundamental limits in a reciprocal system, which is the case for standard materials used in silicon photonic processes. Next, we briefly review this limit using an idealized model and then discuss its implications leading to additional design insights.

For the idealized model, we assume that the radiated power is distributed uniformly on a solid angle Ω bounded by $\theta < \theta_{FOV}$, as shown in Fig. 6.7(a). Since power is only radiated within Ω (instead of the full sphere of 4π solid angle), directivity increases by a factor of $4\pi/\Omega$ within Ω compared to an isotropic radiator (uniform directivity of 1) and is zero outside. Therefore, the directivity pattern is calculated as

$$\Omega = \int_0^{2\pi} d\phi \int_0^{\theta_{FOV}} \sin(\theta) d\theta = 4\pi \sin^2\left(\frac{\theta_{FOV}}{2}\right) \tag{6.9}$$

$$D(\theta, \phi) = \frac{4\pi}{\Omega} = \csc^2\left(\frac{\theta_{FOV}}{2}\right), \tag{6.10}$$

which in combination with (6.5) leads to an effective aperture of

$$A_{eff} = \left(\frac{\lambda}{\sqrt{\Omega}}\right)^2 = \left(\frac{\csc(\frac{\theta_{FOV}}{2})}{2\sqrt{\pi}}\lambda\right)^2 = \left(\eta\lambda\right)^2, \tag{6.11}$$

where η is the effective aperture normalized by wavelength squared. (*e.g.*, $\eta = 1$ corresponds to an effective aperture of λ^2.) Figure 6.7(b) shows η versus the FOV of the antenna. For $\eta = 1$, θ_{FOV} is 32.8° corresponding to a FOV of 65.6°. If the radiation pattern has the ideal conical shape similar to Fig. 6.7 but not centered at $\theta = 0$, the derivation yields the same result for the same solid angle value of Ω. A larger η (larger effective aperture) comes at the cost of smaller FOV. This is the fundamental trade-off between the effective aperture and FOV of a single-port single-mode receiving antenna.

This idealized antenna pattern is a useful, yet practically unrealizable abstraction. The inverse Fourier transform of the pattern that corresponds to the electric field distribution on the surface of the antenna aperture has infinite area due to the brick-wall drop of the radiation pattern, making it unrealizable exactly due to the finite dimensions of any physical antenna. Any finite size antenna will have side lobes outside the primary radiation beam and will not have perfectly uniform radiation pattern within the FOV, often defined by the full-width-half-maximum beam width (3 dB drop). The added power outside the FOV further reduces the average directivity within the FOV. This leads to an average effective aperture in the FOV smaller than the ideal model of Fig. 6.7(a), while the non-uniformity of the effective aperture can lead to a larger effective aperture at the peak of the pattern. Any sidelobe or stray radiation outside of the FOV reduces the directivity and thus the effective aperture inside the FOV, highlighting the need for a well-designed radiation pattern.

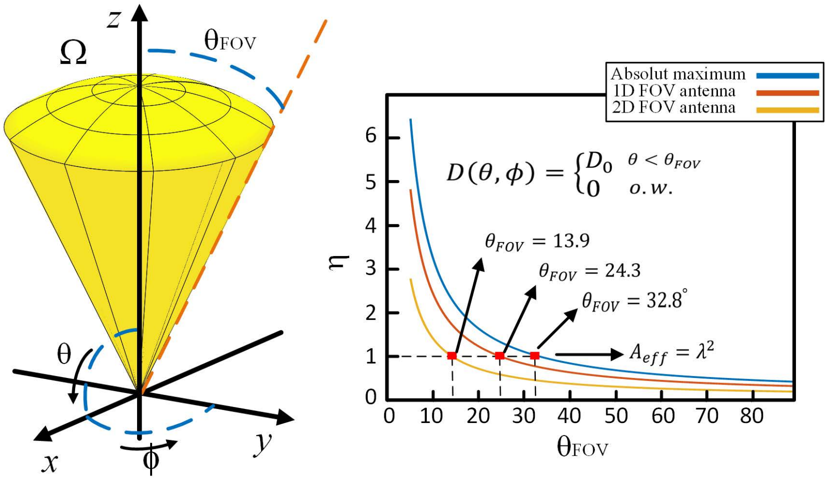

Figure 6.7: (a) Idealized directivity pattern with FOV of $\theta = 2 \times \theta_{FOV}$ (b) η factor versus θ_{FOV} that shows for an effective aperture of λ^2, the maximum achievable FOV is $\theta_{FOV} = 32.8°$, FOV achievable for 1D antennas in low-cost silicon photonics processes is $\theta_{FOV} = 24.3°$ and FOV achievable for 2D antennas in low-cost silicon photonics processes is $\theta_{FOV} = 13.9°$.

In light of the relationship of equation (6.5), the discussion about the physical size of the transmitter antenna and its FOV in section 6.3 can be extended to the receive mode. For the transmitter antennas, increasing the physical size of the antenna leads to a smaller FOV due to the Fourier transform's scaling property. The equivalent of this statement in the receive mode is that a larger physical size can increase the effective aperture and the collected power at the cost of a smaller FOV. Therefore, in designing a single-port single-mode receiver antenna, if the effective aperture is increased by increasing the physical size of the antenna, the angular range that the antenna can collect power from decreases accordingly.

6.5 Designing antennas beyond conventional performance limits

An antenna performance beyond conventional limits could only be achieved by overcoming the trade-off between FOV and effective aperture that was derived in (6.5). This would only be possible by violating the assumptions leading to (6.5). The single-mode antenna port assumption for the configuration of Fig. 6.2 resulted in the two-port network model, which forms the foundation of our derivation. Extending the antenna structure to support multi-mode guided waves may open a path for designing antennas with performance metrics beyond the conventional limits. To capture the effect of the extra modes of the antennas in the scattering matrix model, a new row and column should be added for every extra mode on each antenna. Following the same procedure in section 6.2, it can be shown that for a reciprocal medium, the relationship of equation (6.5) still holds for every pair of transmitter-receiver modes, individually. However, the contribution of different modes *collectively* can yield larger effective aperture and FOV, simultaneously. In other word, adding a second mode to the antenna could in theory upto double the FOV (in solid angle) with the same effective aperture. Alternatively, it could upto double the effective aperture with the same FOV, or increase both FOV and effective aperture partially. Increasing the number of modes supported by the antenna relaxes the trade-off with the same trend by each mode bringing its share of FOV and effective aperture. It is worth noting that dual polarization grating couplers investigated in the literature [143]–[145] are a small subset of multi-mode antenna structures. In these couplers, the two orthogonal incident polarizations are captured by the two antenna modes and coupled into the super-modes formed by two single mode waveguides. While the peak value of the effective aperture is not increased, it is extended to cover the whole polarization state space uniformly rather than having a peak at a single polarization and dropping to zero for the corresponding orthogonal polarization. As a side note, another assumption leading to (6.5) is the reciprocity of the medium, which can potentially be broken by incorporating non-reciprocal materials in the antenna structure. While an interesting topic for further research, we will focus on the multi-mode antennas in the rest of this manuscript due to the current integration challenges and loss properties of non-reciprocal materials.

It should be noted that in a reciprocal medium, the power collected and coupled to multiple modes can not be totally combined into a single mode and carried by a single mode waveguide, as that entire system would be tantamount to a single-mode single-port antenna. It is possible to combine the power of multiple modes into a single mode if the phases of the input modes are defined or controlled [146]. However, in the case of the multi-mode antenna, the relative phase of the excited modes changes versus incident angle and rules out this possibility. In other words, such a power combiner cannot be lossless or it will not have matched ports that causes power reflection at the ports, Fig. 6.8(b) & (c). This fact can be easily understood by changing the boundaries of the network and including the combiner inside the system, which yields an antenna with a single mode port and leads to the limitations discussed. Therefore, the collected power should either be transferred using a multi-mode waveguide or should be down-converted by photodetectors first and then combined, Fig. 6.8(d) & (e). The non-linearity of the photo-detection

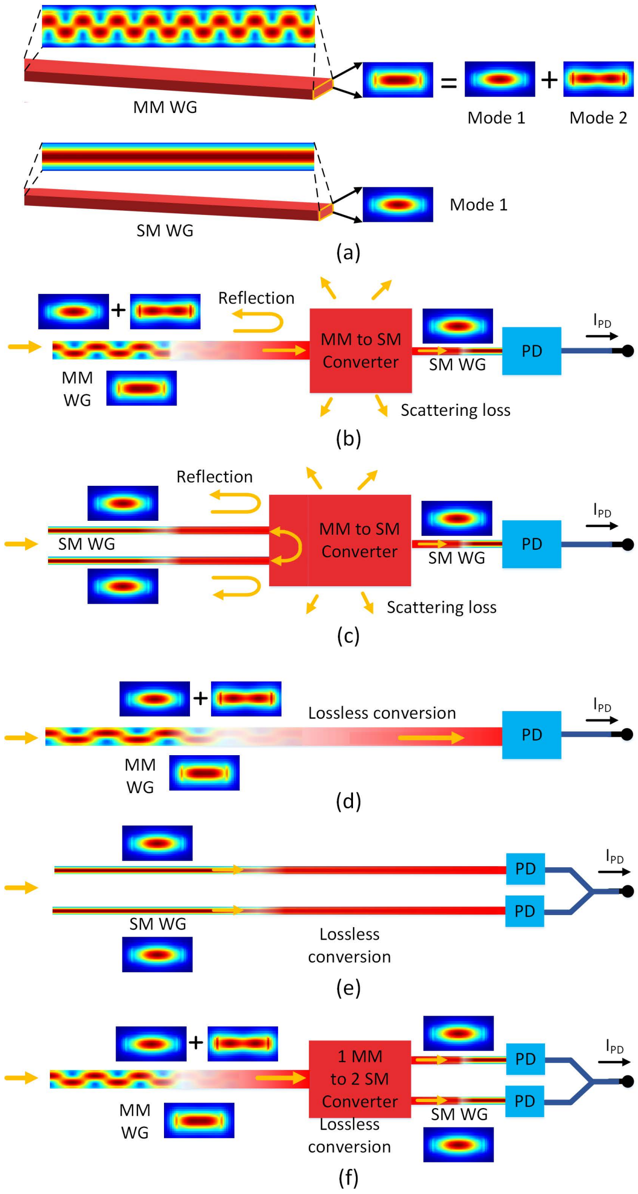

Figure 6.8: (a) Multi-mode and single-mode waveguides (b) The two modes carried by a multi-mode waveguide combined into a single mode. (c) Two super-modes supported by two single-mode waveguides combined into a single mode. (d) The power carried by a multi-mode waveguide input to a power detector that outputs the combined power. (e) The two super-modes of the structure are input to two power detectors and power combining happens after down-conversion to DC. (f) A multi-mode to multi-mode is used before feeding the power into the photodetector.

process breaks the assumptions in our derivations and invalidates the discussed constraints. While lossless conversion of multiple modes into a single mode is not possible, converting n modes carried by a structure into n or more modes supported

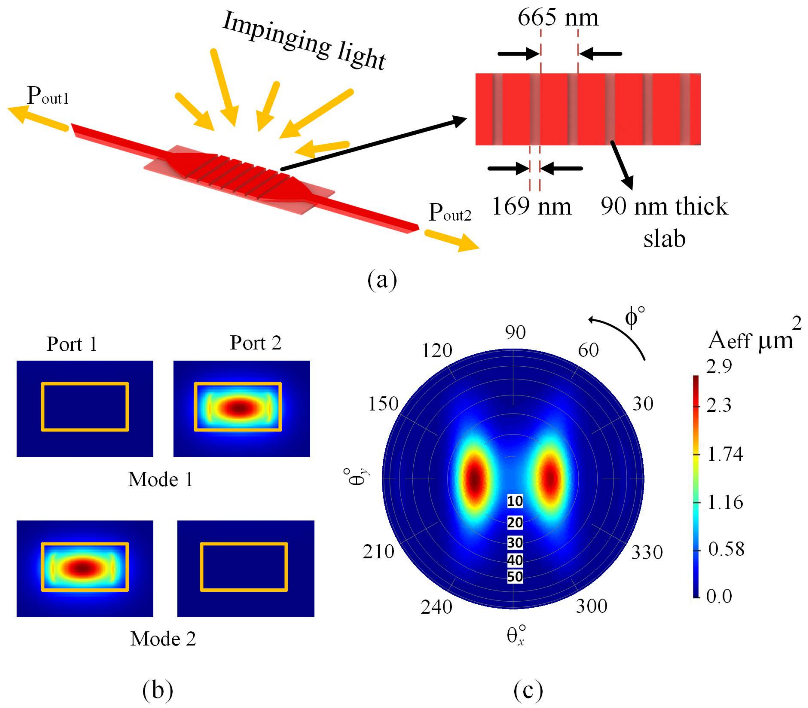

Figure 6.9: (a) Dual-mode antenna which uses two single mode waveguides to form two super-modes carrying the optical power output by the antenna (b) Cross-section of the supper-modes of the antenna propagating in the waveguides (c) Total FOV and effective aperture of the antenna versus azimuth and elevation angles.

by a different structure is possible. Examples of such mode converter structures are presented in [147]–[150] which convert the two modes of a multi-mode waveguide into two super-modes supported by two single-mode waveguides. Therefore, to improve the photodetection process multi-mode to multi-mode conversion can be used first (Fig. 6.8(f)).

There are various possible design option to extend the antenna structure for supporting more than one mode. A simple illustrative structure is the dual-port antenna of forms Fig. 6.9(a), where a super-mode is formed using two single-mode waveguides such that the field distribution of each waveguide is not disturbed. This is done by placing the two waveguides on the opposite sides of the antenna. The two states of the super-mode formed by the two waveguides are shown in Fig. 6.9(b) which can be approximated with the individual modes of the two waveguides with a high accuracy. To keep the design simple and the number of degrees of freedom small, a periodic grating of 6 silicon slabs is used to shape the field distribution on the antenna aperture. Since only two modes are assumed, the design spaces provided by

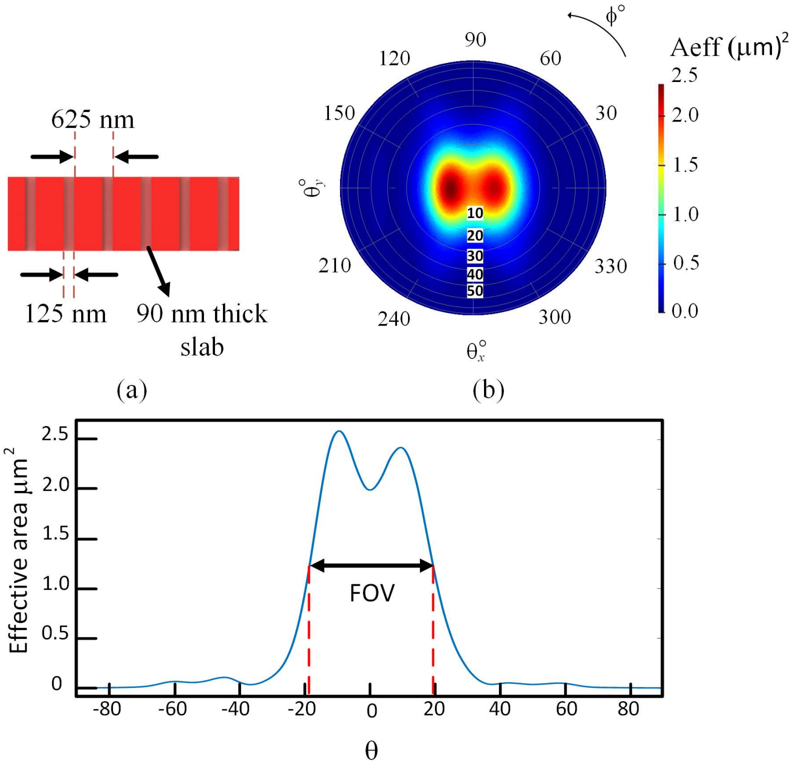

(a) (b)

(c)

Figure 6.10: (a) Design parameters of the dual-mode antenna with a monotonic FOV (b) Total FOV and effective aperture of the antenna versus azimuth, ϕ, and elevation, θ, angles (c) Effective area of the antenna versus θ for $\phi = 0$ which shows a 40° of FOV.

the grating structure is flexible enough to yield high radiation efficiency and effective aperture for both modes. To maximize the FOV, the FOV range of the two modes are designed to be separated, Fig. 6.9(c). Therefore, the FOV of the antenna is doubled compared to a single mode antenna of the same kind in a low-cost silicon photonics process. The grating period is 665 nm with 25% duty cycle. Moreover, an etched silicon slab facilitates the forward propagation of the field as well as providing a good matching at the input ports. This antenna achieves a peak effective area of $2.9\,\mu\text{m}^2$ with total FOV of 30° by 30°.

Separation of the FOV of the two modes maximizes the functional angular range of the antenna but results in a deep notch at 0°. Using the same structure, it is also possible to achieve a monotonic angular range for FOV and adjust the ripple of effective aperture/directivity inside the FOV range. Figure 6.10 shows a design with a single large angular range of FOV of 40° by 15° achieving effective area

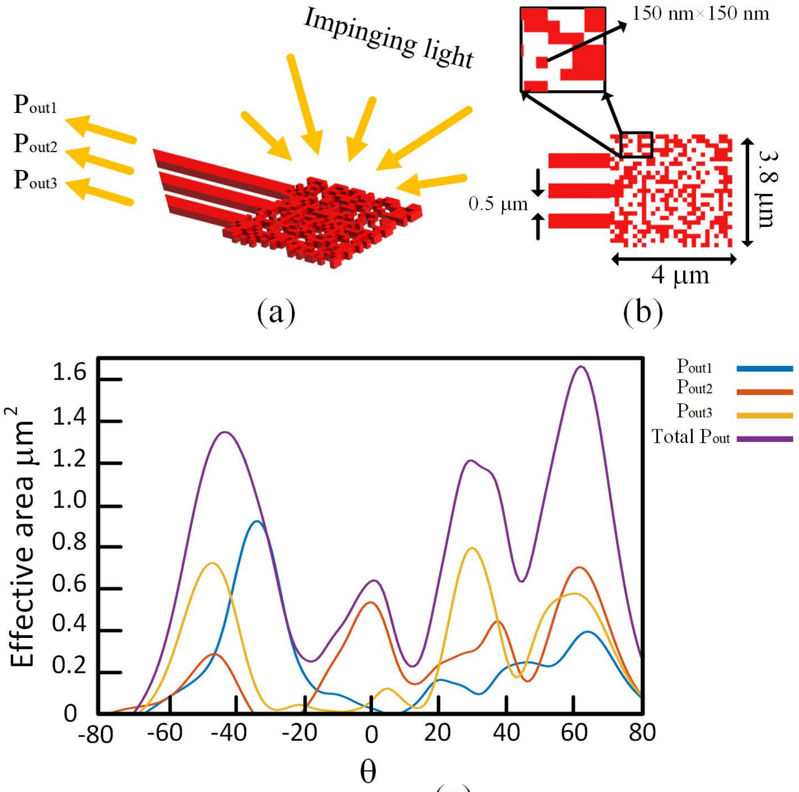

(a) (b)

(c)

Figure 6.11: (a) Schematic of the designed 3-mode antenna which uses three single mode waveguides to form the super-modes carrying the optical power output by the antenna(b) Design details of the antenna aperture formed by etching a binary pattern of 150 nm squares (c) Total effective aperture and individual effective aperture provided by each supported mode versus elevation angle.

of 2.5 µm^2. Since the FOV of the two modes overlap, the peak effective aperture regarding the total collected power by the two modes can be more than the design of Fig. 6.9. In other word, since the trade-off is relaxed by a factor of two in the 2-mode structures, if FOV is reduced the effective area inside the FOV will increase.

Extrapolating the methodology used for the dual-port antenna of Fig. 6.9 and Fig. 6.10, an example of a 3-mode antenna is shown in Fig. 6.11(a). It constructs super-modes using three single-mode waveguides with 0.5 µm gaps between them to increase the product of FOV and effective aperture. The three waveguides collectively support the three modes of the antenna port, as shown in Fig. 6.11. For adjusting the electric field distribution on the antenna aperture, a standard grating structure has a limited design space in this case and cannot be used to achieve a good performance over a broad range of angles. Therefore, we adopted a patterned

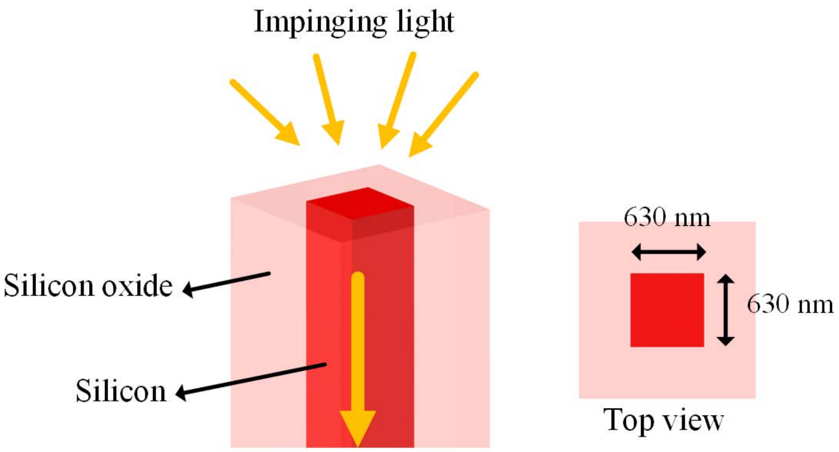

Figure 6.12: A single pillar as a non-planar antenna that supports 4 mode pairs that each pair collect power from two orthogonal polarization.

dielectric slab for the antenna area and exploited an optimization method to generate an etching pattern on the slab. The etching pattern consists of 150 nm blocks that are either etched or left unetched. Therefore, the etching pattern can be represented by a binary pattern, which makes genetic algorithm a suitable optimization method for the problem [20]. The physical antenna aperture is chosen a relatively small square of 3.8 µm by 4 µm. Therefore, FOV of each mode is larger than the 2-mode antenna presented above. The effective aperture of the antenna is shown in Fig. 6.11(c) exhibiting a broad FOV range with a peak effective aperture of 1.6 μm^2. Figure 6.11(c) also shows the effective aperture versus angle for the tree modes individually which illustrates the contribution of each mode in the overall power collection capability of the antenna.

Constructing a super-mode using multiple uncoupled single modes yields a larger antenna footprint as the number of modes increases. An alternative structure is an antenna with a single physical port that supports multiple modes. To collect the output signal of the antenna, a single waveguide that supports those modes and is matched to the input port of the antenna at each mode is needed. In a standard silicon photonics process with silicon layer thickness of 220 nm, the width of a single mode waveguide is 0.5 µm and larger waveguide width introduces more modes that are supported by the waveguide. Since the group index of different modes of a multi-mode waveguide differ a lot, a grating structure is not very effective to construct the antenna aperture and a patterned slab similar to Fig. 6.11 is needed to achieve high performance.

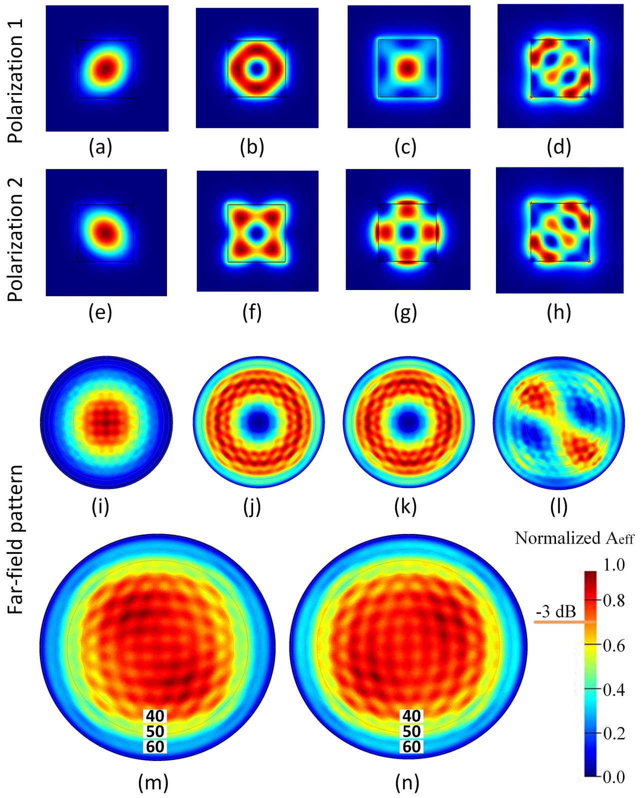

Figure 6.13: The graphs are normalized and the color bar shows the relative intensity (a)-(d) Modes of the polarization set 1 (e)-(h) modes of the polarization set 2 (i)-(l) Effective area of the polarization set 1 modes (effective area for the set 2 is counterpart of these graphs) (m) Collective effective area of set 1 (n) collective area of set 2.

While an integrated planar multi-mode antenna significantly increases the collection area compared to the conventional nano-photonic antennas, non-planar antenna designs can potentially lead to solutions with higher fill factor and broader FOV due to the addition of the third dimension that can be used to support additional modes. To demonstrate this possibility through an example, we propose a multi-mode silicon pillar antenna with a square cross-section of 630 nm by 630 nm surrounded by silicon oxide. Although air as the surrounding material results in a better confinement of the optical field in the silicon pillar, silicon oxide is used here for better mechanical stability and fabrication yield. The dimensions and the higher dielectric constant of silicon compared to the surrounding silicon oxide defines the supported modes of the antenna. The antenna supports four pairs of modes and each pair covers two orthogonal polarizations of the same kind, as in Fig. 6.13(a)-(h). The difference between the electric field distribution of the mode profiles, the amplitude distribution as well as their phase distribution, leads to a different far-field radiation pattern for each mode, where the effective aperture of each mode covers different angular ranges. The reciprocity theorem can be used for each mode separately to obtain the antenna effective aperture corresponding to that mode, which are shown in Fig. 6.13(i)-(l). The collective effective aperture for the two polarization sets are shown in Fig. 6.13(m) and (n) achieving a broader overall antenna FOV. It should be noted that as it is explained in section 6.2, a conventional antenna has a maximum collection area for a particular polarization and zero collection capability for the orthogonal polarization. However, in this structure, not only a large FOV is achieved, but also the pillar antennas have large effective aperture and FOV for both polarizations of the incident wave.

The compact form factor of this pillar antenna makes it a suitable candidate for a dense receiver array aperture with broad FOV and large fill factor. Due to the large index contrast of silicon with the surrounding oxide medium, the modes of the single antennas will not get affected significantly by the neighboring array elements [151] and the major modes of the array will essentially resemble the modes of a single antenna. Figure 6.14(a) shows the antenna array incorporating pillar antennas as array elements. The element spacing of the array and the dimensions of the antenna are optimized to maximize the power collected by each unit cell. The ratio of the collected power by each unit cell to the total incident power (Fig. 6.14(b) & (c)) is more than 95% for a broad range of FOV exceeding 140° by 140°. It should be noted that the effective area of each antenna is close to its upper bound in an array, as discussed previously. Noticeably, both FOV and effective apertures are pushed to their limits independently in this architecture.

In a photonic receiver array, the area of the photodetector is generally a fraction of the unit cell due to the space occupied by various other photonic and electronic components as well as metal interconnects and interfaces. To achieve a large fill factor, an antenna should receive and confine the incident light into a smaller volume so that it can be coupled into the photodetector efficiently. Hence, the dimensions of the pillar antenna and the array element spacing are optimized such that it confines the optical power into a $0.6\,\mu\text{m}$ by $0.6\,\mu\text{m}$ window in the vicinity of the pillar while maintaining a large effective aperture. Figure 6.15 shows the power focusing capability of the array into a small region of the antenna. Since the propagation speed of different modes are not the same, a periodic intensity distribution is formed that peaks where all the modes are in phase. Since effective aperture of the modes

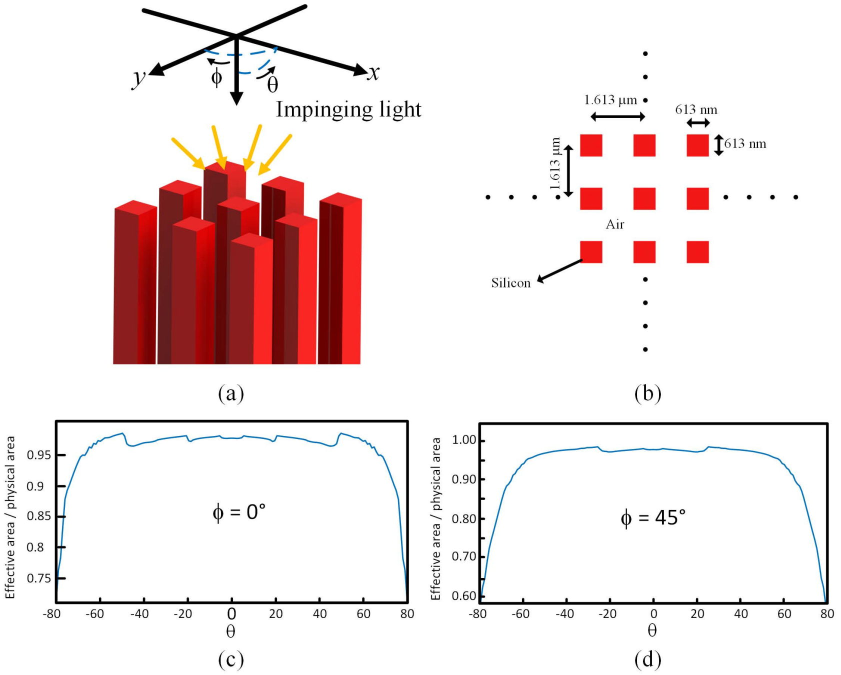

Figure 6.14: (a) Dense array of pillar antennas (b) top view of the array with dimensions of each unit cell (c)&(d) power collection efficiency of the nit cell versus azimuth angles 0° and 45°

vary versus reception angle, the relative magnitude of modes changes accordingly. Therefore, the focusing capability of the antenna is affected for larger angles. A metric for effective aperture of the focusing, which takes into account only the fraction of the power in the 0.6 µm by 0.6 µm window is a more precise measure of the performance of the antennas in an array. Figure 6.15(e) & (f) show the focusing effective aperture of the antenna versus reception angle. While the uniformity of the effective aperture is not the same as the full unit cell, the 3 dB FOV of the aperture exceeds 160°. The antenna collects about 80% of the incident power which corresponds to the effective area of $2.1\,\mu\text{m}^2$. Given that the aperture area of the antenna is considered 0.6 by $0.6\,\mu\text{m}^2 = 0.36\,\mu\text{m}^2$, the multi-mode aperture efficiency of this pillar antenna in the array structure is

$$\epsilon_{ap} = \frac{A_{eff}}{A_{phy}} = 5.8, \tag{6.12}$$

in which A_{eff} is the effective aperture of the antenna and A_{Phy} is the physical area of the antenna. Large aperture efficiency and FOV suggest the application of this structure for a dense optical phased array coherent receiver. To further clarify the merits of this structure, it can be compared to the recently published optical phased

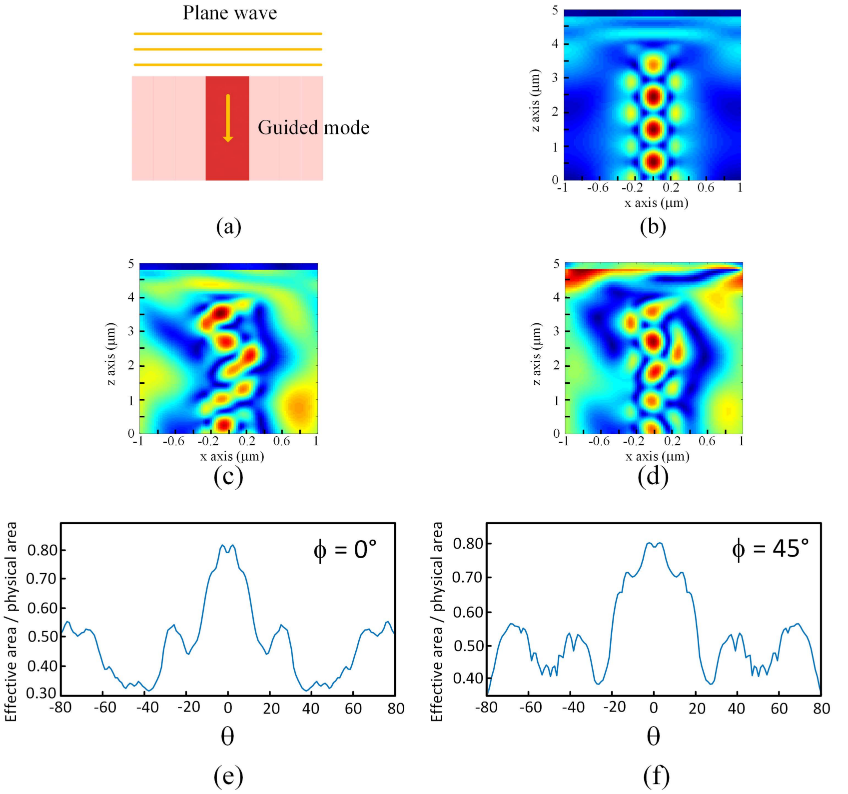

(a) (b) (c) (d) (e) (f)

Figure 6.15: Power collection efficiency of the array in a 0.6 µm by 0.6 µm window around the pillar antenna (a) azimuth angle = 0° (b) azimuth angle = 45°

array receivers [23] which uses conventional nano-photonic antennas in an array for collecting the incident power. The antenna in [23] has 0.92 μm^2 of peak effective aperture at $-6°$ with unit cell size of 11.2 by 11.2 μm^2, where it achieves an aperture efficiency of 0.0074 while the array element spacing limits its FOV to 8°.

6.6 Conclusion

In this chapter, we studied the fundamental limits of antenna design for photonic transmitter and receiver systems and proposed architectures for designing high-performance antennas. An approximated upper bound for radiation efficiency of a transmitter antenna in standard single layer silicon photonics processes is derived based on which architectures for improving the radiated power fraction and reducing the stray light are demonstrated. For the receiver antenna, maximizing the collection efficiency while maintaining the FOV of the receiver is the desired design target due to the typically weak received signal levels. However, the strong relationship between the antenna characteristics in the transmit and receive modes introduce trade-offs in the design space of conventional antennas. Via an idealized model, the trade-offs are quantified and novel architectures for designing high-performance antennas beyond these limitations are demonstrated. Finally, a photonic coherent receiver achieving more than 95% collection efficiency and 170° of FOV utilizing a multi-mode dense pillar antenna array is demonstrated.

Chapter 7

LOW POWER RF PULSE TRANSCEIVER

In this chapter, a novel time-variant electronic circuit is introduced which has the capability of generating and receiving short RF/microwave pulses, in particular modulated Hermite pulses. This architecture generates pulses while transitioning between on- and off-states and detects the received pulses with its correlation-based functionality. This transient-based operation with functioning time at the scale of the pulse duration allows for implementing ultra-low power systems using this architecture as its heart. In the following, first the need for a low power electronic pulse generator/receiver for various applications is discussed. Then, the process of constructing such systems is explained and a capacitor-based network to form a transmitter/receiver is presented. Moreover, an example of a transceiver system utilizing such systems is proposed.

7.1 Introduction

Generating short pulses with defined amplitude shapes and phase/frequency modulation is required for many applications. However, the electronics required for generation of such pulses is power hungry due to the large bandwidth of the short pulses which needs high speed circuits. The large power consumption of pulse generators is a major drawback for applications such as portable pulse radars for ranging and imaging and drive circuitry for solid-state-based quantum computers. In particular, for a quantum computer with integrated electronics that operates at sub-Kelvin or a few Kelvins temperatures with strictly limited power budget, rules out the existing techniques for generating RF/microwave pulses. While the the generated pulse occupies a short time span of the output signal, long start-up time and back-end processing needs for a constantly working system. However, ideally, a system which operates only for the short width of the pulse is sufficiency for generating the desired output. Such a non-conventional system requires novel circuit topologies and signaling techniques. Moreover, the complexity of the system should be significantly reduced if ultra-low power consumption is desired.

In addition to generating a short pulse, receiving it and processing the pulse to extract its properties such as frequency, amplitude, and position in time is equally important and usually needed in the same system that generated the pulse. Detecting a signal (pulse or not) optimally needs a correlation-based receiver which is usually happens in the digital domain with hundreds of correlators in wireless communication, ranging, and imaging systems. The low-noise amplification, down-conversion, digitization, and digital processing need to form a receiver chain lead to a high complexity and power consumption. Moreover, these circuit blocks are continuously operating and quenching them is not usually practical due to the long wake up-time of the circuits. Similar to the transmitter, it is ideally possible to have a receiver that turns on when a pulse is received, processes the pulse and goes off a short time after the pulse is over. However, a non-conventional circuit topology is needed to implement such a system as well.

Here, to reduce the system power consumption, a novel time-dependent system is devised that has the capability of generating and receiving a wide range of RF pulses using only a base-band signal as a controlling input. This system is best suitable for generating/receiving Hermit pulses which are orthogonal pulses of Gaussian family. For a given bandwidth, a Gaussian pulse has the minimum time-width which makes it a good candidate for ultra-low power that operate only during the presence of the pulse. The receiving mechanism of the system performs a correlation on the input signal which yields the optimum sensitivity of detection.

7.2 Theoretical development

To devise a system that can transmit and receive specific pulses, impulse response of an electrical circuit can be used. The impulse response of linear time-invariant systems are limited to decaying or oscillatory exponential and can not be used to generate many useful waveforms. Since linearity is a key feature in RF transceivers which is necessary for handling large destructive interference signals and processing the desired signal with high integrity, we consider the general form of linear time-variant systems as a starting point. Such a system has a time-variant impulse response of $h(t,\tau)$ in which t is the time and τ is the time instance that the input impulse is applied, Fig. 7.1.

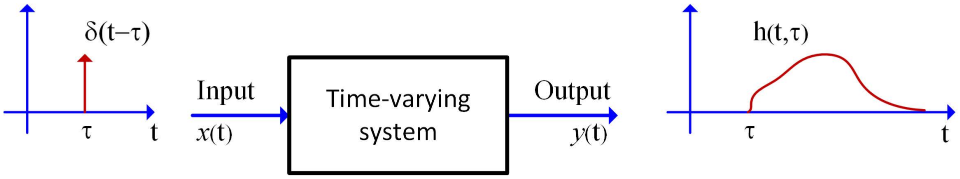

Figure 7.1: Schematic of a time-varying system and its impulse response.

If the impulse response of the system is engineered properly, by applying an impulse at the input, the desired pulse shape is generated at the output. Moreover, if an input $x(t)$, containing the same pulse, additive noise, and other unwanted signals are fed to the system, the output of the system, $y(t)$, is

$$y(t) = \int_{-\infty}^{t} h(t, \tau)x(\tau)d\tau, \tag{7.1}$$

which has the form of a correlation between the input and the impulse response (the pulse template). Correlation-based detection yields the optimum sensitivity in the presence of additive white Gaussian noise and is used in many systems for signal processing and detection. Therefore, engineering the impulse response of a linear time-varying system has the potential for realizing a system capable of transmitting and receiving RF/microwave pulses.

Since the low-power feature is achieved by activating the system only when the pulse is present, a pulse with smaller time duration for a given spectral bandwidth is desirable. Moreover, if the pulse is used for ranging, the width of the pulse determines the range resolution of the system. Among all the waveforms, a Gaussian pulse has the smallest possible time-bandwidth product which makes it a good candidate for this purpose. An extension of this pulse shape is the family of orthogonal modified Hermite pulses (here referred to as Hermite pulses for simplicity). Hermite pulses form an orthogonal set of waveforms that are suitable for various applications such as channel multiplexing, complex symbol transmission, etc. These pulses can be generated by modifying Hermite polynomials to form an orthogonal set [152] which are

$$\begin{aligned} h_0(t) &= k_0 e^{-\frac{t^2}{4\tau^2}} \\ h_1(t) &= k_1 \frac{t}{\tau} e^{-\frac{t^2}{4\tau^2}} \\ h_2(t) &= k_2 \big[(\frac{t}{\tau})^2 - 1 \big] e^{-\frac{t^2}{4\tau^2}} \\ &\dots \end{aligned} \tag{7.2}$$

A linear time-dependant system can be expressed analytically by a linear differential equation with time-dependant coefficients. First order differential equation of such kind can be expressed as

$$y'(t) + a(t)y(t) = g(x(t)), \tag{7.3}$$

in which $g(t)$ is a functional of the input waveform and the coefficient of the highest degree is assumed to be 1 without the loss of generality[1]. The response of such a system can be written in closed form as

$$y(t) = e^{-\int_{-\infty}^{t} a(\lambda)d\lambda} \int_{-\infty}^{t} g(x(\tau)) e^{\int_{-\infty}^{\tau} a(\lambda)d\lambda} d\tau, \tag{7.4}$$

on intervals that $a(t)$ is continuous. The response of this system is shaped by the behaviour of $a(t)$ which can be used to generate the desired pulse shape. However, having an RF pulse for $y(t)$ requires variation by the same frequency for $a(t)$ which necessitates a complex control waveform. Moreover, the degrees of freedom of this system is limited and more suitable for base-band signal generation. While the techniques explained in the following could be used to design a system of the first order, since generating Gaussian RF pulses are targeted here, we proceed to the higher order differential equations.

The general form of a second order time-dependent differential equation is

$$y'' + b(t)y' + c(t)y = g(x(t)), \tag{7.5}$$

which represents the dynamics of a second order time-varying system in a general form. In contrast to the first order differential equation, it is not possible to derive closed form solutions for higher order equations. Therefore, we take an alternative approach to construct the response that can generate the Hermite pulses. Since Hermit pulses have a Gaussian component, we first perform a change of variable to add an exponential term to the output response. Moreover, following the pattern of the output response of the first order equation, it would be more natural to write this term as an integral of a function which yields a change of variable as

$$y(t) = u(t) e^{\int_{-\infty}^{t} p(\lambda)d\lambda}. \tag{7.6}$$

Note that this specific shape of formulating the exponential factor does not limit the generality of the exponential function since the whole integral can be considered an arbitrary function. Therefore, by applying this change of variable, equation (7.6) can be written as

$$u'' + (2p(t) + b(t))u' + (p'(t) + p^2(t) + p(t)b(t) + c(t))u = e^{-\int_{-\infty}^{t} p(\lambda)d\lambda} g(x(t)), \tag{7.7}$$

---

[1] In the case of an arbitrary coefficient for the highest order derivative, the two sides of the equation can be divided by that coefficient to reduce the differential equation to the form of equation (7.3).

To achieve a simplified form we choose $p(t) = -b(t)/2$. Note that equation (7.7) still shows the general form of a second order linear time-dependent differential equation since this process can be done for any arbitrary equation. Substituting $p(t)$ in equation (7.7) yields

$$u'' + \omega^2(t)u = e^{-\int_{-\infty}^{t} p(\lambda)d\lambda} g(x(t)), \tag{7.8}$$

in which (7.5) can be written as

$$\omega^2(t) = (-\frac{b'(t)}{2} - \frac{b^2(t)}{4} + c(t)). \tag{7.9}$$

The advantage of expressing the differential equation in this form is that it resembles the simple differential equation with constant $\omega(t) = \omega_0$ which has sinusoidal responses. The sinusoidal response can be used to generate the carrier frequency, a feature that the first order system was not able to provide. In fact, since variations of the exponential envelope can be controlled by $b(t)$ to shape a pulse, it would be desirable to achieve a constant $\omega(t) = \omega_0$ for generating the sine and cosine functions as RF carriers. Therefore, using the method of variation of parameters, the response of the system to $x(t)$ can be written as

$$\begin{aligned} y(t) = e^{-\frac{1}{2}\int_{-\infty}^{t} b(\lambda)d\lambda} \Bigg[&\sin(\omega_0 t) \int_{-\infty}^{t} g(x(\tau)) \cos(\omega_0 \tau) e^{\frac{1}{2}\int_{-\infty}^{\tau} b(\lambda)d\lambda} d\tau \\ &- \cos(\omega_0 t) \int_{-\infty}^{t} g(x(\tau)) \sin(\omega_0 \tau) e^{\frac{1}{2}\int_{-\infty}^{\tau} b(\lambda)d\lambda} d\tau \Bigg], \end{aligned} \tag{7.10}$$

which can be modified in the shorter form of

$$y(t) = \int_{-\infty}^{t} g(x(\tau)) \cos(\omega_0 (t - \tau)) e^{\frac{1}{2}\int_{t}^{\tau} b(\lambda)d\lambda} d\tau. \tag{7.11}$$

Therefore, if the input functional is a simple operation $g(x(t)) = Ax(t)$, the impulse response of the system is

$$h(t, \tau) = \cos(\omega_0 (t - \tau)) e^{\frac{1}{2}\int_{t}^{\tau} b(\lambda)d\lambda}. \tag{7.12}$$

Since the practical systems follow the rules of causality, we can add a term $u(t - \tau)$ to the impulse response without affecting its shape to represent causality explicitly. Thus the convolution integral can be modified to

$$y(t) = \int_{-\infty}^{\infty} x(\tau) h(t, \tau) u(t - \tau) d\tau, \tag{7.13}$$

which has the form of correlation between $x(t)$ and $h(t,\tau)u(t-\tau)$. However, in a practical application, the output of the system should be observed at a finite time t_0 (waiting to infinity is not possible). Therefore, the output signal will be

$$y(t_0) = \int_{-\infty}^{t_0} x(\tau)h(t_0,\tau)d\tau, \tag{7.14}$$

which requires non-zero part of $x(t)$ (the pulse) happening before t_0 to maintain the full correlation effect. Since $h(t,\tau)$ varies with time, the exact correlation that is calculated at time instance t_0 is between $x(t)$ and $h(t_0,\tau)$. Consequently, the job of the designer is to adjust $h(t_0,\tau)$ to have the desired pulse shape, here Hermite pulses.

For simplicity we start with the Gaussian pulse which is the first Hermite pulse and then extend the system design to higher orders to generate higher order pulses. A general form of a Gaussian pulse is

$$p(t) = Ae^{-\left(\frac{t}{\tau}\right)^2}, \tag{7.15}$$

and shown in Fig. 7.2. This is also called base-band Gaussian pulse since its spectral content starts from DC and has a low-pass shape. The 3 dB pulse width of a Gaussian pulse is 1.2τ and total pulse duration is about 4τ. Fourier transform of this pulse is also a Gaussian waveform

$$P(f) = A\tau\sqrt{\pi}e^{-(\pi f\tau)^2}, \tag{7.16}$$

which has -10 dB bandwidth of 340 MHz for τ =1 ns.

Despite its simplicity, a base-band pulse is not suitable for many applications due to the large size of the antennas required for radiation and reception. An RF carrier can be used to shift the spectral content of the pulse to higher frequencies which yields a modulated Gaussian pulse as

$$p(t) = Ae^{-\left(\frac{t}{\tau}\right)^2}\cos(\omega_0(t-t_c)), \tag{7.17}$$

which has a center frequency of $\omega_0 = 2\pi f_0$ and t_c represents an arbitrary carrier phase in the form of a time delay. Number of cycles in the pulse depends on the magnitude of the product $\omega_0\tau$ which determines the fractional bandwidth of the pulse as well. Moreover, in case of $\omega_0 t_c = (n+1/2)\pi$ there is no DC component in the spectrum of the wave. Otherwise, there will be a DC component that gets smaller as ω_0 increases for a fixed τ.

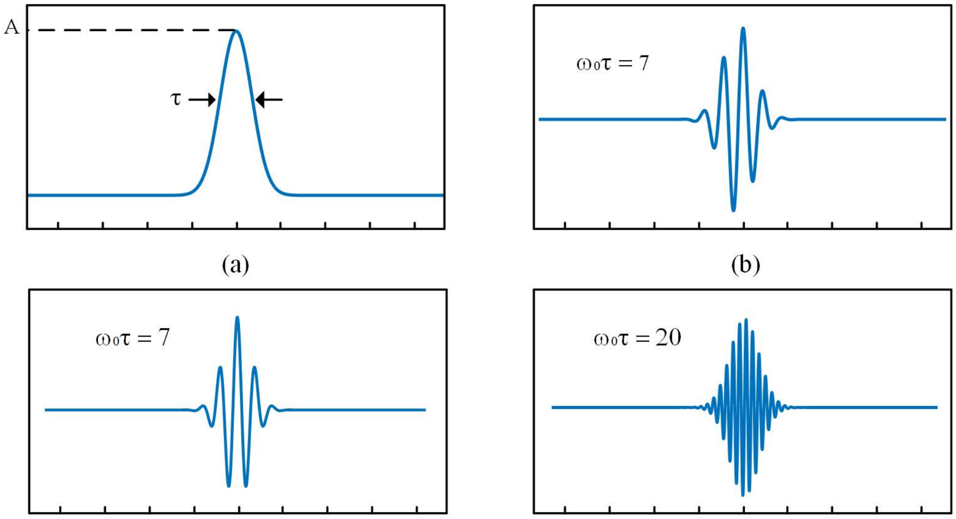

(a) (b) (c) (d)

Figure 7.2: (a) A base-band Gaussian pulse (b) Modulated Gaussian pulse without DC component (c) Modulated Gaussian pulse with DC components (d) Modulated Gaussian pulse with many cycles.

The similarities between equation (7.17) and (7.12) shows the potential capability of the discussed system for implementing RF pulse transmitter and receiver using its impulse response. To generate a Gaussian envelope, $b(t)$ needs to be adjusted to have a ramp shape. While Gaussian pulses are the focus of this study here, other pulse shapes can also be generated by engineering $b(t)$.

7.3 System implementation

To implement a second order system, two energy storing components should be embedded inside the network. Since capacitor and inductor are the commonly used elements in electronic circuits with energy storing capability, two capacitors, two inductors, or a capacitor and an inductor are the three options to implement these systems. Moreover, the two energy storing components should be coupled to each other to realize a second order behavior. To have a time-dependent circuit, the behaviour of some of the components should be varied versus time which can be the resistivity of a switch or the value of a component. Since changing capacitors and inductors usually faces limitations and are undesirable, it is more convenient to have variable resistance and conductance in the circuit. Resistance and conductance are the memoryless elements that do not increase the order of the network and are easy to implement while the system complexity and cost is kept low. Also, switching can be considered as a subset of variable resistors. Therefore, we choose the varying resistance and conductance here to add time-dependence to the circuit. Figure 7.3 shows two examples of such networks in two-capacitor and two-inductor settings which are coupled to each other through *gm* blocks and have variable resistance for time-variability. Since the capacitors and resistors are in parallel configuration with input and output in the form of current and voltage, *gm* blocks are used to read the voltage of one and inject current to the other to achieve coupling. Since inductors are usually bulky and interact with each other, we choose the two-capacitor circuit for the following analysis. However, the two-inductor network is a dual circuit and shows the same behavior.

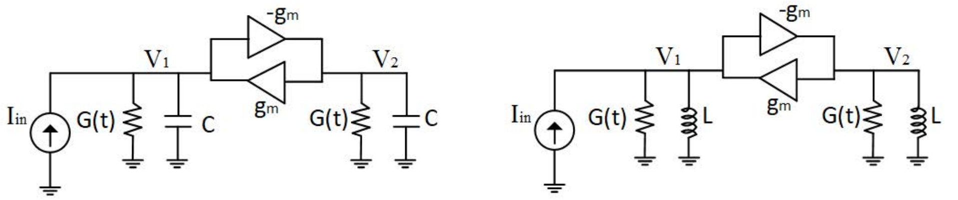

(a) (b)

Figure 7.3: (a) Two-capacitor time-varying circuit (b) Two-inductor time-varying circuit.

The circuit of Fig. 7.3(a) is governed by the following relationships:

$$C\begin{bmatrix}V_1'\\ V_2'\end{bmatrix} = \begin{bmatrix}-G(t) & g_m\\ -g_m & -G(t)\end{bmatrix}\begin{bmatrix}V_1\\ V_2\end{bmatrix}\begin{bmatrix}I_{in}\\ 0\end{bmatrix} \tag{7.18}$$

According to equation (7.5) we apply a change of variable

$$V_i = e^{\int_{-\infty}^{t} q(\lambda)d\lambda} U_i \tag{7.19}$$

and select $q(t)$ such that the resulting system of differential equation is a time-invariant second order system with sinusoidal responses as described in the previous chapter, which yields

$$\begin{bmatrix}U_1'\\ U_2'\end{bmatrix} = \begin{bmatrix}0 & \frac{g_m}{C}\\ -\frac{g_m}{C} & 0\end{bmatrix}\begin{bmatrix}U_1\\ U_2\end{bmatrix}\begin{bmatrix}I_{in}e^{\int_t^\tau \frac{G(t)}{C}}\\ 0\end{bmatrix} \tag{7.20}$$

under the condition of

$$q(t) = -\frac{G(t)}{C}. \tag{7.21}$$

This condition removes $G(t)$ after the process of changing the variable and yields a time-invariant system. This system of two first order differential equations can be written as a second order equation with $\omega_0 = \frac{g_m}{C}$ and the impulse response of

$$\begin{aligned} h_{V_1}(t,\tau) &= e^{\int_t^\tau \frac{G(\lambda)}{C} d\lambda} \cos(\omega_0 t) u(t-\tau) \\ h_{V_2}(t,\tau) &= e^{\int_t^\tau \frac{G(\lambda)}{C} d\lambda} \sin(\omega_0 t) u(t-\tau). \end{aligned} \tag{7.22}$$

The response of these two nodes are in quadrature relationship and can be combined to achieve the desired phase of the carrier in the transmitter mode and I/Q mixing for base-band correlation in the receiver mode. Since Gaussian pulses are desired, $G(t)$ should have a ramp shape to generate the term $-t^2$ for the power of the exponential.

Since hither order Hermite pulses are based on higher order polynomials, generation and reception of them requires higher order systems (differential equations). The presented analysis in the matrix form can be easily extended to higher orders to represent these systems. The key feature in realizing a system is that after the application of the change of variables in equation (7.19), the system of differential equations turn into a time-invariant system. The parameters of that system is then can be adjusted to achieve different characteristic polynomials with decaying and oscillatory terms and the exponential envelope is used to shape the pulse.

The introduced architecture with two capacitors has the capability of being extended to higher orders by stacking similar blocks. To generating the first two Hermite pulses, the architecture of Fig. 7.4(a) can be used. This network generates all the components required for these two pulses with both sine and cosine (quadrature) modulating carriers. Therefore, by combining the four output voltages of this circuit with weighting coefficients, the desired waveforms can be generated.

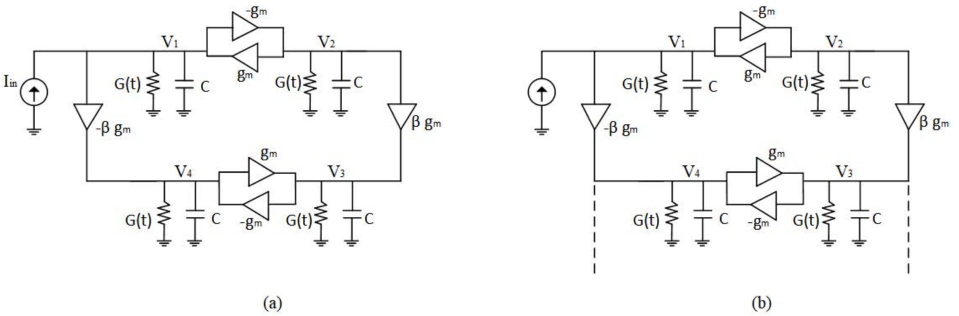

Figure 7.4: (a) 4th order circuit for generation and reception of the first and second order Hermite pulses with both sine and cosine carriers (b) This architecture can be extended for higher order Hermite pulses by extending the it.

The circuit of Fig. 7.4(a) is governed by the following relationships

$$C\begin{bmatrix} V_1' \\ V_2' \\ V_3' \\ V_4' \end{bmatrix} = \begin{bmatrix} -G(t) & g_m & 0 & 0 \\ -g_m & -G(t) & 0 & 0 \\ 0 & \beta g_m & -G(t) & g_m \\ -\beta g_m & 0 & -g_m & -G(t) \end{bmatrix} \begin{bmatrix} V_1 \\ V_2 \\ V_3 \\ V_4 \end{bmatrix} \begin{bmatrix} I_{in} \\ 0 \\ 0 \\ 0 \end{bmatrix}, \tag{7.23}$$

After applying the change of variables (7.19) and using (7.21) we get

$$\begin{bmatrix} U_1' \\ U_2' \\ U_3' \\ U_4' \end{bmatrix} = \begin{bmatrix} 0 & \frac{g_m}{C} & 0 & 0 \\ \frac{-g_m}{C} & 0 & 0 & 0 \\ 0 & \beta\frac{g_m}{C} & 0 & \frac{g_m}{C} \\ -\beta\frac{g_m}{C} & 0 & \frac{-g_m}{C} & 0 \end{bmatrix} \begin{bmatrix} U_1 \\ U_2 \\ U_3 \\ U_4 \end{bmatrix} \begin{bmatrix} e^{\int_{-\infty}^{t} G(\lambda)/C} I_{in} \\ 0 \\ 0 \\ 0 \end{bmatrix}, \tag{7.24}$$

which can be shown having the impulse response of

$$h_(t,\tau) = e^{\int_t^\tau \frac{G(\lambda)}{C} d\lambda} \begin{bmatrix} \cos(\omega_0(t-\tau)) \\ -\sin(\omega_0(t-\tau)) \\ -\beta\omega_0(t-\tau)\sin(\omega_0(t-\tau)) \\ -\beta\omega_0(t-\tau)\cos(\omega_0(t-\tau)) \end{bmatrix} u(t-\tau). \tag{7.25}$$

By linearly combining these four outputs, any Gaussian pulse with polynomial coefficient of first order can be realized. Moreover, any carrier phase on the transmitter mode and quadrature mixing in the receiver mode are achievable.

The presented architecture also has the capability of being extended to generate/receive higher order pulses by simply adding more stages to the network, Fig. 7.4(b). The node voltages of this circuit can be combined to form various forms of impulse responses in the shape of Hermite pulses. If this system is triggered with an input current, it generates the pulse which can be amplified and transmitted with an antenna, or attenuated and delivered to a qubit. Moreover, this system performs a correlation operation on its input waveform and yields optimum reception for the pulse that it generates.

Figure 7.5 demonstrates a potential system structure that can be realized with such a time-varying network at its heart, TVMF. This system can generate the desired RF pulses and transmit them through the antenna. The phase and amplitude of each pulse can be modulated and various pulses can be selected for transmission. On the receiver chain, the received signal is fed to the TVMF for correlation-based reception. Therefore, this system can be used for send/receive data or perform ranging and imaging by transmitting pulses and process the reflection. Multiple systems of this kind can operate simultaneously in an environment through multiplexing the space access by using different orthogonal Hermite pulses.

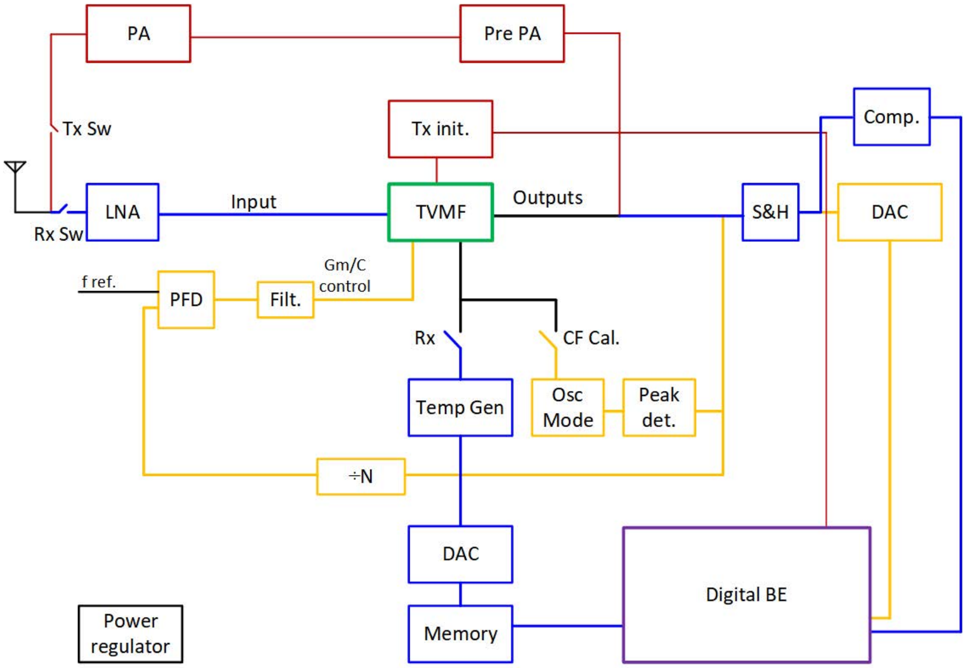

Figure 7.5: A pulse transceiver system for radar ranging and imaging, as well as data communication.

BIBLIOGRAPHY

[1] A. I. Sabra, *The Optics of Ibn Al-Haytham*, ser. Studies of the Warburg Institute (Book 40). Warburg Institute, 1989, ISBN: 978-0854810727.

[2] S. Hawking, *On the Shoulders of Giants: The Great Works of Physics and Astronomy*. Penguin, 2003, ISBN: 9780141015712. [Online]. Available: `https://books.google.com/books?id=eghMcJxGcYwC`.

[3] C. Huygens, *Treatise On Light*. Outlook Verlag, 2020, ISBN: 9783752308167. [Online]. Available: `https://books.google.com/books?id=-8nxDwAAQBAJ`.

[4] A. Wright, "Let there be light," *Nature Materials*, vol. 9, no. 1, S5–S5, 2010, ISSN: 1476-4660. DOI: `10.1038/nmat2638`. [Online]. Available: `https://doi.org/10.1038/nmat2638`.

[5] T. Levitt, *A Short Bright Flash: Augustin Fresnel and the Birth of the Modern Lighthouse*. W. W. Norton, 2013, ISBN: 9780393068795. [Online]. Available: `https://books.google.com/books?id=HRlL7hwDS8oC`.

[6] D. Cheng, *Field and Wave Electromagnetics*, ser. Addison-Wesley series in electrical engineering. Addison-Wesley Publishing Company, 1989, ISBN: 9780201128192. [Online]. Available: `https://books.google.com/books?id=KL%5C_vAAAAMAAJ`.

[7] J. Goodman, *Introduction to Fourier Optics*, ser. McGraw-Hill physical and quantum electronics series. W. H. Freeman, 2005, ISBN: 9780974707723. [Online]. Available: `https://books.google.com/books?id=ow5xs%5C_Rtt9AC`.

[8] S. D'Agostino, *A History of the Ideas of Theoretical Physics: Essays on the Nineteenth and Twentieth Century Physics*, ser. Boston Studies in the Philosophy and History of Science. Springer Netherlands, 2001, ISBN: 9781402002441. [Online]. Available: `https://books.google.com/books?id=OVRNaJZy0CkC`.

[9] J. Ramsay, "Highlights of antenna history," *IEEE Communications Magazine*, vol. 19, no. 5, pp. 4–8, 1981.

[10] J. Hecht, "A short history of laser development," *Appl. Opt.*, vol. 49, no. 25, F99–F122, 2010. DOI: `10.1364/AO.49.000F99`. [Online]. Available: `http://ao.osa.org/abstract.cfm?URI=ao-49-25-F99`.

[11] C. Maurer, A. Jesacher, S. Bernet, and M. Ritsch-Marte, "What spatial light modulators can do for optical microscopy," *Laser & Photonics Reviews*, vol. 5, no. 1, pp. 81–101, 2011. DOI: `10.1002/lpor.200900047`. eprint: `https://onlinelibrary.wiley.com/doi/pdf/10.1002/lpor.200900047`. [Online]. Available: `https://onlinelibrary.wiley.com/doi/abs/10.1002/lpor.200900047`.

[12] Y.-X. Ren, R.-D. Lu, and L. Gong, “Tailoring light with a digital micromirror device,” *Annalen der Physik*, vol. 527, no. 7-8, pp. 447–470, 2015. doi: `10.1002/andp.201500111`. eprint: `https://onlinelibrary.wiley.com/doi/pdf/10.1002/andp.201500111`. [Online]. Available: `https://onlinelibrary.wiley.com/doi/abs/10.1002/andp.201500111`.

[13] S. Li and J. Wang, “Adaptive free-space optical communications through turbulence using self-healing bessel beams,” *Scientific Reports*, vol. 7, no. 1, p. 43 233, 2017, issn: 2045-2322. doi: `10.1038/srep43233`. [Online]. Available: `https://doi.org/10.1038/srep43233`.

[14] L. Vicari, *Optical Applications of Liquid Crystals*, ser. Series in Optics and Optoelectronics. CRC Press, 2016, isbn: 9781420033748. [Online]. Available: `https://books.google.com/books?id=EU%5C_MBQAAQBAJ`.

[15] F. P. Kapron, D. B. Keck, and R. D. Maurer, “Radiation losses in glass optical waveguides,” *Applied Physics Letters*, vol. 17, no. 10, pp. 423–425, 1970. doi: `10.1063/1.1653255`.

[16] T. Miya, Y. Terunuma, T. Hosaka, and T. Miyashita, “Ultimate low-loss single-mode fibre at 1.55 µm,” *Electronics Letters*, vol. 15, no. 4, pp. 106–108, 1979.

[17] Y. Tamura, H. Sakuma, K. Morita, M. Suzuki, Y. Yamamoto, K. Shimada, Y. Honma, K. Sohma, T. Fujii, and T. Hasegawa, “Lowest-ever 0.1419-db/km loss optical fiber,” in *2017 Optical Fiber Communications Conference and Exhibition (OFC)*, 2017, pp. 1–3.

[18] G. Rademacher, R. S. Luís, B. J. Puttnam, T. A. Eriksson, R. Ryf, E. Agrell, R. Maruyama, K. Aikawa, Y. Awaji, H. Furukawa, and N. Wada, “High capacity transmission with few-mode fibers,” *J. Lightwave Technol.*, vol. 37, no. 2, pp. 425–432, 2019. [Online]. Available: `http://jlt.osa.org/abstract.cfm?URI=jlt-37-2-425`.

[19] A. E. Lim, J. Song, Q. Fang, C. Li, X. Tu, N. Duan, K. K. Chen, R. P. Tern, and T. Liow, “Review of silicon photonics foundry efforts,” *IEEE Journal of Selected Topics in Quantum Electronics*, vol. 20, no. 4, pp. 405–416, 2014.

[20] R. Fatemi, A. Khachaturian, and A. Hajimiri, “A nonuniform sparse 2-D large-fov optical phased array with a low-power pwm drive,” *IEEE Journal of Solid-State Circuits*, vol. 54, no. 5, pp. 1200–1215, 2019. doi: `10.1109/JSSC.2019.2896767`.

[21] R. Fatemi, A. Khachaturian, and A. Hajimiri, “Scalable optical phased array with sparse 2D aperture,” in *Conference on Lasers and Electro-Optics*, Optical Society of America, 2018, STu4B.6. doi: `10.1364/CLEO_SI.2018.STu4B.6`. [Online]. Available: `http://www.osapublishing.org/abstract.cfm?URI=CLEO_SI-2018-STu4B.6`.

[22] R. Fatemi, A. Khachaturian, and A. Hajimiri, “A low power pwm optical phased array transmitter with 16° field-of-view and 0.8° beamwidth,” in *2018 IEEE Radio Frequency Integrated Circuits Symposium (RFIC)*, 2018, pp. 28–31. DOI: `10.1109/RFIC.2018.8428847`.

[23] R. Fatemi, B. Abiri, A. Khachaturian, and A. Hajimiri, “High sensitivity active flat optics optical phased array receiver with a two-dimensional aperture,” *Opt. Express*, vol. 26, no. 23, pp. 29 983–29 999, Nov. 2018. DOI: `10.1364/OE.26.029983`. [Online]. Available: `http://www.opticsexpress.org/abstract.cfm?URI=oe-26-23-29983`.

[24] R. Fatemi, B. Abiri, and A. Hajimiri, “A one-dimensional heterodyne lens-free OPA camera,” in *Conference on Lasers and Electro-Optics*, Optical Society of America, 2016, STu3G.3. DOI: `10.1364/CLEO_SI.2016.STu3G.3`. [Online]. Available: `http://www.osapublishing.org/abstract.cfm?URI=CLEO_SI-2016-STu3G.3`.

[25] ——, “An 8×8 heterodyne lens-less OPA camera,” in *Conference on Lasers and Electro-Optics*, Optical Society of America, 2017, JW2A.9. DOI: `10.1364/CLEO_AT.2017.JW2A.9`. [Online]. Available: `http://www.osapublishing.org/abstract.cfm?URI=CLEO_QELS-2017-JW2A.9`.

[26] B. Abiri, R. Fatemi, and A. Hajimiri, “A 1-D heterodyne lens-free optical phased array camera with reference phase shifting,” *IEEE Photonics Journal*, vol. 10, no. 5, pp. 1–12, 2018. DOI: `10.1109/JPHOT.2018.2871823`.

[27] D. T. Amm and R. W. Corrigan, “5.2: Grating light valve™ technology: Update and novel applications,” *SID Symposium Digest of Technical Papers*, vol. 29, no. 1, pp. 29–32, 1998. DOI: `10.1889/1.1833752`. eprint: `https://onlinelibrary.wiley.com/doi/pdf/10.1889/1.1833752`. [Online]. Available: `https://onlinelibrary.wiley.com/doi/abs/10.1889/1.1833752`.

[28] H. J. Tiziani, T. Haist, J. Liesener, M. Reicherter, and L. Seifert, “Application of SLMs for optical metrology,” in *Spatial Light Modulators: Technology and Applications*, U. Efron, Ed., International Society for Optics and Photonics, vol. 4457, SPIE, 2001, pp. 72–81. DOI: `10.1117/12.447740`. [Online]. Available: `https://doi.org/10.1117/12.447740`.

[29] A. M. Weiner, “Femtosecond pulse shaping using spatial light modulators,” *Review of Scientific Instruments*, vol. 71, no. 5, pp. 1929–1960, 2000. DOI: `10.1063/1.1150614`. eprint: `https://doi.org/10.1063/1.1150614`. [Online]. Available: `https://doi.org/10.1063/1.1150614`.

[30] S. Zwick, T. Haist, M. Warber, and W. Osten, “Dynamic holography using pixelated light modulators,” *Appl. Opt.*, vol. 49, no. 25, F47–F58, 2010. DOI: `10.1364/AO.49.000F47`. [Online]. Available: `http://ao.osa.org/abstract.cfm?URI=ao-49-25-F47`.

[31] K. C. Neuman and S. M. Block, "Optical trapping," *Review of Scientific Instruments*, vol. 75, no. 9, pp. 2787–2809, 2004. DOI: `10.1063/1.1785844`. eprint: `https://doi.org/10.1063/1.1785844`. [Online]. Available: `https://doi.org/10.1063/1.1785844`.

[32] D. G. Grier, "A revolution in optical manipulation," *Nature*, vol. 424, no. 6950, pp. 810–816, 2003, ISSN: 1476-4687. DOI: `10.1038/nature01935`. [Online]. Available: `https://doi.org/10.1038/nature01935`.

[33] Z. Chen, T. Zeng, B. Qian, and J. Ding, "Complete shaping of optical vector beams," *Opt. Express*, vol. 23, no. 14, pp. 17 701–17 710, 2015. DOI: `10.1364/OE.23.017701`. [Online]. Available: `http://www.opticsexpress.org/abstract.cfm?URI=oe-23-14-17701`.

[34] J. Wang, J.-Y. Yang, I. M. Fazal, N. Ahmed, Y. Yan, H. Huang, Y. Ren, Y. Yue, S. Dolinar, M. Tur, and A. E. Willner, "Terabit free-space data transmission employing orbital angular momentum multiplexing," *Nature Photonics*, vol. 6, no. 7, pp. 488–496, 2012. DOI: `10.1038/nphoton.2012.138`. [Online]. Available: `https://doi.org/10.1038/nphoton.2012.138`.

[35] F. Aieta, P. Genevet, N. Yu, M. A. Kats, Z. Gaburro, and F. Capasso, "Out-of-plane reflection and refraction of light by anisotropic optical antenna metasurfaces with phase discontinuities," *Nano Letters*, vol. 12, no. 3, pp. 1702–1706, 2012, PMID: 22335616. DOI: `10.1021/nl300204s`. eprint: `https://doi.org/10.1021/nl300204s`. [Online]. Available: `https://doi.org/10.1021/nl300204s`.

[36] A. V. Kildishev, A. Boltasseva, and V. M. Shalaev, "Planar photonics with metasurfaces," *Science*, vol. 339, no. 6125, 2013, ISSN: 0036-8075. DOI: `10.1126/science.1232009`. eprint: `https://science.sciencemag.org/content/339/6125/1232009.full.pdf`. [Online]. Available: `https://science.sciencemag.org/content/339/6125/1232009`.

[37] M. Khorasaninejad, W. T. Chen, R. C. Devlin, J. Oh, A. Y. Zhu, and F. Capasso, "Metalenses at visible wavelengths: Diffraction-limited focusing and subwavelength resolution imaging," *Science*, vol. 352, no. 6290, pp. 1190–1194, 2016, ISSN: 0036-8075. DOI: `10.1126/science.aaf6644`. eprint: `https://science.sciencemag.org/content/352/6290/1190.full.pdf`. [Online]. Available: `https://science.sciencemag.org/content/352/6290/1190`.

[38] M. C. Y. Huang, Y. Zhou, and C. J. Chang-Hasnain, "A surface-emitting laser incorporating a high-index-contrast subwavelength grating," *Nature Photonics*, vol. 1, no. 2, pp. 119–122, 2007, ISSN: 1749-4893. DOI: `10.1038/nphoton.2006.80`. [Online]. Available: `https://doi.org/10.1038/nphoton.2006.80`.

[39] G. Kelp, N. Arju, A. Lee, E. Esquivel, R. Delgado, Y. Yu, S. Dutta-Gupta, K. Sokolov, and G. Shvets, “Application of metasurface-enhanced infrared spectroscopy to distinguish between normal and cancerous cell types,” *Analyst*, vol. 144, pp. 1115–1127, 4 2019. DOI: `10.1039/C8AN01433G`. [Online]. Available: `http://dx.doi.org/10.1039/C8AN01433G`.

[40] G. Lozano, S. R. Rodriguez, M. A. Verschuuren, and J. Gómez Rivas, “Metallic nanostructures for efficient led lighting,” *Light: Science & Applications*, vol. 5, no. 6, e16080–e16080, 2016, ISSN: 2047-7538. DOI: `10.1038/lsa.2016.80`. [Online]. Available: `https://doi.org/10.1038/lsa.2016.80`.

[41] B. Wang, F. Dong, D. Yang, Z. Song, L. Xu, W. Chu, Q. Gong, and Y. Li, “Polarization-controlled color-tunable holograms with dielectric metasurfaces,” *Optica*, vol. 4, no. 11, pp. 1368–1371, 2017. DOI: `10.1364/OPTICA.4.001368`. [Online]. Available: `http://www.osapublishing.org/optica/abstract.cfm?URI=optica-4-11-1368`.

[42] G. Kafaie Shirmanesh, R. Sokhoyan, R. A. Pala, and H. A. Atwater, “Dual-gated active metasurface at 1550 nm with wide (>300°) phase tunability,” *Nano Letters*, vol. 18, no. 5, pp. 2957–2963, 2018, PMID: 29570306. DOI: `10.1021/acs.nanolett.8b00351`. eprint: `https://doi.org/10.1021/acs.nanolett.8b00351`. [Online]. Available: `https://doi.org/10.1021/acs.nanolett.8b00351`.

[43] J. K. Doylend, M. J. R. Heck, J. T. Bovington, J. D. Peters, L. A. Coldren, and J. E. Bowers, “Two-dimensional free-space beam steering with an optical phased array on silicon-on-insulator,” *Opt. Express*, vol. 19, no. 22, pp. 21 595–21 604, 2011. DOI: `10.1364/OE.19.021595`. [Online]. Available: `http://www.opticsexpress.org/abstract.cfm?URI=oe-19-22-21595`.

[44] K. V. Acoleyen, W. Bogaerts, J. Jágerská, N. L. Thomas, R. Houdré, and R. Baets, “Off-chip beam steering with a one-dimensional optical phased array on silicon-on-insulator,” *Opt. Lett.*, vol. 34, no. 9, pp. 1477–1479, 2009. DOI: `10.1364/OL.34.001477`. [Online]. Available: `http://ol.osa.org/abstract.cfm?URI=ol-34-9-1477`.

[45] F. Aflatouni, B. Abiri, A. Rekhi, and A. Hajimiri, “Nanophotonic coherent imager,” *Opt. Express*, vol. 23, no. 4, pp. 5117–5125, 2015. DOI: `10.1364/OE.23.005117`. [Online]. Available: `http://www.opticsexpress.org/abstract.cfm?URI=oe-23-4-5117`.

[46] ——, “Nanophotonic projection system,” *Opt. Express*, vol. 23, no. 16, pp. 21 012–21 022, 2015. DOI: `10.1364/OE.23.021012`. [Online]. Available: `http://www.opticsexpress.org/abstract.cfm?URI=oe-23-16-21012`.

[47] D. A. B. Miller, "Self-configuring universal linear optical component

invited

," *Photon. Res.*, vol. 1, no. 1, pp. 1–15, 2013. DOI: `10.1364/PRJ.1.000001`. [Online]. Available: `http://www.osapublishing.org/prj/abstract.cfm?URI=prj-1-1-1`.

[48] B. Schwarz, "Mapping the world in 3D," *Nature Photonics*, vol. 4, pp. 429–430, 2010. [Online]. Available: `http://dx.doi.org/10.1038/nphoton.2010.148`.

[49] C. W. Oh, E. Tangdiongga, and A. M. J. Koonen, "Steerable pencil beams for multi-gbps indoor optical wireless communication," *Opt. Lett.*, vol. 39, no. 18, pp. 5427–5430, 2014. DOI: `10.1364/OL.39.005427`. [Online]. Available: `http://ol.osa.org/abstract.cfm?URI=ol-39-18-5427`.

[50] T. Koonen, J. Oh, K. Mekonnen, Z. Cao, and E. Tangdiongga, "Ultra-high capacity indoor optical wireless communication using 2D-steered pencil beams," *Journal of Lightwave Technology*, vol. 34, no. 20, pp. 4802–4809, 2016, ISSN: 0733-8724. DOI: `10.1109/JLT.2016.2574855`.

[51] D. Kwong, A. Hosseini, J. Covey, Y. Zhang, X. Xu, H. Subbaraman, and R. T. Chen, "On-chip silicon optical phased array for two-dimensional beam steering," *Opt. Lett.*, vol. 39, no. 4, pp. 941–944, 2014. DOI: `10.1364/OL.39.000941`. [Online]. Available: `http://ol.osa.org/abstract.cfm?URI=ol-39-4-941`.

[52] J. C. Hulme, J. K. Doylend, M. J. R. Heck, J. D. Peters, M. L. Davenport, J. T. Bovington, L. A. Coldren, and J. E. Bowers, "Fully integrated hybrid silicon two dimensional beam scanner," *Opt. Express*, vol. 23, no. 5, pp. 5861–5874, 2015. DOI: `10.1364/OE.23.005861`. [Online]. Available: `http://www.opticsexpress.org/abstract.cfm?URI=oe-23-5-5861`.

[53] J. E. Bowers, T. Komljenovic, M. Davenport, J. Hulme, A. Y. Liu, C. T. Santis, A. Spott, S. Srinivasan, E. J. Stanton, and C. Zhang, "Recent advances in silicon photonic integrated circuits," in *Next-Generation Optical Communication: Components, Sub-Systems, and Systems V*, G. Li and X. Zhou, Eds., International Society for Optics and Photonics, vol. 9774, SPIE, 2016, pp. 1–18. DOI: `10.1117/12.2221943`. [Online]. Available: `https://doi.org/10.1117/12.2221943`.

[54] A. E. Lim, J. Song, Q. Fang, C. Li, X. Tu, N. Duan, K. K. Chen, R. P. Tern, and T. Liow, "Review of silicon photonics foundry efforts," *IEEE Journal of Selected Topics in Quantum Electronics*, vol. 20, no. 4, pp. 405–416, 2014, ISSN: 1077-260X. DOI: `10.1109/JSTQE.2013.2293274`.

[55] W. D. Sacher, J. C. Mikkelsen, Y. Huang, J. C. C. Mak, Z. Yong, X. Luo, Y. Li, P. Dumais, J. Jiang, D. Goodwill, E. Bernier, P. G. Lo, and J. K. S. Poon, "Monolithically integrated multilayer silicon nitride-on-silicon waveguide platforms for 3-d photonic circuits and devices," *Proceedings of the IEEE*, vol. 106, no. 12, pp. 2232–2245, 2018, ISSN: 1558-2256. DOI: `10.1109/JPROC.2018.2860994`.

[56] C. V. Poulton, M. J. Byrd, M. Raval, Z. Su, N. Li, E. Timurdogan, D. Coolbaugh, D. Vermeulen, and M. R. Watts, "Large-scale silicon nitride nanophotonic phased arrays at infrared and visible wavelengths," *Opt. Lett.*, vol. 42, no. 1, pp. 21–24, 2017. DOI: `10.1364/OL.42.000021`. [Online]. Available: `http://ol.osa.org/abstract.cfm?URI=ol-42-1-21`.

[57] D. Pozar, *Microwave Engineering*. Wiley, 2004, ISBN: 9780471448785. [Online]. Available: `https://books.google.com/books?id=4wzpQwAACAAJ`.

[58] B. J. Frey, D. B. Leviton, and T. J. Madison, "Temperature-dependent refractive index of silicon and germanium," in *Optomechanical Technologies for Astronomy*, E. Atad-Ettedgui, J. Antebi, and D. Lemke, Eds., International Society for Optics and Photonics, vol. 6273, SPIE, 2006, pp. 790–799. DOI: `10.1117/12.672850`. [Online]. Available: `https://doi.org/10.1117/12.672850`.

[59] E. Timurdogan, C. V. Poulton, M. J. Byrd, and M. R. Watts, "Electric field-induced second-order nonlinear optical effects in silicon waveguides," *Nature Photonics*, vol. 11, no. 3, pp. 200–206, 2017, ISSN: 1749-4893. DOI: `10.1038/nphoton.2017.14`. [Online]. Available: `https://doi.org/10.1038/nphoton.2017.14`.

[60] J. Sun, E. Timurdogan, A. Yaacobi, E. S. Hosseini, and M. R. Watts, "Large-scale nanophotonic phased array," *Nature*, vol. 493, pp. 195–199, 2013. [Online]. Available: `http://dx.doi.org/10.1038/nature11727`.

[61] C. V. Poulton, M. J. Byrd, M. Raval, Z. Su, N. Li, E. Timurdogan, D. Coolbaugh, D. Vermeulen, and M. R. Watts, "Large-scale silicon nitride nanophotonic phased arrays at infrared and visible wavelengths," *Opt. Lett.*, vol. 42, no. 1, pp. 21–24, 2017. DOI: `10.1364/OL.42.000021`. [Online]. Available: `http://ol.osa.org/abstract.cfm?URI=ol-42-1-21`.

[62] S. Chung, H. Abediasl, and H. Hashemi, "A monolithically integrated large-scale optical phased array in silicon-on-insulator CMOS," *IEEE Journal of Solid-State Circuits*, vol. 53, no. 1, pp. 275–296, 2018, ISSN: 0018-9200. DOI: `10.1109/JSSC.2017.2757009`.

[63] S. A. Miller, C. T. Phare, Y.-C. Chang, X. Ji, O. A. J. Gordillo, A. Mohanty, S. P. Roberts, M. C. Shin, B. Stern, M. Zadka, and M. Lipson, "512-element actively steered silicon phased array for low-power LIDAR," in *Conference on Lasers and Electro-Optics*, Optical Society of America, 2018, JTh5C.2.

[Online]. Available: `http://www.osapublishing.org/abstract.cfm?URI=CLEO_SI-2018-JTh5C.2`.

[64] C. V. Poulton, A. Yaacobi, D. B. Cole, M. J. Byrd, M. Raval, D. Vermeulen, and M. R. Watts, "Coherent solid-state lidar with silicon photonic optical phased arrays," *Opt. Lett.*, vol. 42, no. 20, pp. 4091–4094, 2017. DOI: `10.1364/OL.42.004091`. [Online]. Available: `http://ol.osa.org/abstract.cfm?URI=ol-42-20-4091`.

[65] C. V. Poulton, P. Russo, E. Timurdogan, M. Whitson, M. J. Byrd, E. Hosseini, B. Moss, Z. Su, D. Vermeulen, and M. R. Watts, "High-performance integrated optical phased arrays for chip-scale beam steering and lidar," in *Conference on Lasers and Electro-Optics*, Optical Society of America, 2018, ATu3R.2. DOI: `10.1364/CLEO_AT.2018.ATu3R.2`. [Online]. Available: `http://www.osapublishing.org/abstract.cfm?URI=CLEO_AT-2018-ATu3R.2`.

[66] J. J. López, S. A. Skirlo, D. Kharas, J. Sloan, J. Herd, P. Juodawlkis, M. Soljačić, and C. Sorace-Agaskar, "Planar-lens enabled beam steering for chip-scale lidar," in *Conference on Lasers and Electro-Optics*, Optical Society of America, 2018, SM3I.1. DOI: `10.1364/CLEO_SI.2018.SM3I.1`. [Online]. Available: `http://www.osapublishing.org/abstract.cfm?URI=CLEO_SI-2018-SM3I.1`.

[67] W. Zhang, "Lidar-based road and road-edge detection," in *2010 IEEE Intelligent Vehicles Symposium*, 2010, pp. 845–848. DOI: `10.1109/IVS.2010.5548134`.

[68] M. A. Khalighi and M. Uysal, "Survey on free space optical communication: A communication theory perspective," *IEEE Communications Surveys Tutorials*, vol. 16, no. 4, pp. 2231–2258, 2014, ISSN: 1553-877X. DOI: `10.1109/COMST.2014.2329501`.

[69] C. V. Poulton, D. Vermeulen, E. Hosseini, E. Timurdogan, Z. Su, B. Moss, and M. R. Watts, "Lens-free chip-to-chip free-space laser communication link with a silicon photonics optical phased array," in *Frontiers in Optics 2017*, Optical Society of America, 2017, FW5A.3. DOI: `10.1364/FIO.2017.FW5A.3`. [Online]. Available: `http://www.osapublishing.org/abstract.cfm?URI=FiO-2017-FW5A.3`.

[70] S. J. Spector, B. F. Lane, M. R. Watts, L. D. Benney, J. G. Delva, A. E. Hare, A. F. Kelsey, J. M. Mlynarczyk, E. S. Hosseini, C. V. Poulton, and J. P. Laine, "Broadband imaging and wireless communication with an optical phased array," in *Conference on Lasers and Electro-Optics*, Optical Society of America, 2018, SM3I.7. DOI: `10.1364/CLEO_SI.2018.SM3I.7`. [Online]. Available: `http://www.osapublishing.org/abstract.cfm?URI=CLEO_SI-2018-SM3I.7`.

[71] J. Zhou, J. Sun, A. Yaacobi, C. V. Poulton, and M. R. Watts, "Design of 3d hologram emitting optical phased arrays," in *Advanced Photonics 2015*, Optical Society of America, 2015, IT4A.7. doi: `10.1364/IPRSN.2015.IT4A.7`. [Online]. Available: `http://www.osapublishing.org/abstract.cfm?URI=IPRSN-2015-IT4A.7`.

[72] R. Hansen, *Phased Array Antennas*, ser. Wiley Series in Microwave and Optical Engineering. Wiley, 2009, isbn: 9780470529171. [Online]. Available: `https://books.google.com/books?id=vVtnDPhi43YC`.

[73] R. A. Meyer, "Optical beam steering using a multichannel lithium tantalate crystal," *Appl. Opt.*, vol. 11, no. 3, pp. 613–616, 1972. doi: `10.1364/AO.11.000613`. [Online]. Available: `http://ao.osa.org/abstract.cfm?URI=ao-11-3-613`.

[74] H. Sasaki and R. M. De La Rue, "Electro-optic multichannel waveguide deflector," *Electronics Letters*, vol. 13, no. 10, pp. 295–296, 1977.

[75] F. Vasey, F. K. Reinhart, R. Houdré, and J. M. Stauffer, "Spatial optical beam steering with an algaas integrated phased array," *Appl. Opt.*, vol. 32, no. 18, pp. 3220–3232, 1993. doi: `10.1364/AO.32.003220`. [Online]. Available: `http://ao.osa.org/abstract.cfm?URI=ao-32-18-3220`.

[76] K. V. Acoleyen, W. Bogaerts, J. Jágerská, N. L. Thomas, R. Houdré, and R. Baets, "Off-chip beam steering with a one-dimensional optical phased array on silicon-on-insulator," *Opt. Lett.*, vol. 34, no. 9, pp. 1477–1479, 2009. doi: `10.1364/OL.34.001477`. [Online]. Available: `http://ol.osa.org/abstract.cfm?URI=ol-34-9-1477`.

[77] J. K. Doylend, M. J. R. Heck, J. T. Bovington, J. D. Peters, L. A. Coldren, and J. E. Bowers, "Two-dimensional free-space beam steering with an optical phased array on silicon-on-insulator," *Opt. Express*, vol. 19, no. 22, pp. 21 595–21 604, 2011. doi: `10.1364/OE.19.021595`. [Online]. Available: `http://www.opticsexpress.org/abstract.cfm?URI=oe-19-22-21595`.

[78] K. Van Acoleyen, K. Komorowska, W. Bogaerts, and R. Baets, "One-dimensional off-chip beam steering and shaping using optical phased arrays on silicon-on-insulator," *Journal of Lightwave Technology*, vol. 29, no. 23, pp. 3500–3505, 2011.

[79] F. Xiao, W. Hu, and A. Xu, "Optical phased-array beam steering controlled by wavelength," *Appl. Opt.*, vol. 44, no. 26, pp. 5429–5433, 2005.

[80] K. Van Acoleyen, W. Bogaerts, and R. Baets, "Two-dimensional dispersive off-chip beam scanner fabricated on silicon-on-insulator," *IEEE Photonics Technology Letters*, vol. 23, no. 17, pp. 1270–1272, 2011.

[81] K. V. Acoleyen, H. Rogier, and R. Baets, "Two-dimensional optical phased array antenna on silicon-on-insulator," *Opt. Express*, vol. 18, no. 13, pp. 13 655–13 660, 2010. doi: `10.1364/OE.18.013655`. [Online]. Available: `http://www.opticsexpress.org/abstract.cfm?URI=oe-18-13-13655`.

[82] J. C. Hulme, J. K. Doylend, M. J. R. Heck, J. D. Peters, M. L. Davenport, J. T. Bovington, L. A. Coldren, and J. E. Bowers, "Fully integrated hybrid silicon two dimensional beam scanner," *Opt. Express*, vol. 23, no. 5, pp. 5861–5874, 2015. doi: `10.1364/OE.23.005861`. [Online]. Available: `http://www.opticsexpress.org/abstract.cfm?URI=oe-23-5-5861`.

[83] H. Abediasl and H. Hashemi, "Monolithic optical phased-array transceiver in a standard SOI CMOS process," *Opt. Express*, vol. 23, no. 5, pp. 6509–6519, 2015. doi: `10.1364/OE.23.006509`. [Online]. Available: `http://www.opticsexpress.org/abstract.cfm?URI=oe-23-5-6509`.

[84] M. R. Kossey, C. Rizk, and A. C. Foster, "End-fire silicon optical phased array with half-wavelength spacing," *APL Photonics*, vol. 3, no. 1, p. 011 301, 2018. doi: `10.1063/1.5000741`. eprint: `https://doi.org/10.1063/1.5000741`. [Online]. Available: `https://doi.org/10.1063/1.5000741`.

[85] D. N. Hutchison, J. Sun, J. K. Doylend, R. Kumar, J. Heck, W. Kim, C. T. Phare, A. Feshali, and H. Rong, "High-resolution aliasing-free optical beam steering," *Optica*, vol. 3, no. 8, pp. 887–890, 2016. doi: `10.1364/OPTICA.3.000887`. [Online]. Available: `http://www.osapublishing.org/optica/abstract.cfm?URI=optica-3-8-887`.

[86] C. V. Poulton, A. Yaacobi, Z. Su, M. J. Byrd, and M. R. Watts, "Optical phased array with small spot size, high steering range and grouped cascaded phase shifters," in *Advanced Photonics 2016 (IPR, NOMA, Sensors, Networks, SPPCom, SOF)*, Optical Society of America, 2016, IW1B.2. doi: `10.1364/IPRSN.2016.IW1B.2`. [Online]. Available: `http://www.osapublishing.org/abstract.cfm?URI=IPRSN-2016-IW1B.2`.

[87] J. Notaros, M. Raval, M. Notaros, and M. R. Watts, "Integrated-phased-array-based visible-light near-eye holographic projector," in *Conference on Lasers and Electro-Optics*, Optical Society of America, 2019, STu3O.4. doi: `10.1364/CLEO_SI.2019.STu3O.4`. [Online]. Available: `http://www.osapublishing.org/abstract.cfm?URI=CLEO_SI-2019-STu3O.4`.

[88] M. Prost, Y. Ling, S. Cakmakyapan, Y. Zhang, K. Zhang, J. Hu, Y. Zhang, and S. J. B. Yoo, "Solid-state mwir beam steering using optical phased array on germanium-silicon photonic platform," *IEEE Photonics Journal*, vol. 11, no. 6, pp. 1–9, 2019.

[89] J. M. Zara, S. Yazdanfar, K. D. Rao, J. A. Izatt, and S. W. Smith, "Electrostatic micromachine scanning mirror for optical coherence tomography," *Opt. Lett.*, vol. 28, no. 8, pp. 628–630, 2003. doi: `10.1364/OL.28.000628`.

[Online]. Available: `http://ol.osa.org/abstract.cfm?URI=ol-28-8-628`.

[90] A. Tuantranont, V. Bright, J. Zhang, W. Zhang, J. Neff, and Y. Lee, "Optical beam steering using mems-controllable microlens array," *Sensors and Actuators A: Physical*, vol. 91, no. 3, pp. 363–372, 2001, Proceedings of the Technical Digest of the 2000 Solid-State Sensors and Actuators Workshop, ISSN: 0924-4247. DOI: `https://doi.org/10.1016/S0924-4247(01)00609-4`. [Online]. Available: `http://www.sciencedirect.com/science/article/pii/S0924424701006094`.

[91] T. K. Chan, M. Megens, B.-W. Yoo, J. Wyras, C. J. Chang-Hasnain, M. C. Wu, and D. A. Horsley, "Optical beamsteering using an 8 × 8 mems phased array with closed-loop interferometric phase control," *Opt. Express*, vol. 21, no. 3, pp. 2807–2815, 2013. DOI: `10.1364/OE.21.002807`. [Online]. Available: `http://www.opticsexpress.org/abstract.cfm?URI=oe-21-3-2807`.

[92] X. Shang, A. M. Trinidad, P. Joshi, J. D. Smet, D. Cuypers, and H. D. Smet, "Tunable optical beam deflection via liquid crystal gradient refractive index generated by highly resistive polymer film," *IEEE Photonics Journal*, vol. 8, no. 3, pp. 1–11, 2016, ISSN: 1943-0655. DOI: `10.1109/JPHOT.2016.2555585`.

[93] J. Stockley and S. Serati, "Advances in liquid crystal beam steering," in *Free-Space Laser Communications IV*, J. C. Ricklin and D. G. Voelz, Eds., International Society for Optics and Photonics, vol. 5550, SPIE, 2004, pp. 32–39. DOI: `10.1117/12.562595`. [Online]. Available: `https://doi.org/10.1117/12.562595`.

[94] R. Mailloux, *Phased Array Antenna Handbook*, ser. Antennas and Propagation Library. Artech House, 2005, ISBN: 9781580536899. [Online]. Available: `https://books.google.com/books?id=v-htQgAACAAJ`.

[95] F. Bratkovic, "Computer determination of spaces of a broad-band nonuniform antenna array," *IEEE Transactions on Antennas and Propagation*, vol. 21, no. 3, pp. 407–408, 1973, ISSN: 0018-926X. DOI: `10.1109/TAP.1973.1140511`.

[96] A. Trucco, "Thinning and weighting of large planar arrays by simulated annealing," *IEEE Transactions on Ultrasonics, Ferroelectrics, and Frequency Control*, vol. 46, no. 2, pp. 347–355, 1999, ISSN: 0885-3010. DOI: `10.1109/58.753023`.

[97] B. Fuchs, "Synthesis of sparse arrays with focused or shaped beampattern via sequential convex optimizations," *IEEE Transactions on Antennas and Propagation*, vol. 60, no. 7, pp. 3499–3503, 2012, ISSN: 0018-926X. DOI: `10.1109/TAP.2012.2196951`.

[98] R. L. Haupt, “Thinned arrays using genetic algorithms,” *IEEE Transactions on Antennas and Propagation*, vol. 42, no. 7, pp. 993–999, 1994, ISSN: 0018-926X. DOI: `10.1109/8.299602`.

[99] A. Trucco and V. Murino, “Stochastic optimization of linear sparse arrays,” *IEEE Journal of Oceanic Engineering*, vol. 24, no. 3, pp. 291–299, 1999, ISSN: 0364-9059. DOI: `10.1109/48.775291`.

[100] R. J. Mailloux and E. Cohen, “Statistically thinned arrays with quantized element weights,” *IEEE Transactions on Antennas and Propagation*, vol. 39, no. 4, pp. 436–447, 1991, ISSN: 0018-926X. DOI: `10.1109/8.81455`.

[101] J. O. Erstad and S. Holm, “An approach to the design of sparse array systems,” in *1994 Proceedings of IEEE Ultrasonics Symposium*, vol. 3, 1994, 1507–1510 vol.3. DOI: `10.1109/ULTSYM.1994.401876`.

[102] A. Trucco, “Thinning and weighting of large planar arrays by simulated annealing,” *IEEE Transactions on Ultrasonics, Ferroelectrics, and Frequency Control*, vol. 46, no. 2, pp. 347–355, 1999, ISSN: 0885-3010. DOI: `10.1109/58.753023`.

[103] F. J. Ares-Pena, J. A. Rodriguez-Gonzalez, E. Villanueva-Lopez, and S. R. Rengarajan, “Genetic algorithms in the design and optimization of antenna array patterns,” *IEEE Transactions on Antennas and Propagation*, vol. 47, no. 3, pp. 506–510, 1999, ISSN: 0018-926X. DOI: `10.1109/8.768786`.

[104] Y. Yang, Y. Ma, H. Guan, Y. Liu, S. Danziger, S. Ocheltree, K. Bergman, T. Baehr-Jones, and M. Hochberg, “Phase coherence length in silicon photonic platform,” *Opt. Express*, vol. 23, no. 13, pp. 16 890–16 902, 2015. DOI: `10.1364/OE.23.016890`. [Online]. Available: `http://www.opticsexpress.org/abstract.cfm?URI=oe-23-13-16890`.

[105] M. R. Watts, J. Sun, C. DeRose, D. C. Trotter, R. W. Young, and G. N. Nielson, “Adiabatic thermo-optic Mach-Zehnder switch,” *Opt. Lett.*, vol. 38, no. 5, pp. 733–735, 2013. DOI: `10.1364/OL.38.000733`. [Online]. Available: `http://ol.osa.org/abstract.cfm?URI=ol-38-5-733`.

[106] J. Notaros, N. Li, C. V. Poulton, Z. Su, M. J. Byrd, E. S. Magden, and M. R. Watts, “CMOS-compatible optical phased arrays with monolithically-integrated erbium lasers,” in *Conference on Lasers and Electro-Optics*, Optical Society of America, 2018, STu4B.2. DOI: `10.1364/CLEO_SI.2018.STu4B.2`. [Online]. Available: `http://www.osapublishing.org/abstract.cfm?URI=CLEO_SI-2018-STu4B.2`.

[107] S. Mandegaran and A. Hajimiri, “A breakdown voltage multiplier for high voltage swing drivers,” *IEEE Journal of Solid-State Circuits*, vol. 42, no. 2, pp. 302–312, 2007, ISSN: 0018-9200. DOI: `10.1109/JSSC.2006.889390`.

[108] Y. Zhang, S. Yang, A. E.-J. Lim, G.-Q. Lo, C. Galland, T. Baehr-Jones, and M. Hochberg, "A compact and low loss Y-junction for submicron silicon waveguide," *Opt. Express*, vol. 21, no. 1, pp. 1310–1316, 2013. DOI: `10.1364/OE.21.001310`. [Online]. Available: `http://www.opticsexpress.org/abstract.cfm?URI=oe-21-1-1310`.

[109] J. Park, J.-H. Kang, S. J. Kim, X. Liu, and M. L. Brongersma, "Dynamic reflection phase and polarization control in metasurfaces," *Nano Letters*, vol. 17, no. 1, pp. 407–413, 2017, PMID: 27936784. DOI: `10.1021/acs.nanolett.6b04378`. eprint: `https://doi.org/10.1021/acs.nanolett.6b04378`. [Online]. Available: `https://doi.org/10.1021/acs.nanolett.6b04378`.

[110] A. Arbabi, Y. Horie, M. Bagheri, and A. Faraon, "Dielectric metasurfaces for complete control of phase and polarization with subwavelength spatial resolution and high transmission," *Nature Nanotechnology*, vol. 10, 2015. [Online]. Available: `http://dx.doi.org/10.1038/nnano.2015.186`.

[111] M. I. Shalaev, J. Sun, A. Tsukernik, A. Pandey, K. Nikolskiy, and N. M. Litchinitser, "High-efficiency all-dielectric metasurfaces for ultracompact beam manipulation in transmission mode," *Nano Letters*, vol. 15, no. 9, pp. 6261–6266, 2015, ISSN: 1530-6984. DOI: `10.1021/acs.nanolett.5b02926`. [Online]. Available: `https://doi.org/10.1021/acs.nanolett.5b02926`.

[112] N. Mohammadi Estakhri and A. Alù, "Wave-front transformation with gradient metasurfaces," *Phys. Rev. X*, vol. 6, p. 041 008, 4 2016. DOI: `10.1103/PhysRevX.6.041008`. [Online]. Available: `https://link.aps.org/doi/10.1103/PhysRevX.6.041008`.

[113] N. Yu and F. Capasso, "Flat optics with designer metasurfaces," *Nature Materials*, vol. 13, 2014, Review Article. [Online]. Available: `http://dx.doi.org/10.1038/nmat3839`.

[114] Z. Zhu, P. G. Evans, R. F. Haglund, and J. G. Valentine, "Dynamically reconfigurable metadevice employing nanostructured phase-change materials," *Nano Letters*, vol. 17, no. 8, pp. 4881–4885, 2017, ISSN: 1530-6984. DOI: `10.1021/acs.nanolett.7b01767`. [Online]. Available: `https://doi.org/10.1021/acs.nanolett.7b01767`.

[115] J. Sautter, I. Staude, M. Decker, E. Rusak, D. N. Neshev, I. Brener, and Y. S. Kivshar, "Active tuning of all-dielectric metasurfaces," *ACS Nano*, vol. 9, no. 4, pp. 4308–4315, 2015, ISSN: 1936-0851. DOI: `10.1021/acsnano.5b00723`. [Online]. Available: `https://doi.org/10.1021/acsnano.5b00723`.

[116] H.-S. Ee and R. Agarwal, "Tunable metasurface and flat optical zoom lens on a stretchable substrate," *Nano Letters*, vol. 16, no. 4, pp. 2818–2823,

2016, ISSN: 1530-6984. DOI: 10.1021/acs.nanolett.6b00618. [Online]. Available: https://doi.org/10.1021/acs.nanolett.6b00618.

[117] Y.-W. Huang, W. T. Chen, W.-Y. Tsai, P. C. Wu, C.-M. Wang, G. Sun, and D. P. Tsai, "Aluminum plasmonic multicolor meta-hologram," *Nano Letters*, vol. 15, no. 5, pp. 3122–3127, 2015, ISSN: 1530-6984. DOI: 10.1021/acs.nanolett.5b00184. [Online]. Available: https://doi.org/10.1021/acs.nanolett.5b00184.

[118] W. T. Chen, P. Török, M. R. Foreman, C. Y. Liao, W.-Y. Tsai, P. R. Wu, and D. P. Tsai, "Integrated plasmonic metasurfaces for spectropolarimetry," *Nanotechnology*, vol. 27, no. 22, p. 224 002, 2016. [Online]. Available: http://stacks.iop.org/0957-4484/27/i=22/a=224002.

[119] M. Khorasaninejad, W. T. Chen, A. Y. Zhu, J. Oh, R. C. Devlin, D. Rousso, and F. Capasso, "Multispectral chiral imaging with a metalens," *Nano Letters*, vol. 16, no. 7, pp. 4595–4600, 2016, ISSN: 1530-6984. DOI: 10.1021/acs.nanolett.6b01897. [Online]. Available: https://doi.org/10.1021/acs.nanolett.6b01897.

[120] W. T. Chen, K.-Y. Yang, C.-M. Wang, Y.-W. Huang, G. Sun, I.-D. Chiang, C. Y. Liao, W.-L. Hsu, H. T. Lin, S. Sun, L. Zhou, A. Q. Liu, and D. P. Tsai, "High-efficiency broadband meta-hologram with polarization-controlled dual images," *Nano Letters*, vol. 14, no. 1, pp. 225–230, 2014, ISSN: 1530-6984. DOI: 10.1021/nl403811d. [Online]. Available: https://doi.org/10.1021/nl403811d.

[121] X. Ni, Z. Jing Wong, M. Mrejen, Y. Wang, and X. Zhang, "An ultrathin invisibility skin cloak for visible light," *Science*, vol. 349, no. 6254, pp. 1310–1314, 2015. DOI: 10.1126/science.aac9411.

[122] J. Kraus and R. Marhefka, *Antennas for All Applications*, ser. McGraw-Hill series in electrical engineering. McGraw-Hill, 2002, ISBN: 9780071232012. [Online]. Available: https://books.google.com/books?id=V6pSPgAACAAJ.

[123] Y. Zhang, K. Shang, Y.-C. Ling, and S. J. B. Yoo, "3d integrated silicon photonic unit cell with vertical u-turn for scalable optical phase array," in *Conference on Lasers and Electro-Optics*, Optical Society of America, 2018, SM3I.6. DOI: 10.1364/CLEO_SI.2018.SM3I.6. [Online]. Available: http://www.osapublishing.org/abstract.cfm?URI=CLEO_SI-2018-SM3I.6.

[124] W. D. Sacher, Y. Huang, G. Lo, and J. K. S. Poon, "Multilayer silicon nitride-on-silicon integrated photonic platforms and devices," *Journal of Lightwave Technology*, vol. 33, no. 4, pp. 901–910, 2015, ISSN: 0733-8724. DOI: 10.1109/JLT.2015.2392784.

[125] X. Chen, R.-D. Wen, and S.-Y. Tseng, "Analysis of optical directional couplers using shortcuts to adiabaticity," *Opt. Express*, vol. 24, no. 16,

pp. 18 322–18 331, 2016. DOI: `10.1364/OE.24.018322`. [Online]. Available: `http://www.opticsexpress.org/abstract.cfm?URI=oe-24-16-18322`.

[126] B. L. Kasper, C. A. Burrus, J. R. Talman, and K. L. Hall, “Balanced dual-detector receiver for optical heterodyne communication at gbit/s rates,” *Electronics Letters*, vol. 22, no. 8, pp. 413–415, 1986, ISSN: 0013-5194. DOI: `10.1049/el:19860282`.

[127] D. Marris-Morini, L. Vivien, J. M. Fédéli, E. Cassan, P. Lyan, and S. Laval, “Low loss and high speed silicon optical modulator based on a lateral carrier depletion structure,” *Opt. Express*, vol. 16, no. 1, pp. 334–339, 2008. DOI: `10.1364/OE.16.000334`. [Online]. Available: `http://www.opticsexpress.org/abstract.cfm?URI=oe-16-1-334`.

[128] S. Alexander, *Optical Communication Receiver Design*. SPIE Optical Engineering Press, 1997, ISBN: 9780852969007. [Online]. Available: `https://books.google.com/books?id=1FbDg3PyCocC`.

[129] A. Vasilyev, “The optoelectronic swept-frequency laser and its applications in ranging three-dimensional imaging and coherent beam combining of chirped-seed amplifiers,” PhD thesis, California Institute of Technology, 2013.

[130] B. Behroozpour, P. A. M. Sandborn, N. Quack, T. Seok, Y. Matsui, M. C. Wu, and B. E. Boser, “Electronic-photonic integrated circuit for 3d microimaging,” *IEEE Journal of Solid-State Circuits*, vol. 52, no. 1, pp. 161–172, 2017.

[131] A. Oppenheim, A. Willsky, and S. Nawab, *Signals and Systems*, ser. Prentice-Hall signal processing series. Prentice Hall, 1997, ISBN: 9780138147570. [Online]. Available: `https://books.google.com/books?id=LwQqAQAAMAAJ`.

[132] P. P. Vaidyanathan and P. Pal, “System identification with sparse coprime sensing,” *IEEE Signal Processing Letters*, vol. 17, no. 10, pp. 823–826, 2010.

[133] ——, “Theory of sparse coprime sensing in multiple dimensions,” *IEEE Transactions on Signal Processing*, vol. 59, no. 8, pp. 3592–3608, 2011.

[134] W. Heni, Y. Kutuvantavida, C. Haffner, H. Zwickel, C. Kieninger, S. Wolf, M. Lauermann, Y. Fedoryshyn, A. F. Tillack, L. E. Johnson, D. L. Elder, B. H. Robinson, W. Freude, C. Koos, J. Leuthold, and L. R. Dalton, “Silicon–organic and plasmonic–organic hybrid photonics,” *ACS Photonics*, vol. 4, no. 7, pp. 1576–1590, 2017. DOI: `10.1021/acsphotonics.7b00224`. eprint: `https://doi.org/10.1021/acsphotonics.7b00224`. [Online]. Available: `https://doi.org/10.1021/acsphotonics.7b00224`.

[135] M. Raval, C. V. Poulton, and M. R. Watts, “Unidirectional waveguide grating antennas with uniform emission for optical phased arrays,” *Opt. Lett.*, vol. 42, no. 13, pp. 2563–2566, 2017. DOI: `10.1364/OL.42.002563`. [Online]. Available: `http://ol.osa.org/abstract.cfm?URI=ol-42-13-2563`.

[136] J. L. Pita, I. Aldaya, P. Dainese, H. E. Hernandez-Figueroa, and L. H. Gabrielli, “Design of a compact cmos-compatible photonic antenna by topological optimization,” *Opt. Express*, vol. 26, no. 3, pp. 2435–2442, 2018. DOI: `10.1364/OE.26.002435`. [Online]. Available: `http://www.opticsexpress.org/abstract.cfm?URI=oe-26-3-2435`.

[137] F. Ashtiani and F. Aflatouni, “N × n optical phased array with 2n phase shifters,” *Opt. Express*, vol. 27, no. 19, pp. 27 183–27 190, 2019. DOI: `10.1364/OE.27.027183`. [Online]. Available: `http://www.opticsexpress.org/abstract.cfm?URI=oe-27-19-27183`.

[138] C. V. Poulton, M. J. Byrd, P. Russo, E. Timurdogan, M. Khandaker, D. Vermeulen, and M. R. Watts, “Long-range lidar and free-space data communication with high-performance optical phased arrays,” *IEEE Journal of Selected Topics in Quantum Electronics*, vol. 25, no. 5, pp. 1–8, 2019, ISSN: 1558-4542. DOI: `10.1109/JSTQE.2019.2908555`.

[139] P. F. Wang, G. Z. Luo, H. Y. Yu, Y. J. Li, M. Q. Wang, X. L. Zhou, W. X. Chen, Y. J. Zhang, and J. Q. Pan, “Improving the performance of optical antenna for optical phased arrays through high-contrast grating structure on soi substrate,” *Opt. Express*, vol. 27, no. 3, pp. 2703–2712, 2019. DOI: `10.1364/OE.27.002703`. [Online]. Available: `http://www.opticsexpress.org/abstract.cfm?URI=oe-27-3-2703`.

[140] Y. Wang, J. P. van Engelen, S. F. G. Reniers, M. B. J. van Rijn, X. Zhang, Z. Cao, V. Dolores-Calzadilla, K. A. Williams, M. K. Smit, and Y. Jiao, “High resolution grating antennas for beam steering on the imos platform,” in *Asia Communications and Photonics Conference (ACPC) 2019*, Optical Society of America, 2019, M4B.5. [Online]. Available: `http://www.osapublishing.org/abstract.cfm?URI=ACPC-2019-M4B.5`.

[141] N. V. Sapra, D. Vercruysse, L. Su, K. Y. Yang, J. Skarda, A. Y. Piggott, and J. Vučković, “Inverse design and demonstration of broadband grating couplers,” *IEEE Journal of Selected Topics in Quantum Electronics*, vol. 25, no. 3, pp. 1–7, 2019.

[142] Q. Wang, S. Wang, Y. Zeng, W. Wang, Y. Cai, Z. Tu, W. Yue, X. Wang, Q. Fang, and M. Yu, “Dual-layer waveguide grating antenna with high directionality for optical phased arrays,” *Appl. Opt.*, vol. 58, no. 21, pp. 5807–5811, 2019. DOI: `10.1364/AO.58.005807`. [Online]. Available: `http://ao.osa.org/abstract.cfm?URI=ao-58-21-5807`.

[143] Y. Luo, Z. Nong, S. Gao, H. Huang, Y. Zhu, L. Liu, L. Zhou, J. Xu, L. Liu, S. Yu, and X. Cai, "Low-loss two-dimensional silicon photonic grating coupler with a backside metal mirror," *Opt. Lett.*, vol. 43, no. 3, pp. 474–477, 2018. DOI: `10.1364/OL.43.000474`. [Online]. Available: `http://ol.osa.org/abstract.cfm?URI=ol-43-3-474`.

[144] W. Bogaerts, D. Taillaert, P. Dumon, D. V. Thourhout, R. Baets, and E. Pluk, "A polarization-diversity wavelength duplexer circuit in silicon-on-insulator photonic wires," *Opt. Express*, vol. 15, no. 4, pp. 1567–1578, 2007. DOI: `10.1364/OE.15.001567`. [Online]. Available: `http://www.opticsexpress.org/abstract.cfm?URI=oe-15-4-1567`.

[145] T. Watanabe, Y. Fedoryshyn, and J. Leuthold, "2-d grating couplers for vertical fiber coupling in two polarizations," *IEEE Photonics Journal*, vol. 11, no. 4, pp. 1–9, 2019.

[146] P. Velha, V. Sorianello, M. V. Preite, G. D. Angelis, T. Cassese, A. Bianchi, F. Testa, and M. Romagnoli, "Wide-band polarization controller for si photonic integrated circuits," *Opt. Lett.*, vol. 41, no. 24, pp. 5656–5659, 2016. DOI: `10.1364/OL.41.005656`. [Online]. Available: `http://ol.osa.org/abstract.cfm?URI=ol-41-24-5656`.

[147] D. Dai and H. Wu, "Realization of a compact polarization splitter-rotator on silicon," *Opt. Lett.*, vol. 41, no. 10, pp. 2346–2349, 2016. DOI: `10.1364/OL.41.002346`. [Online]. Available: `http://ol.osa.org/abstract.cfm?URI=ol-41-10-2346`.

[148] W. D. Sacher, T. Barwicz, B. J. F. Taylor, and J. K. S. Poon, "Polarization rotator-splitters in standard active silicon photonics platforms," *Opt. Express*, vol. 22, no. 4, pp. 3777–3786, 2014. DOI: `10.1364/OE.22.003777`. [Online]. Available: `http://www.opticsexpress.org/abstract.cfm?URI=oe-22-4-3777`.

[149] Z. Lu, M. Ma, H. Yun, Y. Wang, N. A. F. Jaeger, and L. Chrostowski, "Silicon photonic polarization beamsplitter and rotator for on-chip polarization control," in *2016 IEEE 13th International Conference on Group IV Photonics (GFP)*, 2016, pp. 70–71.

[150] M. Ma, A. H. K. Park, Y. Wang, H. Shoman, F. Zhang, N. A. F. Jaeger, and L. Chrostowski, "Sub-wavelength grating-assisted polarization splitter-rotators for silicon-on-insulator platforms," *Opt. Express*, vol. 27, no. 13, pp. 17 581–17 591, 2019. DOI: `10.1364/OE.27.017581`. [Online]. Available: `http://www.opticsexpress.org/abstract.cfm?URI=oe-27-13-17581`.

[151] C. J. Chang-Hasnain and W. Yang, "High-contrast gratings for integrated optoelectronics," *Adv. Opt. Photon.*, vol. 4, no. 3, pp. 379–440, 2012. DOI: `10.1364/AOP.4.000379`. [Online]. Available: `http://aop.osa.org/abstract.cfm?URI=aop-4-3-379`.

[152] M. Ghavami, M. Ghavami, L. Michael, and R. Kohno, *Ultra Wideband Signals and Systems in Communication Engineering*. Wiley, 2007, ISBN: 9780470027639. [Online]. Available: `https://books.google.com/books?id=qYFGAAAAYAAJ`.